LIÈGE université Library

https://lib.uliege.be https://matheo.uliege.be

Travail de fin d'études et stage[BR]- Travail de fin d'études : Experimental analysis and modelling of a heat pump for a micro-CHP (Combined Heat and Power) cycle[BR]- Stage d'insertion professionnelle

Auteur : Müllender, Sophie
Promoteur(s) : Lemort, Vincent
Faculté : Faculté des Sciences appliquées
Diplôme : Master en ingénieur civil électromécanicien, à finalité spécialisée en énergétique
Année académique : 2020-2021
URI/URL : http://hdl.handle.net/2268.2/11601

Avertissement à l'attention des usagers :

Tous les documents placés en accès ouvert sur le site le site MatheO sont protégés par le droit d'auteur. Conformément aux principes énoncés par la "Budapest Open Access Initiative"(BOAI, 2002), l'utilisateur du site peut lire, télécharger, copier, transmettre, imprimer, chercher ou faire un lien vers le texte intégral de ces documents, les disséquer pour les indexer, s'en servir de données pour un logiciel, ou s'en servir à toute autre fin légale (ou prévue par la réglementation relative au droit d'auteur). Toute utilisation du document à des fins commerciales est strictement interdite.

Par ailleurs, l'utilisateur s'engage à respecter les droits moraux de l'auteur, principalement le droit à l'intégrité de l'oeuvre et le droit de paternité et ce dans toute utilisation que l'utilisateur entreprend. Ainsi, à titre d'exemple, lorsqu'il reproduira un document par extrait ou dans son intégralité, l'utilisateur citera de manière complète les sources telles que mentionnées ci-dessus. Toute utilisation non explicitement autorisée ci-avant (telle que par exemple, la modification du document ou son résumé) nécessite l'autorisation préalable et expresse des auteurs ou de leurs ayants droit.

University of Liège
Faculty of Applied Sciences
Aerospace and Mechanical Engineering Department
Academic year 2020-2021

Experimental analysis and modelling of a heat pump for a micro-CHP (combined heat and power) cycle

Mullender Sophie

Academic year: 2020-2021

Master thesis submitted in partial fulfillment of
the requirements for the degree of Master in
Electromechanical Engineering

Abstract

The European Union aims to become the first climate-neutral continent by 2050. The heating and cooling sectors constitute a significant potential to reduce the energy consumption of Europe and to achieve the greenhouse gas emission reduction goal. Improving and developing energy-efficient heating and cooling technologies is imperative. This work focuses on a micro-CHP (combined heat and power) system designed for trigeneration (i.e. electricity, heating and cooling production) and, more particularly, on the $50kW_{th}$ R1234yf heat pump of the system. The first objective of this thesis is the characterisation of the heat pump performances in heating mode. A test bench of the unit is built and an experimental campaign is conducted. The effects of the refrigerant charge, the water temperature lift, the superheat and a liquid receiver are assessed. The second objective is the prediction of the performances. For this purpose, a semi-empirical model of the heat pump is built.

Acknowledgements

I would like to express my deep gratitude to my supervisor, Professor V. Lemort, for its precious advises and guidance throughout this work.

I would also like to thank all the member from the Thermodynamics Laboratory. A particular thanks to Olivier Dumont for giving me the opportunity to work on the construction of the test bench and for sharing his great knowledge on heat pump systems; to Frederic Ransy for his time and clear explanations on modelling; and to Richard Labenda, Bernard Loly and José Concha who where always available to solve the many technical problems that occurred during the construction and testing of the unit.

I am extremely thankful to Michel Delanaye for giving me the opportunity to perform my internship at MITIS. Many thanks to the team for the integration, help and advises.

Finally, I would like to convey my sincere thanks to Danish Rehman for the countless times dedicated to my thesis, the valuable advises and careful rereadings.

Contents

List of Figures

List of Tables

Nomenclature

Acronyms

BPHE Brazed Plate Heat Exchanger

CHP Combined Heat and Power

COP Coefficient Of Performance

DAQ Data Acquisition

EEV Electronic Expansion Valve

GWP Global Warming Potential

HP Heat Pump

ODP Ozone Depletion Potential

PID Proportional Integral Derivative

Symbols

$\dot{m}$	Mass flow rate	$[kg/s]$
$\dot{Q}$	Thermal power	$[W]$
$\dot{V}$	Volumetric flow rate	$[m^3/s]$
$\dot{W}$	Power	$[W]$
ϵ	Effectiveness	[-]
η	Efficiency	[-]
ρ	Density	$[kg/m^3]$
A	Area	$[m^2]$
cp	Specific heat capacity at constant pressure	$[J/(K.kg)]$
h	Enthalpy	[J/(kg)]

N	Rotational speed	$[rpm]$
P	Pressure	[Pa]
$r_{v,in}$	Built-in volume ratio	[-]
s	Entropy	$[J/(kg.K)]$
T	Temperature	$[°C]$
U	Heat exchange coefficient	$[W/(m^2.K)]$
v	Specific volume	$[m^3/kg]$
V_s	Swept volume	$[m^3]$

Subscripts and superscripts

ad	adapted
amb	ambient
aux	auxiliaries
cd	condenser
cmp	compressor
$elec$	electrical
ev	evaporator
ex	exhaust
gw	glycol water
hp	high pressure
in	internal
is	isentropic
l	liquid
$leak$	leakage
lp	low pressure
oh	over-heating
s	swept

sat	saturation
sc	subcooling
sf	secondary fluid
su	supply
th	theoretical
tp	two-phase
v	vapour
vol	volumetric
w	water
wf	working fluid

Chapter 1

Introduction

Due to population and economic growth, there has been a dramatic rise in energy and fuel consumption over the past decades. Alongside this rise, global warming has forced the European Union to take action, like becoming climate neutral by 2050. Significant projects are being carried out on energy-savings technologies to reach that goal.

In Europe, heating and cooling are responsible for nearly fifty percents of the final energy consumption. In the residential sector, space and water heating are even responsible for almost ninety-five percent of total final energy use (share of 78% and 16% respectively) [3]. In 2016, 75% of the energy used in the heating and cooling sector came from fossil fuels [4]. In fact, natural gas, oil and coil boiler represented 61% of the total European installed thermal capacity in 2012, while biomass burning technologies and heat pump only accounted for 20% and 7% of the installed capacity, respectively [5]. Reducing the consumption of the heating sector is key to achieving the European greenhouse gas emission reduction goal. It will be achieved with energy-efficient solutions.

Among high efficient heating technologies, condensing gas boilers are replacing traditional gas boilers as they increase the efficiency from 0 to 12% [6]. The flue gas produced by the combustion is cooled down below the dew point which allows the recovery of both the sensible and latent heat. Thus, this increases the thermal efficiency of the boiler. In addition, the environmental pollution of these efficient boilers is reduced as SO_2, NO_x and particulate matter are solved in the condensed water [7]. Electric heaters are highly efficient (around 100%) as the electrical work is entirely converted into heat. Electric heat pumps offer the best-adapted energy-efficient solutions for heating purposes. They have coefficients of performance higher than one and are therefore essential elements for the achievement of the decarbonization of society. However, electricity is generated with an efficiency around 34% [8], as almost two-thirds of the primary energy is lost as waste heat, and is also subjected to

transmission losses.

Combined heat and power (CHP) systems are solutions to avoid the high losses of centralised electricity production. They produce electricity while making profit from the released thermal power, which allows reaching high efficiencies. In fact, electricity is mainly produced through heat converted into electrical power, which is an inefficient process. The wasted energy is mostly rejected as heat into rivers, seas or the atmosphere as heat energy is economically and operationally impractical to transport, in contrast with electricity that is easily and efficiently transportable. In a CHP system, heat is used close to where electricity is produced. CHP systems can be classified by their technologies: internal combustion engines, steam turbines, fuel cells and gas turbines. Nuclear power, geothermal power and thermal solar power can also be used in CHP systems but have not, so far, been significantly developed. Internal combustion engines, divided between 'Otto engines' (i.e.spark ignition engines) and 'Diesel engines' (i.e. compression ignition engines), are used for power generation and heat generation (i.e. for hot water and space heating), but they can not provide higher grade heat. They can work at part load without decreasing their efficiency (down to 50% load) [9]. Steam turbines generate electricity and heat by extracting energy from hot and pressurized steam. Steam is produced by a boiler which can be fueled by coal, gas, nuclear or biomass. The high flexibility of steam turbines makes them favourable for CHP systems. Fuel cells are electrochemical devices which can operate at high temperature and therefore can work as CHP systems. They have been widely researched [10] [11] [12] [13] and show high electrical and total efficiencies. In fact, an hydrogen fuell cell project demonstrated an electrical efficiency higher than 50% and a total efficiency around 95% [14]. Gas turbines are engines that consume fuel (usually natural gas) to generate electrical power while releasing high temperature gases. The combustion between fossil fuel and compressed air produces hot exhaust gases that flow over the blades of the turbine to produce electricity. The gases exit the turbine at high temperature and can be used to heat up water to produce thermal power. Gas turbines therefore have a good potential as CHP systems.

FLAMINCO is a machine developed by Mitis that merges three of the most promising efficient technologies: a gas turbine, a heat pump and a condensing boiler. The final product is a complete micro-CHP that allows high flexibility. FLAMINCO offers three working modes, selected according to the demand (i.e. electrical power and/or thermal power) and the price of electricity:

- 1) FLAMINCO as a 98% efficient micro-CHP, that produces $10kW_e$ of electrical power and $40kW_{th}$ of thermal heat,
- 2) FLAMINCO as an ultra-efficient gas heat pump. The electricity produced

by the gas turbine is directly fed into the heat pump to produce $50kW_{th}$ in addition to the $40kW_{th}$ generated by the exhaust gases of the turbine. During peak demand times, the condensing gas boiler can be turned on to produce an additional $45kW_{th}$. As a gas heat pump, FLAMINCO can therefore deliver up to $135kW_{th}$ at a 160% average global efficiency,

- FLAMINCO, as an efficient electric heat pump, can produce $50kW$ of thermal power directly from electricity of the grid when the price of electricity is low.

This thesis will focus on the $50kW_{th}$ R1234yf heat pump of FLAMINCO.

1.1 Background

1.1.1 Electric Heat pump

Electric heat pumps are thermodynamic machines. They extract heat from low temperature to high temperature medium through the contribution of compression work. Heat is therefore not generated but transferred between heat reservoirs. The four main components of a heat pump are a compressor, an expansion valve and two heat exchangers (i.e. one condenser and one evaporator). The heat pump cycle is shown in Figure 1.1a.

Heat transfer between heat source and heat sink is achieved through a working fluid called refrigerant. The refrigerating agent is subjected to four main stages before going back to its original state. The ideal vapour compression cycle makes use of latent heat that extracts more heat at constant mass flow compared to sensible heat. The cycle is described by:

1-2: Isentropic compression by providing electrical power to the compressor.
2-3: Isobaric condensation at constant temperature in the condenser. Heat is transferred from the refrigerant to the heat sink.
3-4: Isenthalpic expansion in the expansion valve.
4-1: Isobaric evaporation at constant temperature in the evaporator. Heat is transferred from the heat source to the refrigerant.

The real vapour compression cycle is shown in Figure 1.1b. Heat transfer does not occur integrally at constant temperature. Refrigerant is superheated in the evaporator (from 4' to 1) to ensure no liquid is entering the compressor, as it could cause damages. Subcooling, at the outlet of the condenser (from 2" to 3), maintains supersaturated liquid at the inlet of the expansion valve. If not, high pressure drop occurs in the liquid line and the valve does not work properly. Compression is not isentropic and neither is expansion isenthalpic. Pressure drops occur at the inlet

and outlet of the compressor but also through the heat exchangers and piping. Heat losses to the atmosphere occur as well.

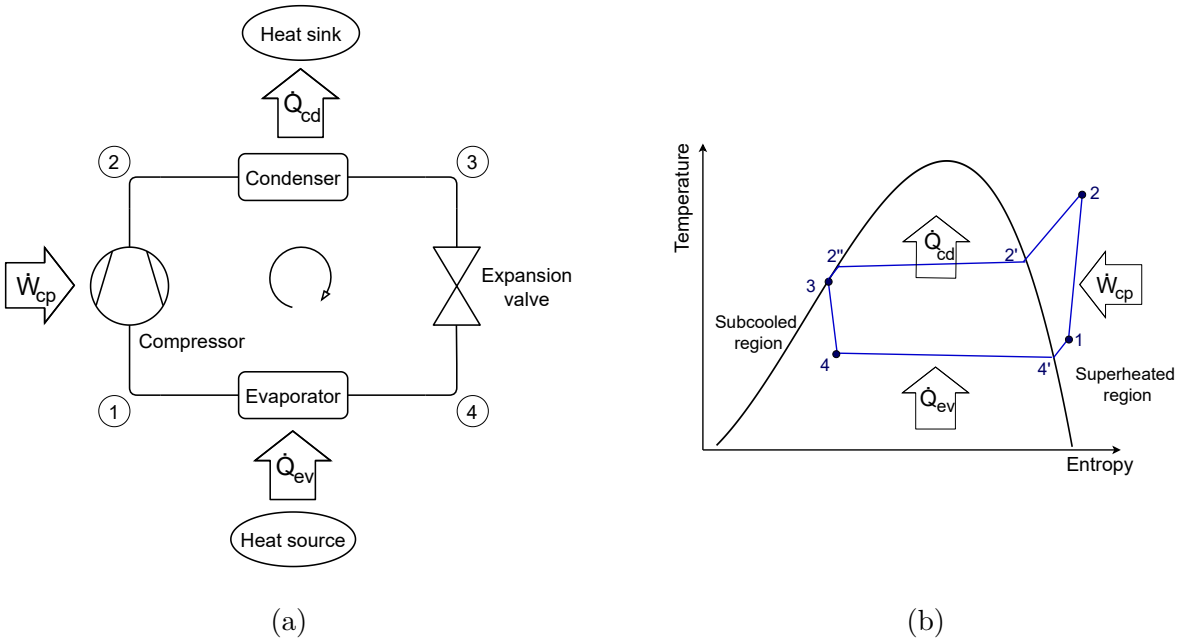

(a) (b)

Figure 1.1: Heat pump cycle (a), and T-S diagram of vapour compression cycle (b).

1.1.2 Refrigerants

As stated above, refrigerants are used to transfer heat from low-temperature medium to high-temperature medium. Their principal advantages are their low boiling point at atmospheric pressure and their high heat transfer coefficient. The low boiling point allows the refrigerant to evaporate at low temperature and therefore to take profit of low temperature heat source at high latent heat of vaporization. The high heat transfer coefficient provides a high heat transfer rate in a small heat exchange area, allowing the system to be compact. Other important properties to take into account when choosing the appropriate refrigerant could be their chemicals properties (toxicity, reactivity, oil solubility, etc), environmental effects (flammability, ozone depletion potential ODP, global warming potential GWP, etc), cost and availability.

Refrigerants are subjected to many legislations. In 1987, the Montreal Protocol on Substances that Deplete the Ozone Layer was signed to phase out the use of chlorofluorocarbons (CFCs), such as Freon-12 (ODP of 1 and GWP of 10900) [15]. R134A, which belongs to hydrofluorocarbons (HFCs), was then developed to replace CFCs and has become very common as it is safe to handle, non-toxic, non-flammable and has a zero ODP [16]. However, R134a contributes to global warming and is classified as a greenhouse gas due to its 1430 GWP. R410A and R32, despite their high

value of GWP (2088 and 675, respectively [17]) are also dominating the domestic heat pump market. The Kyoto [18] Protocol, adopted in 1997, has restricted the use of hydrofluorocarbon (HFC) because of their high global warming potential. Nowadays, studies are performed to replace refrigerants such as R134a, R410A and R32.

The new regulations are forcing the industry to develop and use refrigerants with GWP of less than 150 [19]. Alternative refrigerants have gained interest over the last years, including natural refrigerants, hydrofluoroolefins (HFOs), hydrochlorofluorolefins (HCFOs), hydrocarbons (HCs) and low-GWP hydrofluorocarbons (HFCs) [20]. They are detailed below.

Natural refrigerants, such as ammonia, carbon dioxide and water, can be used in HP systems. Their global warming and ozone depletion potential being zero, they are promising to replace the non-environmental friendly refrigerants. Ammonia (R717) has been used for more than a century and has regained great interest over the last few years, due to its low cost, high availability and extremely high latent heat [21]. However, ammonia is both flammable and toxic. R744, commonly known as CO_2, is the most promising candidate in refrigeration applications among natural refrigerants. CO_2 has many advantages as it is inert, non-toxic, non-flammable, inexpensive, available and easy to recycle. It also has high heat transfer properties, low pressure ratio and high volumetric capacity, which allows to miniaturised the system [22] [23] [24]. However, its low critical temperature imposes CO_2 to be operated in a transcritical cycle which requires a very high compression ratio and therefore strong components to avoid leakages. Water (R718) is also used as a refrigerant and subject to various researches due to its 0 ODP and GWP, non-toxicity and non-flammability. Water can be directly evaporated and condensed, as it can be used both as working and heat carrier fluid [25]. R718 has demonstrated high performances, especially in high temperature heat pumps [26]. The use of R718 is limited due to the large vapour volume flow rates, high required pressure ratio and its boiling point of $100°C$ at atmospheric pressure, which requires operating under vacuum conditions in the low pressure line when the heat source temperature is lower than $100°C$.

Hydrocarbons (HCs), such as propane (R290), propene (R1270) and isobutane (R600a), are a class of natural refrigerants. They have zero ODP, GWP lower than 10 [20] and have comparable or better performances than synthetic refrigerants [27] [28] [29]. However, HCs belong to the high flammability class of refrigerants (i.e. class 3) [30] and specials cares need to be taken. At low heat source temperature, heat pumps work under vacuum pressure and the risk of air leakage is increased, which also increases the flammability risk. Reduced charge of refrigerant, outdoor unit, forced ventilation and sensors are solutions to reduce the risk of flammability [31].

Hydrofluorocarbons (HFCs) tend to be replaced, but some low GWP HFCs are still under researches, such as R152a and R161. R152a has been known for a long time but its high level of flammability (class A2) has put restrictions on its use as a refrigerant. Due to its low GWP (138) and its similarities to R134a, R152 has regained interest [32] and has shown better performances than R134a [33] [34]. R161 has a low GWP of 12, is highly flammable [35] and has given high values of COP [36]. Its flammability issue can be addressed by mixing R161 with other refrigerants [37].

Hydrochlorofluorolefins (HCFOs) are synthetic refrigerants. The two most promising are R1233zd(E) and R1224yd(Z) because of their high critical temperature, non-flammability and non-toxicity [20]. However, their ozone depletion potentials are not equal to zero (i.e. 0.00034 and 0.00012 ODP for R1233zd(E) and R1224yd(Z), respectively) but can be considered as negligible due to their short lifetime [38]. R1233zd(E) and R1224yd(Z) show promising results in heat pump applications [38] [39].

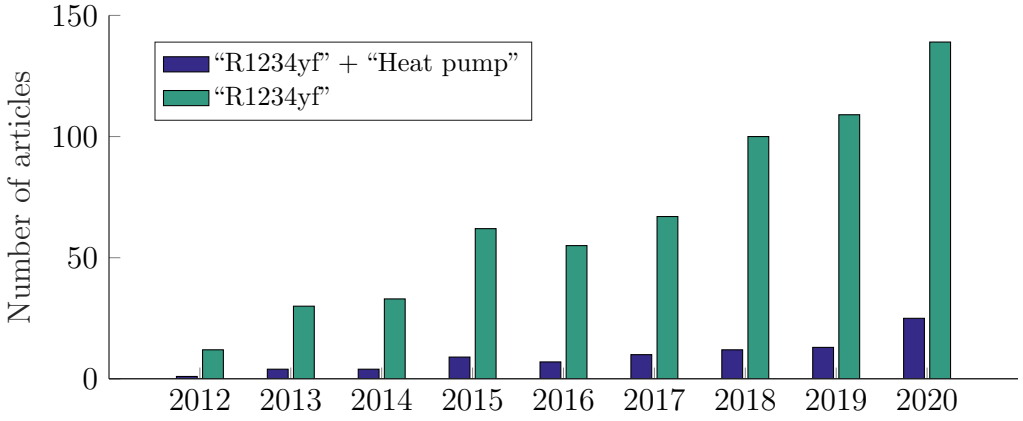

Figure 1.2: Evolution of the number of articles published on Scopus.

Hydrofluoroolefins (HFOs) are environment-friendly refrigerants, suitable to become alternatives to HFCs due to their low global warming potential [40]. R1234yf, R1234ze(E), R1234ze(Z) and R1233zd(E) are the main promising HFOs with GWP lower than 1, 0.8, 6 and 1.4, respectively [41]. R1234yf, or 2,3,3,3-tetrafluoroprop-1-ene, is the most promising HFO and has been researched in an increasing number of articles since 2012, as shown in Figure 1.2. R1234yf has been studied for mobile air conditioners (MAC), residential cooling appliances and water and air heater applications. It is important to underline that, since 2018, the research of R1234yf has mainly been carried out on HFC/HFO mixtures instead of pure R1234yf [42]. R1234yf is considered as the direct replacement of R134a [43] [44] [45] due to its comparable thermodynamics properties and oil compatibility (i.e. with POE oil). R1234yf has low toxicity, low flammability (class A2) and can be used without risk in refrigeration systems [42]. Some marginal decreases in COP have been observed

in comparison with the R134a performances, but R1234yf is still considered as a drop-in replacement of R134a, especially in the automotive sector [40]. Thanks to its numerous advantages and promising future, R1234yf has been chosen as the working fluid of the FLAMINCO heat pump.

A summary of the main refrigerants is shown in Table 1.1.

Type	ASHRAE Number	ODP	100-year GWP	Characteristics
CFC	R-12	1	10900	Not used anymore because of the high ODP
HFC	R-134a	0	1430	Getting replaced because of the high GWP
HFC	R-32	0	675	Getting replaced because of the high GWP
HFC	R-152a	0	138	Under researches to replace high GWP HFC but highly flammable (A2)
HC	R-290	0	3	Known as propane, high COP but extremely flammable (A3)
HC	R-1270	0	2	Known as propene, high COP but extremely flammable (A3)
HC	R-600a	0	3	Known as isobutane, high COP but extremely flammable (A3)
Natural refrigerant	Ammonia	0	0	Highly available, affordable but flammable and toxic
Natural refrigerant	Carbon dioxide	0	1	Inert, available but low critical temperature and thus used in transcritical system
Natural refrigerant	Water	0	0	Non-toxic, available but large vapour volume flow rates
HFCO	R1233zd(E)	0.00034	1	Non-flammable, non-toxic but non-zero ODP
HFO	R1234yf	0	1	Relatively non-toxic and non-flammable, used as drop-in replacement of R134a

Table 1.1: Summary of the existing refrigerants.

1.2 Aim of the thesis

This thesis aims to analyse the performance in heating mode of a geothermal R1234yf heat pump designed to produce $50kW$ of thermal power for floor heating (i.e. hot water at a temperature of $35°C$). The first prototype of the FLAMINCO's heat pump is fully equipped with sensors to further characterise its behaviour. The purpose of the heat pump is its commercialisation and different configurations need to be tested in order to reach the highest coefficient of performance. The effect of the compressor rotational speed, the temperature of the heat source, the temperature of the heat sink, the refrigerant charge, the subcooling, the overheating and the liquid receiver need to be studied.
The second objective of this thesis is the prediction of the performances out of the tested temperatures and rotational speed ranges. A semi-empirical model of the heat pump therefore needs to be developed.

1.3 Overview

This thesis is organised into several chapters:

- Chapter 1: The introduction provides the context and motivation for this thesis. A theoretical background of electrical heat pumps and refrigerants is performed.
- Chapter 2: A description of the experimental setup is provided. The heat pump unit, the secondary fluid loops, the sensors and the data acquisition system are described.
- Chapter 3: A complete analysis of the experimental results is conducted.
- Chapter 4: The performances of the $50kW_{th}$ heat pump are predicted through a semi-empirical model.
- Chapter 5: Some perspectives and improvements for future works are presented.
- Chapter 6: The main results of this thesis are summarised.

Chapter 2

Test-rig description

The water to water heat pump is located in the Thermodynamics Laboratory of the University of Liège. The experimental test rig is composed of a heat pump unit and two hydraulic loops. The scheme of the test rig is displayed in Figure 2.1. A complete description of the components is provided in the next section.

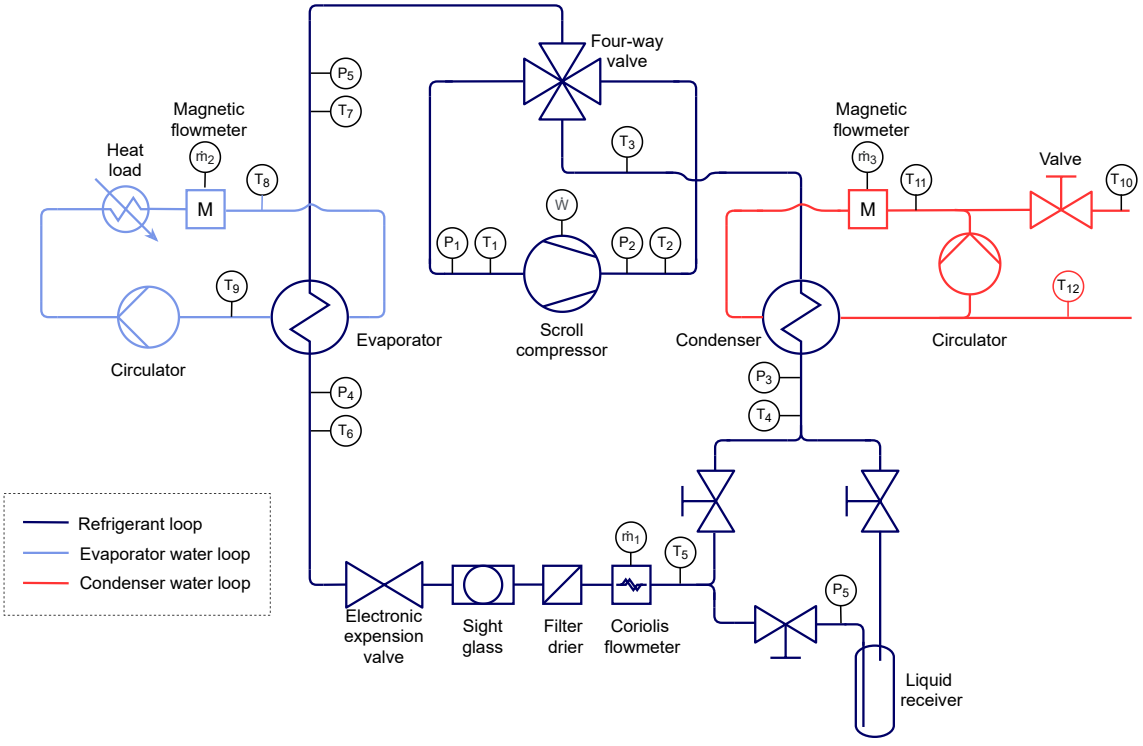

Figure 2.1: Scheme of the test rig.

2.1 Heat Pump unit

2.1.1 Compressor

The compressor selected for this application is a hermetic scroll compressor manufactured by Danfoss (model SY240). The compressor is compatible with R1234yf and

has been developed to work at 50 and 60Hz. Eventhough it is not declared as a variable speed compressor, SY240 tolerates working between 40 and 60Hz. An inverter from ABB (model ACS480) allows the speed variation of rotation and therefore controls the produced load. At high speed of rotation, mass flow of refrigerant is high and thermal power is large. A polyolester oil is used to lubricate the compressor. As no oil separator is displaced at the outlet of the scroll compressor, lubricating oil is moving with the refrigerant in the HP loop. This oil transportation is deteriorating performances by decreasing the heat transfer in the two heat exchangers. The aim of this heat pump being its commercialisation, the system is kept simple without adding an oil separator. Furthermore, compressors are nowadays designed for a good oil return inside the compressor. The main technical data of the scroll compressor are shown in Table 2.1.

Table 2.1: Technical data of Danfoss SY240 scroll compressor.

Swept volume $[cm^3]$	347.8
Lubricant	P.O.E. 320SZ

2.1.2 Heat exchangers

Two brazed plate heat exchangers (BPHE's) are used as evaporator and condenser to transfer the heat from and to the secondary loop, respectively. The secondary fluids in both the condenser and the evaporator are water and 30% Ethylene Glycol. They are counter-flow heat exchangers made of corrugated channel plates, their main advantages are their compactness and their high efficiency. The chosen ones are both manufactured by SWEP. Evaporator model is V80x84 and condenser is B80ASx66. Their main technical data are shown in Table 2.2. It is noteworthy that heat exchangers have been chosen to maximise the efficiency of the heat pump in heating mode. In cooling mode, the evaporation and condensation locations are exchanged compared to heating mode.

2.1.3 Filter dryer

A bi-directional filter dryer is added between the condenser and the electronic expansion valve. Its purpose is to remove contaminants like moisture or dirt. Moisture can freeze and restricts the flow of refrigerant, and reacts with oil to form acid. Particulates can also block the flow of refrigerant, mainly in the expansion valve.

Table 2.2: Technical data of SWEP brazed plate heat exchangers.

	Evaporator	Condenser
Model	V80x84	B80ASx66
Heat load [kW]	40	50
Total heat transfer area [m^2]	4.92	3.85
Heat flux [kW/m^2]	8.13	13
Number of plates	84	66

2.1.4 Electronic expansion valve

The expansion valve used in the heat pump is an electronic stepper motor valve from Danfoss (Colibri 12C). An electronic expansion valve (EEV) allows compactness, precise flow control and reactivity. EEV has been chosen over thermostatic expansion valve as it allows a better superheat control, and therefore a better evaporator efficiency and better COP. A positive superheat at the outlet of evaporator is mandatory to avoid liquid at the suction side of the compressor. However, a too high superheat reduces the section of the heat exchanger which is being fed with saturated refrigerant. The efficiency and capacity of the evaporator are therefore reduced as the heat exchanger is partially filled with vapour refrigerant which has a lower heat transfer coefficient than a two-phase fluid. Electronic expansion valve constantly achieves an optimally low superheat and thus a high evaporating pressure.
Colibri 12C is driven by a stepper motor and controlled by a superheat controller from Danfoss (EKE 1C). The control is set on a fixed superheat of 5 degrees Kelvin.

2.1.5 Four-way valve

A four-way valve is added to the system in order to make it reversible. It allows switching the refrigeration cycle from heating mode in winter to cooling mode in summer, by inverting the condenser and the evaporator.

2.1.6 Liquid receiver

A liquid receiver is a storage tank installed at the outlet of the condenser. It is filled with both liquid and vapour and equipped with an immersion tube that ensures liquid refrigerant at its outlet. Its purpose is twofold: to store refrigerant in case of operations on the system and to withstand refrigerant charge fluctuations.
In fact, modifying the heat pump unit requires transferring the refrigerant charge in a recovery bottle, with a dedicated pump, before doing any changes. By adding

a liquid receiver to the system, one can perform a pump down operation. This operation consists in closing the outlet of the receiver and running the compressor to pump refrigerant into the receiver. Pumping down the heat pump unit also avoids liquid migration back to the compressor during off-cycle.
Furthermore, a heat pump unit can be working under fluctuating conditions. As the total required refrigerant charge varies with the operating load, the liquid receiver acts as a buffer to balance the charge variations. The refrigerant charge must be sufficient at all time to ensure liquid refrigerant in the expansion valve but the system should not be overcharged to keep satisfying heat transfer in the heat exchangers. Excess of refrigerant mainly accumulates in the condenser causing subcooling at the outlet of the condenser to increase. Too much subcooling implies that the condenser is mostly filled up with liquid. As liquid refrigerant has lower heat transfer properties than two-phase refrigerant, heat exchangers do not operate at optimal design point.

However, liquid receivers require a minimum operating charge and therefore increase the total refrigerant mass of the heat pump unit. Adding a liquid receiver also increases the size of the heat pump. The compactness of the system being a major concern in commercial heat pump, manufacturers tend to avoid liquid receivers in their products. For this reason, the heat pump was designed and manufactured without a liquid receiver. It was decided afterwards to also test the unit with and without a receiver, one is therefore added in the liquid line between the condenser outlet and the mass flow meter. Due to the initial configuration, the heat pump can not run in cooling mode with the liquid receiver as its inlet and outlet can not be switched. Manual stop valves and a by-pass line are therefore required.

2.2 Hydraulic loops

Two hydraulic loops are needed to supply the heat pump with cold and hot fluid. The condenser is supplied with tap water through a motorized globe valve and the supply temperature is controlled by means of a recirculation pump. The evaporator is supplied with a water-glycol mixture with a thirty percents concentration of Ethylene Glycol to provide freeze protection up to -15°C. Mass flow rate and supply temperature are controlled with a pump and a 40kW resistive load, respectively.

2.2.1 Pumps

The circulators used in the two loops are both E-pumps from Grundfoss (model CME) with frequency-controlled permanent-magnet motors. They allow to precisely control the flow rate of the condenser loop and the supply temperature of the evaporator, by controlling the recirculating flow rate. The main technical data of

the pumps are shown in Table 2.3.
The pumps are controlled with a 0-10V signal which allows the variation of their rotational speed between the minimum and maximum setpoints.

Table 2.3: Technical data of Grundfoss CME pumps.

Model	CME 5-2 A-R-A-E-AQQE S-A-D-N
Nominal flow rate	5.64 m^3/h
Fluid temperatures range	-20...90°C
Rated power	1.1kW

2.2.2 Resistive load

The evaporator is supplied by a closed loop of 30% Ethylene Glycol which therefore has to be provided with heat. A resistive load of 40kW from Kamenev is used to simulate the ground source of a geothermal heat pump.
The heating load is controlled through a power regulator from Regin (model TTC80F). The regulator receives a signal between 0 and 10V and provides the resistance with an electrical power of 0 to 40kW.

2.2.3 Motorized globe valve

Through the condenser, the heat pump is generating heat which has to be rejected. The condenser loop is therefore not operated in closed loop. Tap water is entering the test bench through a valve, is being preheated to the desired supply temperature thanks to water recirculation, heated up in the condenser and then rejected to the drain. The motorized globe valve is therefore adjusting the freshwater flow rate entering the loop. The control of the valve is done through a 0 to 10V signal.

2.3 Instrumentation

In order to precisely characterise the heat pump unit, the test bench is equipped with various sensors, as shown in Figure 2.1. More details on the used sensors and data monitoring can be found as follow:

2.3.1 Measurement devices

2.3.1.1 Temperature measuring sensors

T-type thermocouples are used to measure the numerous temperatures to characterise the state of the refrigerant and of the secondary fluids. Thermocouples consist

in two wires, made of different metals, that are joined together at the end where temperature needs to be measured. An electromotive force is generated if the junction is heated up or cooled down, as explained by Seebeck effect. This electromotive force can be correlated back to the temperature using thermocouple reference tables. Conversion between voltage output and temperature reading is made with Labview software through a Data Acquisition (DAQ) system. More information about the Data Acquisition can be found in section 2.3.3. The main advantages of thermocouples are their low price and wide temperature range. Type T thermocouples are utilized with their measuring range between -200 °C and 350 °C, with a nominal accuracy of ± 0.5°C. The locations of the temperature measurements are listed in Table 2.4.

Table 2.4: List of temperature measuring sensors .

Measurement device	Temperature measuring sensors	Description
T-type thermocouples	T_1	Compressor inlet
	T_2	Compressor outlet
	T_3	Condenser inlet
	T_4	Compressor outlet
	T_5	Compressor inlet
	T_6	Corriolis flow meter inlet
	T_6	Evaporator inlet
	T_7	Evaporator outlet
	T_8	Heat source supply temperature
	T_9	Heat source exhaust temperature
	T_{10}	Tap water temperature
	T_{11}	Heat sink supply temperature
	T_{12}	Heat sink exhaust temperature

2.3.1.2 Pressure sensors

Six piezoresistive pressure transducers are installed on the heat pump unit, as shown in Table 2.5. The fifth four are made by Wika (model A-10) and have a 0-16$bar\,(g)$ range, a non-linearity of ± 0.5 % BSFL and a maximum measured error lower than ± 1% of span. The sixth pressure transducer comes from Keller (model PA-21Y), has a range of 0-6 bar(g) and a total error band of ± 1.5% Full Scale (FS). This last pressure sensor is used by the superheat controller to compute superheat at the

evaporator outlet.

Due to piezoresistive effect, a conductive material is subject to a change in its electrical resistance when it is stretched. Under pressure, the sensor element is deformed and its change in resistance can be converted to an output signal using a Wheatstone bridge. Output signal of the piezoresistive pressure transducers is between 4-20mA.

Table 2.5: List of pressure measuring sensors .

Measurement device	Pressure measuring sensors	Description
piezoresistive pressure transducer	P_1	Compressor inlet
	P_2	Compressor outlet
	P_3	Condenser outlet
	P_4	Evaporator inlet
	P_5	Receiver outlet
	P_6	Evaporator outlet

2.3.1.3 Flow meter

Three mass flow meters from Emerson are used in this test rig.
Volumetric flow rates of the two hydraulic loops are measured with magnetic flow meters (Rosemount 8705). Magnetic flow meters are made of a set of coils and of two electrodes, as depicted in Figure 2.2a. Current is supplied to the coils to form a magnetic field which causes the separation of the negative and positive charged fluid particles. Charged particles create an induced voltage at the electrodes which is measured and converted into a flow velocity thanks to Faraday's Law. Rosemount 8705 has a range of 0 to 1.2 l/s and a flow accuracy of $\pm 0.25\%$ of rate while the Rosemount transmitter has an accuracy of 0.25%.

Mass flow rate of refrigerant is measured with Coriolis flowmeter (Micro Motion ELITE CMFS050M). This flow meter is made off two parallel flow tubes which splits the flow of refrigerant as shown in Figure 2.2b. The tubes are energized by the driver unit (i.e. a coil) to oscillate and oscillations are measured with sensors at inlet and outlet of the flow meter. When there is no flow, the tubes oscillate in phase but, as long as the fluid is moving, a Coriolis force is induced which causes the tube to twist and the generated sine waves to be shifted in phase. Mass flow rate of the fluid is proportional to the time delay between the two sine waves. The density of the fluid modifies the vibrating frequency of the tube, it is therefore proportional

to the wave frequency. Micro Motion ELITE has a mass flow accuracy (Liquid) of ±0.10% of mass flow rate while the transmitter has a linearity of 0.015 % of span.

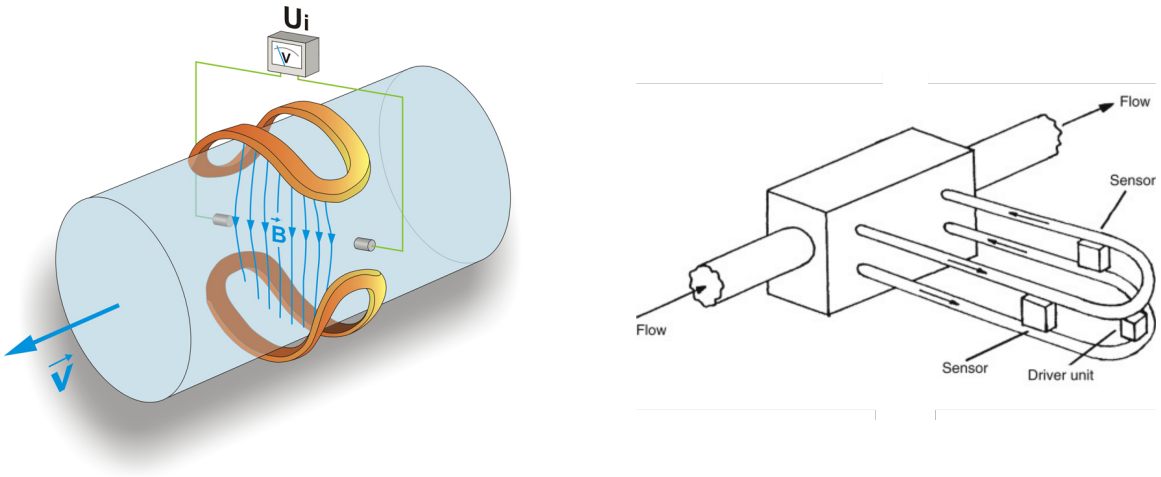

(a) (b)

Figure 2.2: Magnetic flow meter (a) and Coriolis flow meter (b).

Table 2.6: List of flow measuring sensors .

Measurement device	Flow measuring sensors	Description
Coriolis flow meter	m_1	Refrigerant [kg/s]
Magnetic flow meter	m_2	30% Ethylene Glycol [l/s]
	m_3	Water [l/s]

2.3.1.4 Power meter

A watt-meter from Camille Bauer (model SINEAX AM2000) quantifies the consumed power of the heat pump, i.e. the consumed power of the inverter. Power consumed by the compressor itself is also measured by the inverter in order to characterise the behaviour of the compressor.

2.3.1.5 Sight glass

A sight glass allows to control the state of the refrigerant (i.e. liquid or two-phase) and is installed as close as possible to the inlet of the expansion valve. In order to ensure the proper functioning of the expansion valve, the refrigerant should be supersaturated liquid at its inlet. Subcooling at the condenser outlet should ensure the supersaturated liquid state but, due to high pressure drops in the liquid line, formation of vapour bubbles can be detected in the sight glass. This sight glass is

used in order to find the proper mass of refrigerant. This will be discussed in the next chapter.

2.3.2 Safety switch

To ensure that pressure is not increasing above $16bar\,(g)$ in the heat pump, a Ranco high pressure switch is added on the high pressure side. Too high pressures can damage the pressure sensors and the compressor itself as reliable operations of the compressor are guaranteed under $20bar\,(g)$. When high pressure rises above $16bar\,(g)$, the compressor is shut down.

2.3.3 Data Monitoring

In order to fully characterise the performance of this heat pump, data coming from the test rig need to be collected and stored. This operation is done through a Data Acquisition system, Modbus communication and Labview software.

2.3.3.1 Data Acquisition System

A compactDAQ is used to receive analog signal from the measurement devices and send analog signal to some controllable components of the test bench (i.e. pumps, valve, resistance and four-way valve). The compactDAQ allows converting analog signal to digital signal and vice versa. It is worth noting that the compressor, through the inverter, and the superheat controller are controlled directly via Modbus communication. The compactDAQ is a data acquisition platform made of a CompactDAQ Chassis and four C Series Input and Output (I/O) modules: two analog output modules (current and voltage) and two analog input modules (current and thermocouple). Details on the modules can be found in Table 2.7. The chassis used in the test rig is a cDAQ 9178.

Table 2.7: C Series Input and Output modules of the test rig.

I/O Module	I/O type	range	accuracy
NI 9213	Thermocouple input	[-200;1000°C]	± 0.02°C
NI 9208	current input	[-20;20mA]	± 0.76% of reading, ± 0.04% of range
NI 9264	voltage output	[-10;10V]	± 0.2% of reading, ± 0.25% of range
NI 9265	current output	[0;4mA]	± 0.35% of reading, ± 1.4% of range

2.3.3.2 Modbus

Modbus is a communication protocol between a device requesting the information, called master, and devices providing the information, called slaves. One master can be connected with up to 247 slaves, each with a unique address. Modbus has been developed by Modicon systems in 1979. The information exchange is always initiated by the master, the slaves therefore can not send information before a request from the master.
Information is exchanged through bits of zeros and ones, sent as voltage. Zeros are positive voltage while ones are negative. Transmission is really fast: around 9600 baud (bits per second). Bits are combined in block of four to be read as hexadecimal, each block is therefore represented by characters from 0 to F. A byte is a block of 8 bits.
Inquiries from the master consist of series of bits. The first byte is used to specify the slave address as each slave as its own (from 0 to 247). The second byte states the function code with a read or write data command to the slave. If the command is to write, the next bytes specify the data to write. The Cyclic Redundancy Check (i.e. CRC), an error checking field, ends the inquiries. CRC is calculated from the previous bytes by the sending device. The receiving device also calculates the CRC to compare it with the one of the messages. If one bit has not been sent correctly, the CRC will be different and the receiving device will conclude to an error. Inquiries from the slaves are composed of the slave address, the function code, the data and a checksum.
The physical support for Modbus communication used in this set-up is RS485. RS485 is chosen for its many advantages. It can support high data rate over long distances and have many slaves on one bus. Moreover, it is immune to noise.

Modbus and RS485 are used in the test bench to control the compressor, through the inverter, by controlling its rotational speed and its ON/OFF switch. The electronic expansion valve is also controlled by Modbus through its controller. Many parameters, like the operational mode or the superheat setpoint, can be set. This communication protocol is finally used to receive data from the inverter, the EEV controller and the wattmeter.

2.3.3.3 LabView

Information from and to the components of the test bench are processed through LabView. LabView is a visual programming language developed by National Instrument to design, control and metering systems. The user interface is called Virtual Instrument (VI). LabView is particularly suitable for test bench as it is used for data acquisition and signal processing.
A main LabView VI has been created for this set-up, with additional subVI's. Its

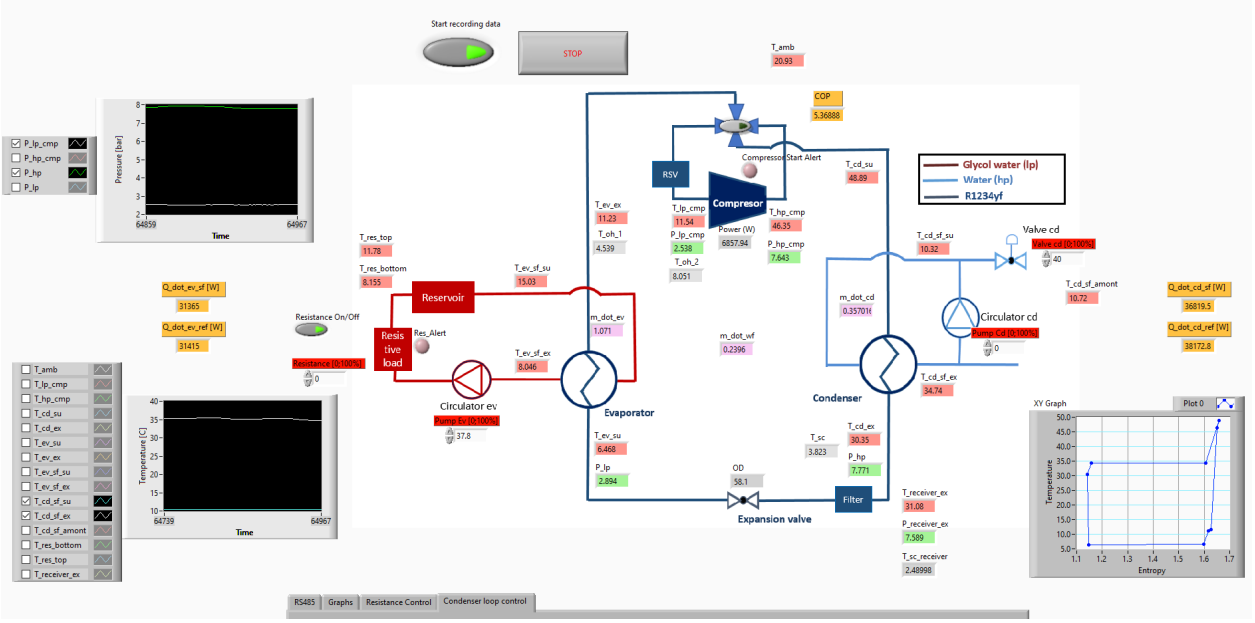

Figure 2.3: LabView VI of the test bench.

main role is to collect data from the sensors and to control the devices of the test bench. Data are then exported in a text file to be post-processed on Matlab. The VI also allows visualising, during testing, the performance of the heat pump. Temperatures, pressures and mass flow are displayed on the screen, as shown in Figure 2.3. SubVI's are created and implemented to estimate superheat, subcooling and TS diagram in order to ensure the effective operation of the test bench.

Some safety features are implemented through LabView. Indeed, many conditions need to be fulfilled to ensure the proper functioning of the test bench. Two major components need to be protected: the 40kW resistive load and the compressor. The resistance has to be given careful attention: the water-glycol mixture should always be in motion to remove the heat while the fluid temperature should never exceed 30°C. Temperature can quickly rise if those conditions are not respected and this may lead to the component degradation. Three conditions need to be satisfied in order to run the compressor. Firstly, high pressure can never exceed $16bar\,(g)$, as explained in the previous section. Secondly, deep vacuum operations are forbidden as it can cause internal electrical arcing and scroll instability. A low pressure switch is set at $0.6bar\,(g)$ as the minimum low pressure setting is $0.5bar\,(g)$ according to Danfoss. Third, exit temperature of glycol water solution from evaporator can not drop below -10° C as 30% Ethylene Glycol freezes at
-15° C. Furthermore, the resistive load is shut down if the compressor has to be turned off, and vice versa.

2.4 Experimental test set-up

Pictures of the experimental test set-up can be found in Figures 2.4a and 2.4b. The main system components are listed in Table 2.8.

Table 2.8: Main components of the test rig.

(A)	Compressor
(B)	Condenser
(C)	Evaporator
(D)	Electronic expansion valve
(E)	Sight glass
(F)	Filter dryer
(G)	Mass flow meter
(H)	Liquid receiver
(I)	Four way valve
(J)	Circulators
(K)	Mass flow meters
(L)	Heat load of the evaporator loop
(M)	Valve of the condenser loop

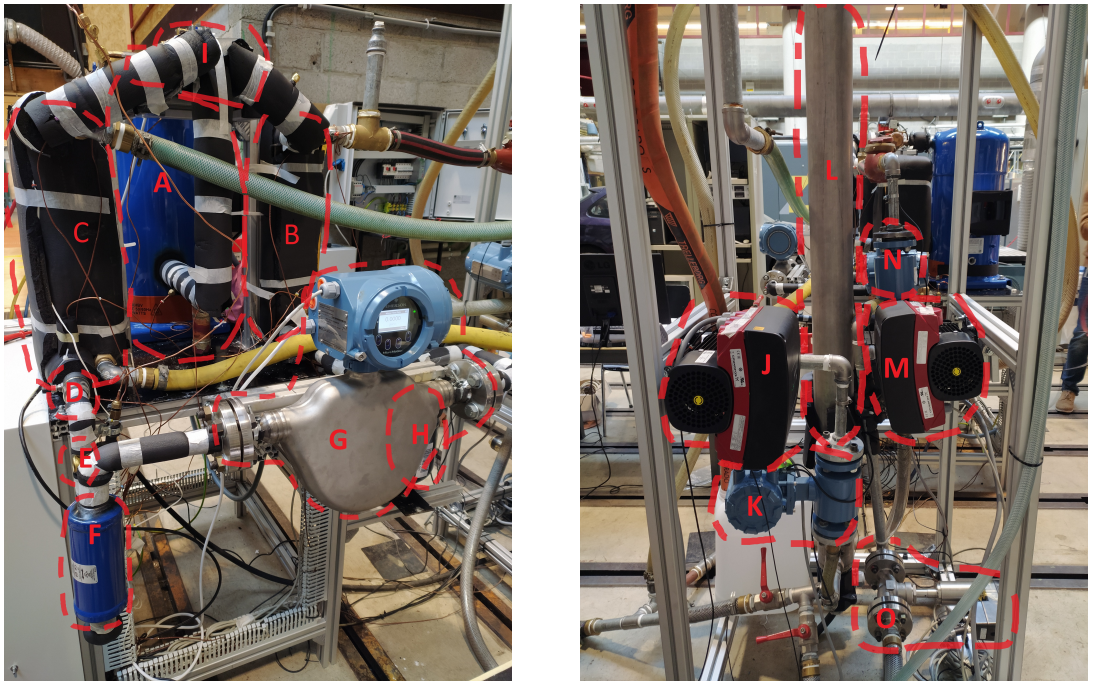

(a) (b)

Figure 2.4: Actual mounted assembly for heat pump (a), and secondary loops (b).

Chapter 3

Experimental results

3.1 Data reduction

This section describes the equations that are used to assess the heat pump performances from the experimental campaign.

- **Compressor**
  The compression work undergone by the refrigerant in the compressor is described by Equation 3.1.

$$\dot{W}_{cmp} = \dot{m}_{wf} \cdot (h_{cmp,ex} - h_{cmp,su}), \tag{3.1}$$

  where $h_{cmp,ex}$ and $h_{cmp,su}$ are the enthalpy of the refrigerant at the compressor supply and exhaust, respectively.

  The compressor performances are studied through the isentropic and volumetric efficiencies, defined by Equations 3.2 and 3.3:

$$\epsilon_{is} = \frac{\dot{m}_{wf} \cdot (h_{cmp,ex,is} - h_{cmp,su})}{\dot{W}_{cmp,elec}}, \tag{3.2}$$

$$\epsilon_{vol} = \frac{\dot{V}_{wf,su}}{\dot{V}_{wf,th}}, \tag{3.3}$$

  where $h_{cmp,ex,is}$ is the compressor exhaust enthalpy for an isentropic compression, $\dot{W}_{cmp,elec}$ the electrical consumption of the compressor. $\dot{V}_{wf,su}$ is the actual volumetric flow rate delivered by compressor and $\dot{V}_{wf,th}$ the theoretical volumetric flow rate. They are defined by Equations 3.4 and 3.5 .

$$\dot{V}_{wf,su} = \frac{\dot{m}_{wf}}{\rho_{cmp,su}}, \tag{3.4}$$

$$\dot{V}_{wf,th} = \frac{V_s \cdot N}{60}, \tag{3.5}$$

where $\rho_{cmp,su}$ is the density of the fluid at the compressor inlet, V_s is the compressor swept volume and N is the compressor rotational speed.

- **Heat exchangers**
  The thermal heat transfers occurring in the condenser and in the evaporator are defined by Equations 3.6 and 3.7:

$$\begin{aligned} \dot{Q}_{cd,wf} &= \dot{m}_{wf} \cdot (h_{cd,wf,su} - h_{cd,wf,ex}), \\ \dot{Q}_{cd,sf} &= \dot{m}_{cd,sf} \cdot cp_{cd,sf,m} \cdot (T_{cd,sf,ex} - T_{cd,sf,su}), \end{aligned} \tag{3.6}$$

$$\begin{aligned} \dot{Q}_{ev,wf} &= \dot{m}_{wf} \cdot (h_{ev,wf,ex} - h_{ev,wf,su}), \\ \dot{Q}_{ev,sf} &= \dot{m}_{ev,sf} \cdot cp_{ev,sf,m} \cdot (T_{ev,sf,su} - T_{ev,sf,ex}), \end{aligned} \tag{3.7}$$

  where $cp_{cd,sf,m}$ and $cp_{ev,sf,m}$ are the mean specific heat capacity of the water and glycol water mixture, respectively.

- **Coefficient of performance**
  The coefficient of performance of the heat pump is assessed with Equation

$$COP = \frac{\dot{Q}_{cd}}{\dot{P}_{elec,cmp} + \dot{P}_{elec,aux}}, \tag{3.8}$$

  where $\dot{P}_{elec,cmp}$ is the electrical consumption of the compressor and $\dot{P}_{elec,aux}$ is the electrical consumption of the auxiliaries (i.e. defined in Section 3.4).

3.2 Experimental methodology

The test campaign has been conducted during seven weeks and a set of 157 steady-state points is obtained. Each point is recorded for 10 minutes and the performance of the heat pump is assessed through the average of each measurement. This amount of time allows the lessening of the measured noise and the obtention of an average temperature differing from less than $0.23°C$ from the desired temperature. The goal of this experimental campaign being the characterisation of the heat pump behaviour, testing is made over a wide range of conditions. The secondary fluid inlet temperature of the evaporator $T_{ev,sf,su}$ and the water condenser outlet temperature $T_{cd,sf,ex}$ are varied from $5°C$ to 15°C and 25 to 45°C respectively, each with $5°C$ step. Those ranges of temperature are chosen to characterise a heat pump in a typical European environment to produce water for floor heating. The heat pump has been designed as a geothermal one but it has been suggested that the definitive

commercialised unit could be an air-to-water heat pump. The secondary fluid inlet temperature of the evaporator has therefore also been tested down to -15° for this reason, this temperature being the minimal one allowed by the 30% Ethylene Glycol mixture. It was also decided to test the heat pump unit up to 55°C for radiator heating. Since the maximum allowable pressure of the employed sensor is $16bar\,(g)$, it limits the maximum condensation temperature to be $61.5°C$. Considering a usual 5-6 pinch in the heat exchanger, the heat pump is further tested to achieve a maximum of $55°C$ of water temperature at the condenser outlet. Condensation temperature higher than $50°C$ is well within the compressor envelope that can be operated at a maximum condensing temperature of $68°C$. However, since the maximum available power from the CHP unit is 10kWe, it has been decided to test the unit so that the maximum electric power withdrawned by the compressor is 10kW. The water temperature at the condenser outlet is therefore also limited by the electric power and a $55°C$ temperature can sometimes not be achieved. In a similar way, evaporating temperatures is limited and the water temperature at the inlet of the evaporator, in some cases, can not be lowered too much.

An experimental campaign is conducted by varying the temperature of the secondary fluids at two rotational speed of the scroll compressor (i.e. 2400 and 3000rpm). In order to maintain consistency between each point, the mass flow of water on condenser side $\dot{m}_{cd}$ and glycol-water on evaporator side $\dot{m}_{ev}$ are both fixed at $1.1l/s$ to allow a water temperature lift between 5 and $10°C$. However, some tests are conducted at higher lift and flow rate is therefore varied. The range of tested condensing and evaporating pressure are shown in Figure 3.1.

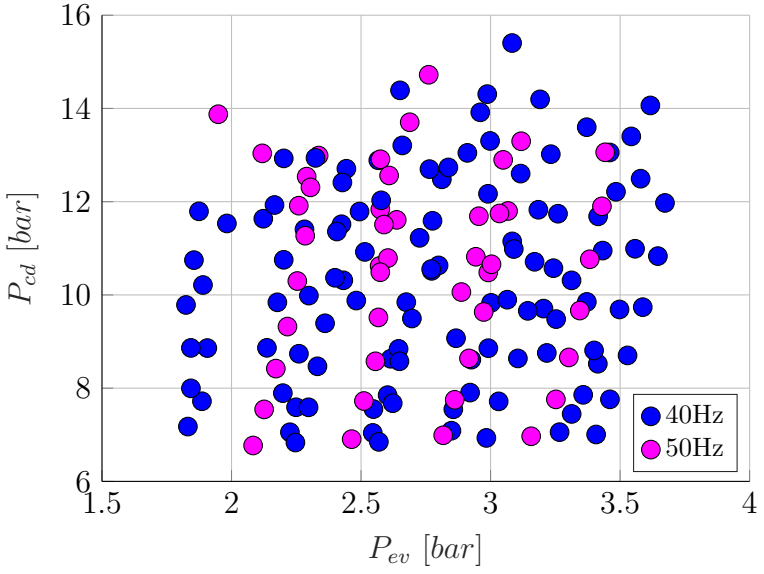

Figure 3.1: Test matrix of the experimental campaign.

The heat pump is tested in four main conditions. At first, tests are carried out while being overcharged (i.e. refrigerant charge is too important for the system). As it will be discussed in Section 3.6, subcooling is large when the heat pump is overcharged, causing pressure and therefore electrical consumption to increase. An overcharged heat pump is therefore not desired in a commercial application. Secondly, the optimal charge of refrigerant is found and the heat pump is being tested with a water temperature lift of around $10°C$ on the condenser side. Thirdly, tests are carried with a larger lift (i.e. with tap water entering the condenser). Fourthly, some tests are performed to assess the effect of overheating. Finally, the effect of a liquid receiver after the condenser is also studied.

3.3 PID controller

PID controllers are implemented to set the secondary fluid temperatures to the desired values. $T_{ev,sf,su}$ is controlled through the power sent to the heating resistance while $T_{cd,sf,ex}$ is controlled through the opening of the motorized globe valve. The heating resistance and the valve allow to respectively control the heat load of the hot water loop and the amount of freshwater added to the cold water loop.

A PID controller is a control system ensuring a measured process variable (PV) to reach a desired setpoint (SP) by adjusting a control variable $u(t)$. A PID controller calculates the error value $e(t)$ between SP and PV and ajdust $u(t)$ to minimize this error. The overall control function is written as:

$$u(t) = K_{\mathrm{c}} \left(e(t) + \frac{1}{T_{\mathrm{i}}} \int_0^t e(t)dt + T_{\mathrm{d}} \frac{de(t)}{dt} \right), \tag{3.9}$$

where K_c is the proportional gain, T_i the integration time, T_d the derivative time, de the change in error value and dt the change in time.

The parameters of the Proportional Integral Derivative (PID) controller of the evaporator loop have been determined by monitoring the system behaviour under step changes. This loop is subject to high delay time between a change in the power sent by the heating resistance and its effect on $T_{ev,sf,su}$. The PID parameters needs to be correctly optimised to allow a good and fast control of the loop. First, the system is tested under four values of the proportional term K_c while keeping T_i and T_d constant. One can see in Figure 3.2a that high values of K_c lead to large overshoots which are not a desirable behaviour. The proportional gain is chosen to be 0.5 in order to have acceptable overshoot while keeping its value high enough to sustain system disturbances. Then, the response of $T_{ev,sf,su}$ is studied for four values of the integral term T_i while keeping the two other parameters constant. The result is

shown in Figure 3.2b and the value of T_i is chosen equal to $0.5min$ to obtain a fast convergence while avoiding too large overshoot. Finally, one can see in Figure 3.2c the impact of the derivative term T_d, which has little influence. T_d is chosen equal to $0.5min$. The parameters of the PID controller of the condenser loop have been determined by manual tuning as well.

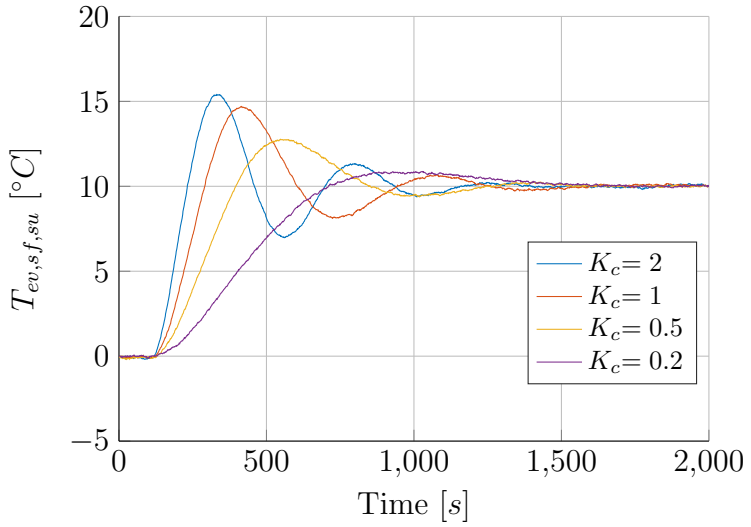

(a) Response of $T_{ev,sf,su}$ to step change, for four values of K_c (T_i=0.5 min and T_d=0.5min).

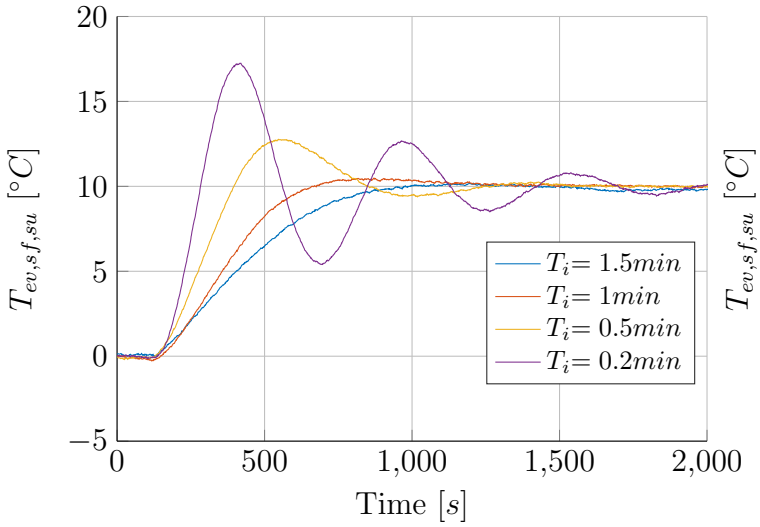

(b) Response of $T_{ev,sf,su}$ to step change, for four values of T_i (K_c=0.5 min and T_d=0.5min).

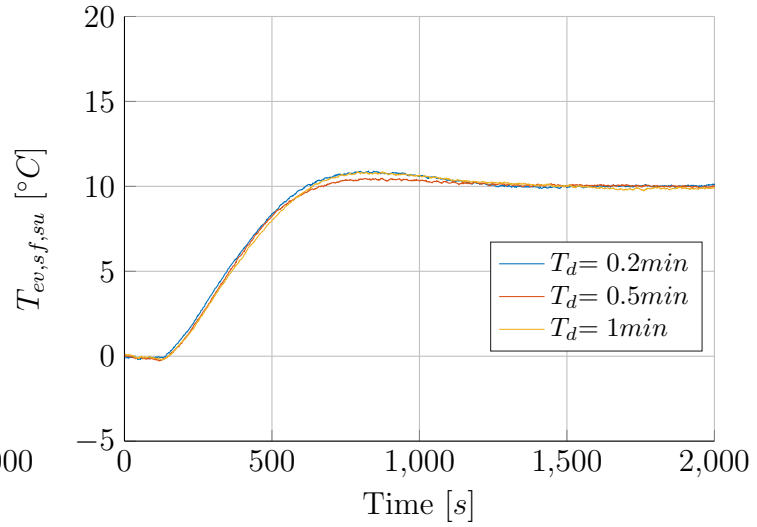

(c) Response of $T_{ev,sf,su}$ to step change, for three values of T_d (K_c=0.5 min and T_i=1min).

Figure 3.2: Effect of varying parameters (K_c, T_i and T_d) on the evaporator loop.

The PID controllers parameters are listed in Table 3.3a. The responses of the secondary fluid loops to a step change are shown in Figures 3.3a and 3.3b. One can

see in Figure 3.3a that the settling time is long, almost 1500s. Finding the proper parameters of each system is therefore of significant importance. The chosen ones allow having a short rise time and small steady-state error.

Table 3.1: PID controllers parameters.

	Resistance control	Valve control
Proportional gain K_c [-]	0.5	-2.5
Integral time T_i [min]	1	2.2
Derivative time T_d [min]	0.5	0.01

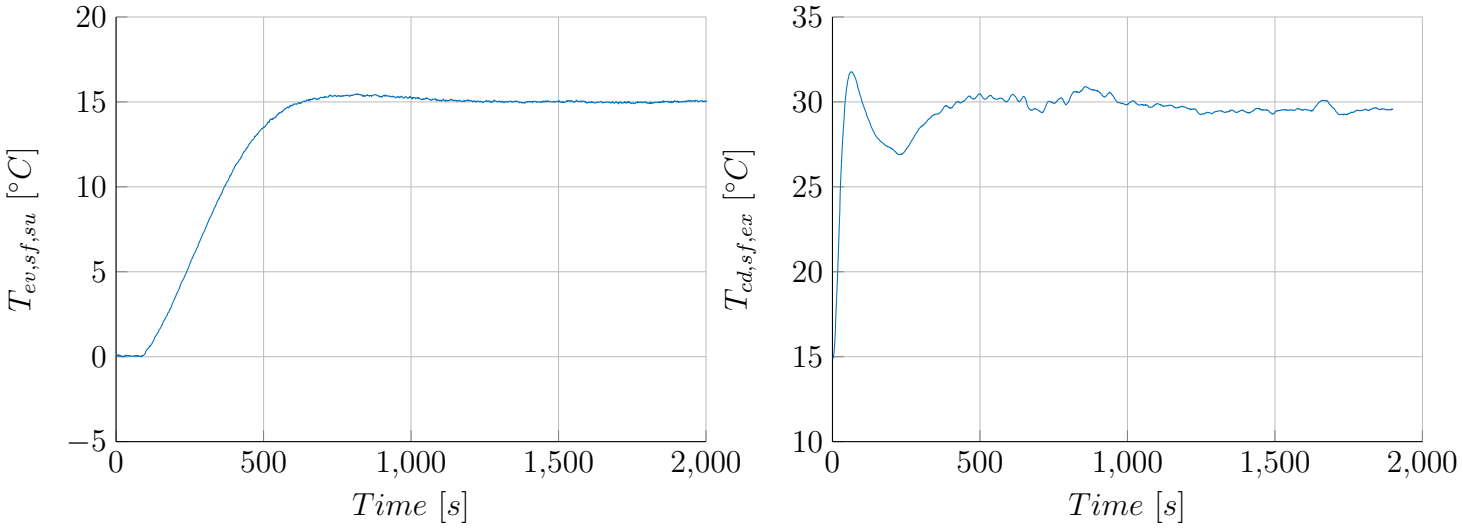

(a) Time evolution of $T_{ev,sf,su}$ subjected to a 5°C increases with the heating resistance controlled by a PID.

(b) Time evolution of $T_{cd,sf,ex}$ subjected to a 15°C step change with the globe valve controlled by a PID.

Figure 3.3: Response of the system to step changes.

3.4 Electrical consumption of the auxiliaries

The main electrical consumption of the water to water heat pump is brought by the compressor, but the auxiliaries also contribute to the HP performance characterisation. The auxiliaries to be considered in this case are the only two circulators that are supplying secondary fluids to the condenser and evaporator. The consumption of the other components, such as the motorized globe valve, the expansion valve or

the sensors, are assumed negligible.

The consumption of the circulators is not recorded during each test as they are not wired to have analog output. However, the consumption can be read in real-time through a smartphone via the Grundfos GO remote application. The circulator consumption as a function of its voltage analog input can be found in Figure 3.4. The cold and hot water loop circulators are consuming between 370 and 470W in all. This consumption is marginal in comparison with the compressor electrical power but is still taken into account in the performance evaluation. It is worth noting that the circulator, supplying glycol water to the evaporator, is consuming a substantial part of the auxiliary power. Whereas, the circulator supplying water to the condenser is only re-circulating a small quantity of the freshwater to maintain the condenser inlet temperature and therefore consumes less than 200W.

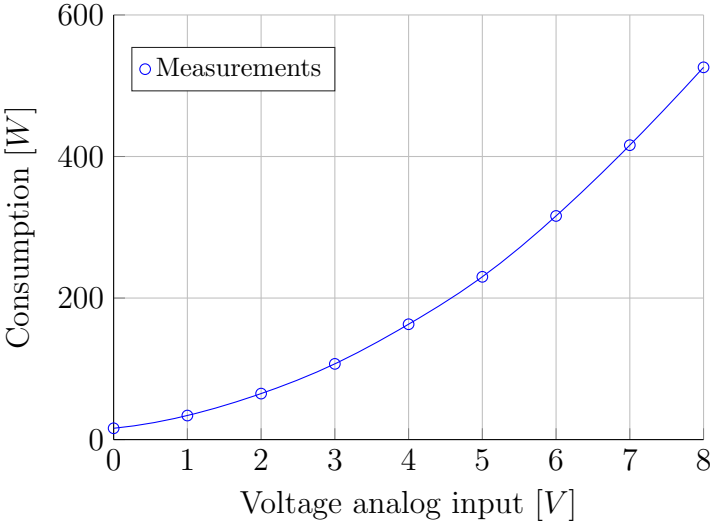

Figure 3.4: Circulator consumption function of the voltage analog input.

3.5 Measurements validation

Experimental campaigns are always subjected to measurement uncertainties which are caused by limitations of the measuring instruments, reading errors or sensor malfunctions. It is therefore of significant importance to perform measurement redundancies to validate the test campaign.

The working fluid temperature at the inlet of the evaporator is not consistent with the others measurements. As seen in Figure 3.5, the temperatures at the evaporator inlet (1) and at compressor exhaust (5) seem incorrect. The evaporator inlet temperature is above the saturation temperature computed from the evaporating pressure. This temperature difference varies between 0 and 6°C in the experimental

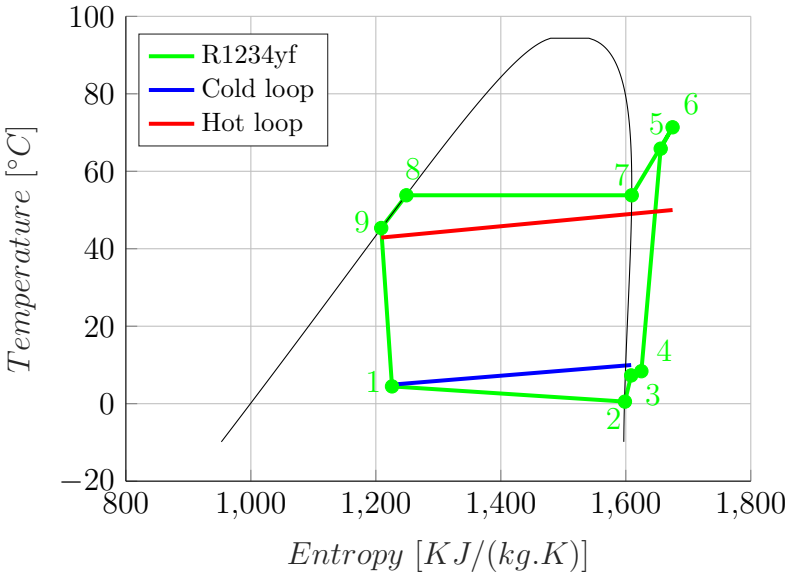

Figure 3.5: TS diagram obtained with all the measurements.

campaign, as shown in Figure 3.6. This is not possible, either the temperature or the pressure measurement is wrong. One can see in Figure 3.7 that the difference between $T_{ev,sf,ex}$ and $T_{ev,wf,su}$, called pinch point, is in some instances negative. The pinch point is the minimum temperature difference between a hot and a cold stream which limits the maximum heat that can be transferred in a heat exchanger. This temperature difference equals to zero if the heat exchanger area is infinite. In practical applications, the pinch point can never reach zero and more than ever can not be negative. Figure 3.7 therefore shows unrealistic measurements. Either the outlet temperature of the glycol-water solution on the evaporator side or the evaporation temperature measurement is wrong. The working fluid temperature at the inlet of the evaporator shows inconsistency in both case, this measurement is therefore questioned

The temperature at the compressor exhaust is also not consistent with the other measurements. The temperature at the compressor exhaust (5), as illustrated in Figure 3.5, is lower than the temperature at the condenser inlet (6). Ideally, those two temperatures should be equal. In a realistic situation, heat transfer occurs in the four-way valve and the fluid is cooled down between the exit of the compressor and the supply of the condenser. However, the opposite is shown on the graph. One can see in Figure 3.9 that $T_{cd,wf,su}$ is always higher than $T_{cmp,wf,ex}$ and that the temperature difference increases with the temperature at the compressor outlet. Either $T_{cd,wf,su}$, $T_{cmp,wf,ex}$ or both measurements are wrong. The electrical power consumed by the compressor is compared to the work performed on the refrigerant by the compressor which, as a remember, is calculated by:

$$\dot{W}_{measured} = \dot{m}_{ref} \cdot (h_{cmp,ex} - h_{cmp,su}), \tag{3.10}$$

where $h_{cmp,su}$ is the exhaust enthalpy of the compressor, computed from the high pressure $P_{cmp,ex}$ and the exhaust temperature (i.e. $T_{cd,wf,su}$ or $T_{cmp,wf,ex}$). The comparison between the compressor consumption measured at the inverter and the consumption calculated from cycle conditions, for both exhaust temperatures, are shown in Figures 3.8a and 3.8b. It clearly demonstrates improper energy balance when $T_{cmp,wf,ex}$ is used for the exhaust temperature of the compressor, especially at high power. Indeed, Figure 3.10 shows that $T_{cmp,wf,ex}$ increases with the compressor consumption while Figure 3.9 shows that the difference between $T_{cd,wf,su}$ and $T_{cmp,wf,ex}$) increases with $T_{cmp,wf,ex}$. Conversely, a proper heat balance on the compressor is obtained when $T_{cd,wf,su}$ is used as the temperature of the compressor outlet.

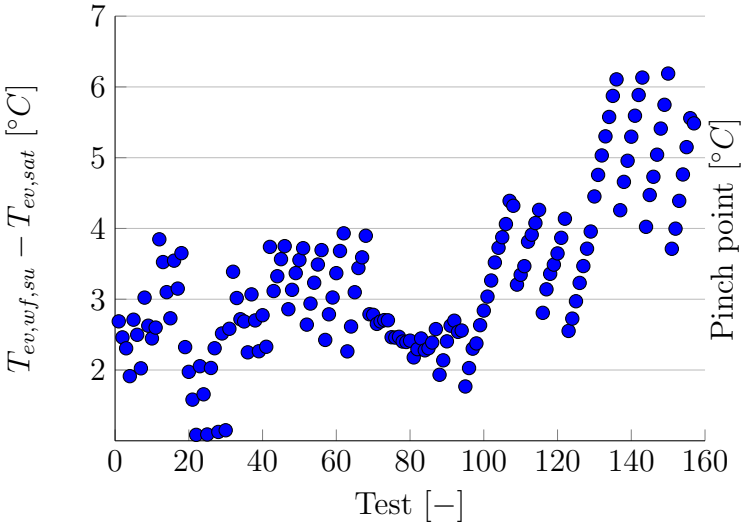

Figure 3.6: Difference between $T_{ev,wf,su}$ and $T_{ev,sat}$.

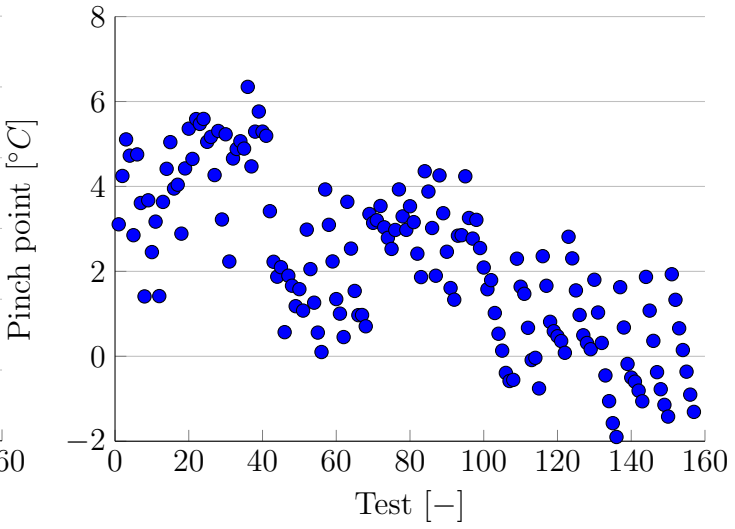

Figure 3.7: Pinch point at the evaporator.

The above discussion has shown inaccuracies for the temperatures at the evaporator inlet and at the compressor exhaust. It is important to emphasize that those two temperature measurements are taken on the copper tube surfaces while all the other temperature sensors are displaced in immersion sleeves. This might be the reason for the tremendous errors in those two measurements.
It has been decided not to further consider these erroneous readings from the sensors mounted at the inlet of evaporator and outlet of the compressor. The temperature at the evaporator inlet is estimated by knowing the evaporating pressure and by making the assumption of an isenthalpic expansion (State 9 - 1 in Figure 3.5), the state

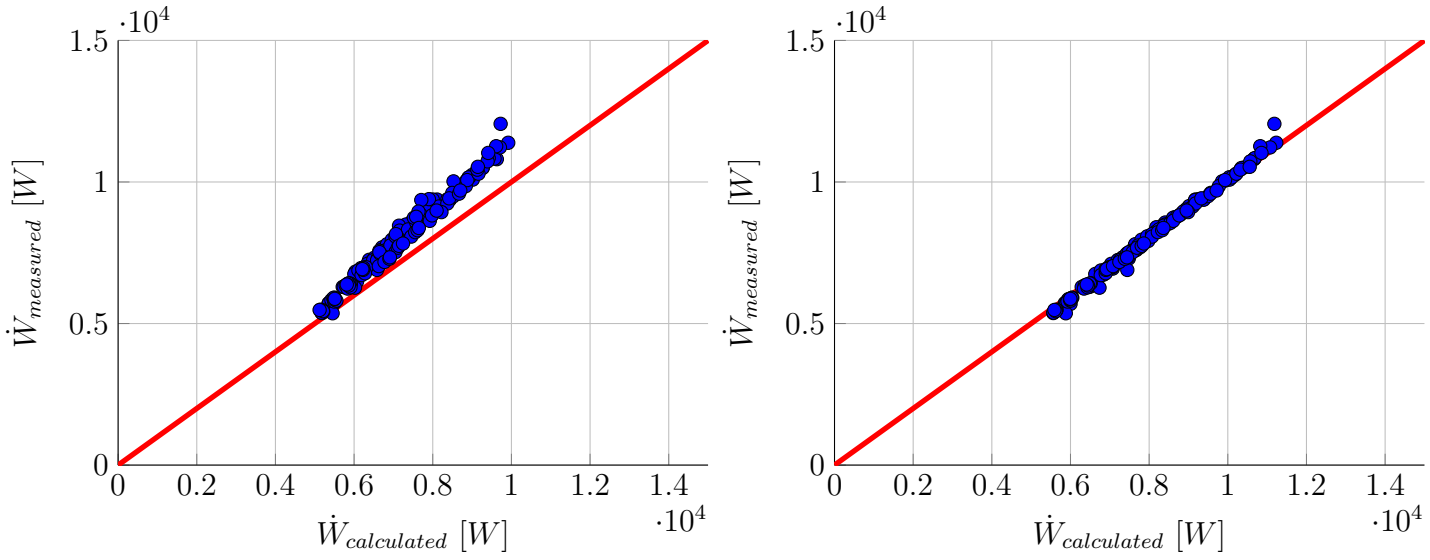

Figure 3.8: Comparison between the compressor consumption measured at the inverter and the consumption calculated from cycle conditions, based on $T_{ex,cmp}$ for the exhaust temperature of the compressor (a), and based on $T_{cd,su}$ for the exhaust temperature of the compressor (b).

of the refrigerant before the EEV being known. The temperature at the compressor exhaust is measured at the condenser inlet. The impact of the four-way valve can therefore not be studied as the fluid state is unknown at its inlet.

Heat balances are performed on the two heat exchangers, by taking into account the two temperature corrections. They are computed with Equation 3.11. This allows comparing the heat transfer rates of the secondary fluid and refrigerant that take place in the evaporator and the condenser. With accurate sensors, heat transfer rates should be equal.

$$\dot{m}_{wf}\left(h_{wf,su} - h_{wf,ex}\right) = \dot{m}_{sf} \cdot cp_w \left(t_{sf,ex} - t_{sf,su}\right). \tag{3.11}$$

One can see in Figures 3.11a and 3.11b that consistent results are retrieved, the maximum relative error being 8.13% and 10.52% for the condenser and evaporator respectively.

Finally, a global energy residual is computed with Equation 3.12, where heat transfer in the heat exchangers is assessed by knowing the state of the working fluid or of the secondary fluid.

$$Res_{global} = \dot{W}_{cmp} + \dot{Q}_{ev} - \dot{Q}_{cd} \tag{3.12}$$

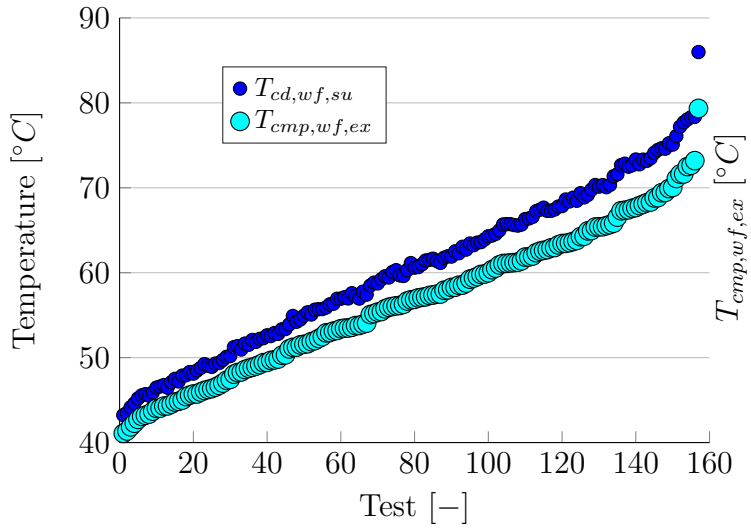

Figure 3.9: Temperature at the compressor outlet, before and after the four-way valve.

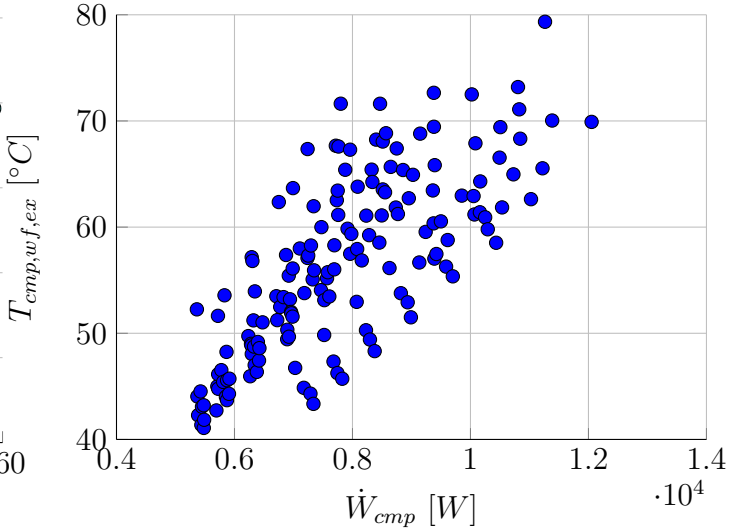

Figure 3.10: Temperature at the compressor outlet function of the compressor consumption.

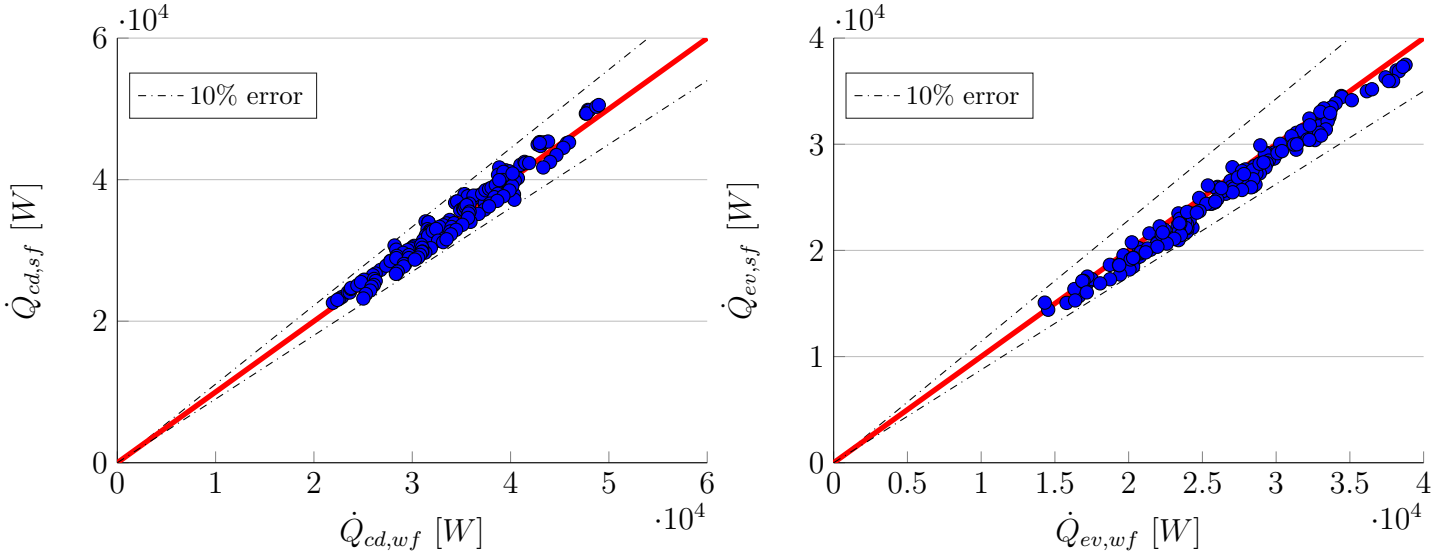

(a) (b)

Figure 3.11: Condenser heat balance (a), and evaporator heat balance (b).

As shown in Figure 3.12a, the global energy residual computed with the working fluid measurements is lower than 1000W and has a mean absolute value of 329.62W. The order of magnitude of the residual is also the one of the heat losses to the ambiant air calculated by the heat pump model in the next chapter. As the heat pump produces between 20kW and 50kW, one can say that working fluid measurements are reliable. The secondary fluids residuals are much greater, its mean absolute value being 1605.1W. As a consequence, heat load in the two heat exchangers are computed with the working fluid measurements in the following discussion.

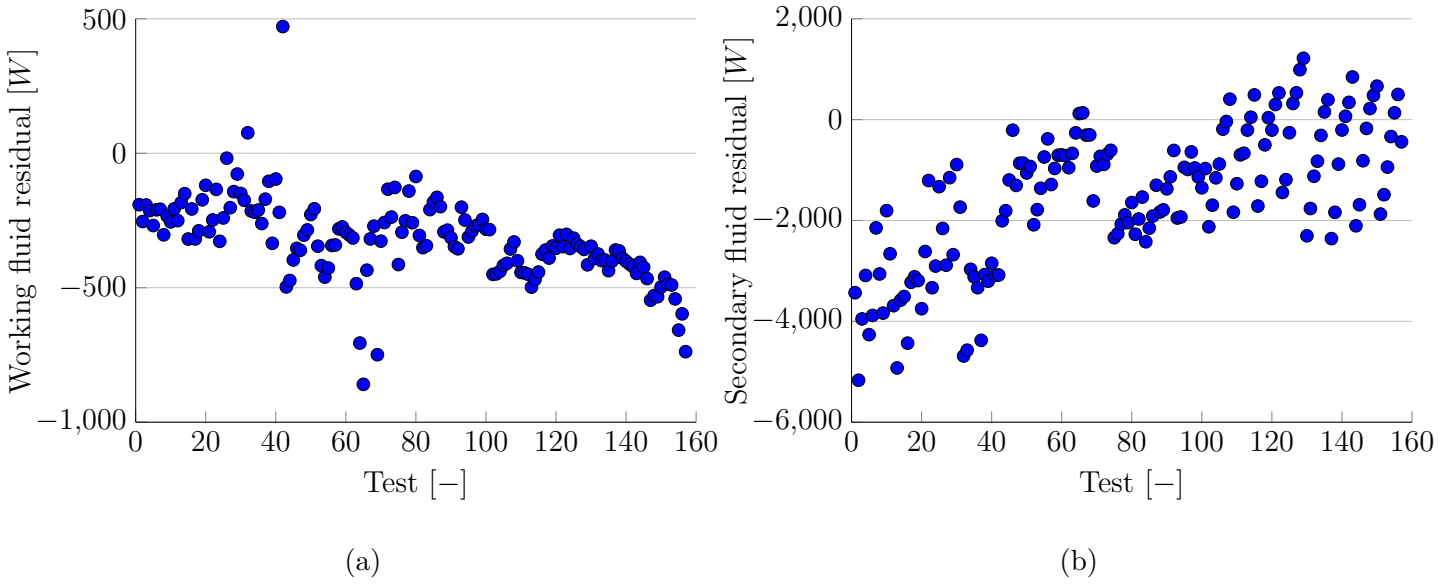

(a) (b)

Figure 3.12: Working fluid residual (a), and secondary fluid residual (b).

3.6 Appropriate refrigerant charge

The heat pump performances are linked to the refrigerant charge if no buffer (i.e. liquid receiver) is present in the system. Figures 3.13a and 3.13b illustrate the behaviour of the heat pump when being correctly charged and overcharged respectively, with the same external conditions (i.e. same $T_{ev,sf,su}$ and $T_{cd,sf,ex}$). One can see in Figure 3.13a that the condensing temperature is set close to $T_{cd,sf,ex}$. Figure 3.13b shows that the condensation temperature is about 10°C higher than in the appropriate charged heat pump. When the system is overcharged, the charge surplus sets in the condenser in liquid state. The area used by saturated liquid increases at the expense of the one used for latent heat transfer and subcooling therefore increases from 5°C to 24.5°C. It can be observed that having a high subcooling rises the condensing pressure, which increases the consumed electrical power by the compressor. As a matter of fact, the electrical power consumed by the compressor is 7607W when the charge is $5.24kg$ and 9021W when the charge is $6.55kg$, as seen in Table 3.2. It is worth noting that the heat load of the condenser increases with subcooling as the change in enthalpy rises. However, this positive impact is not important enough to counterbalance the increase of the compressor work: COP is higher when an appropriate charge of refrigerant is added to the system.

When the optimum charge is added to the system, one can see in Figure 3.14a that the subcooling is highly dependent on the conditions of the secondary fluid: it increases with increasing $T_{cd,sf,ex}$ and decreasing $T_{ev,sf,su}$. Figure 3.14b shows that subcooling also increases with the rotational speed of the compressor. The appropriate refrigerant charge is found by minimising it while having liquid fluid

	Correctly charged	Overcharged
Mass of refrigerant [kg]	5.24	6.55
$\dot{W}_{elec}$ [W]	7607	9021
$\dot{Q}_{cd}$ [W]	37380	39131
COP [-]	4.575	4.065

Table 3.2: Characteristics of the heat pump when being correctly charged and overcharged.

at the sight glass, i.e. entering the expansion valve. This is done at 40Hz with $T_{ev,sf,su}$=15°C, this is necessary to ensure sufficient subcooling over the entire range of HP working conditions.

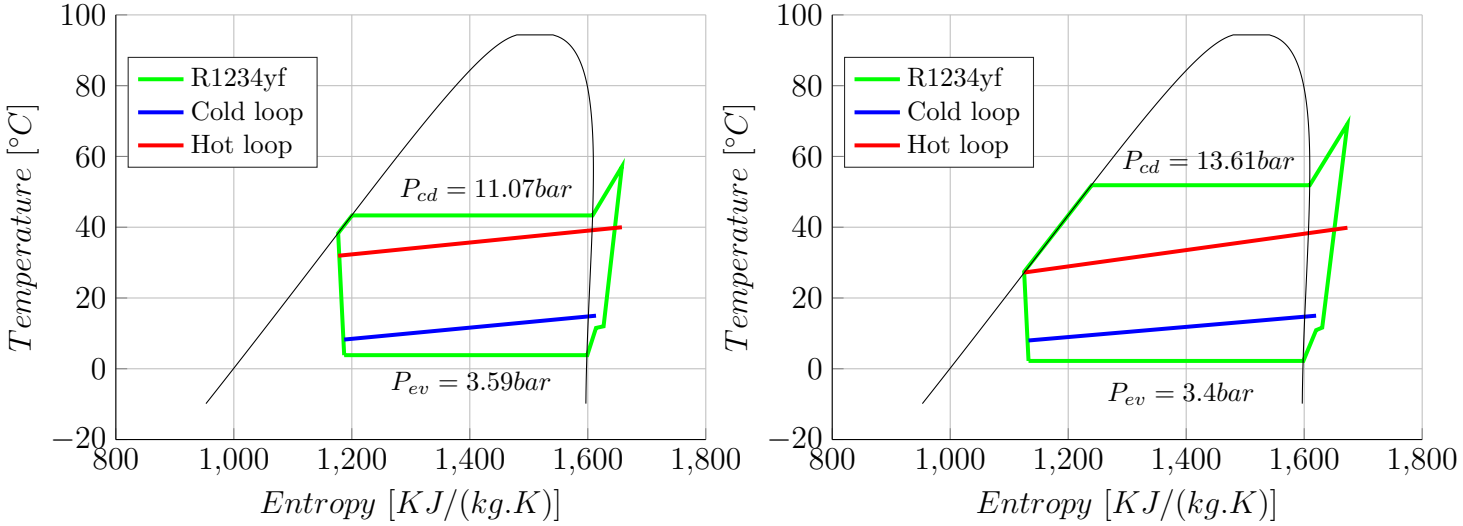

(a) (b)

Figure 3.13: T-s diagram when the heat pump is correctly charged (a), and when the heat pump is overcharged (b).

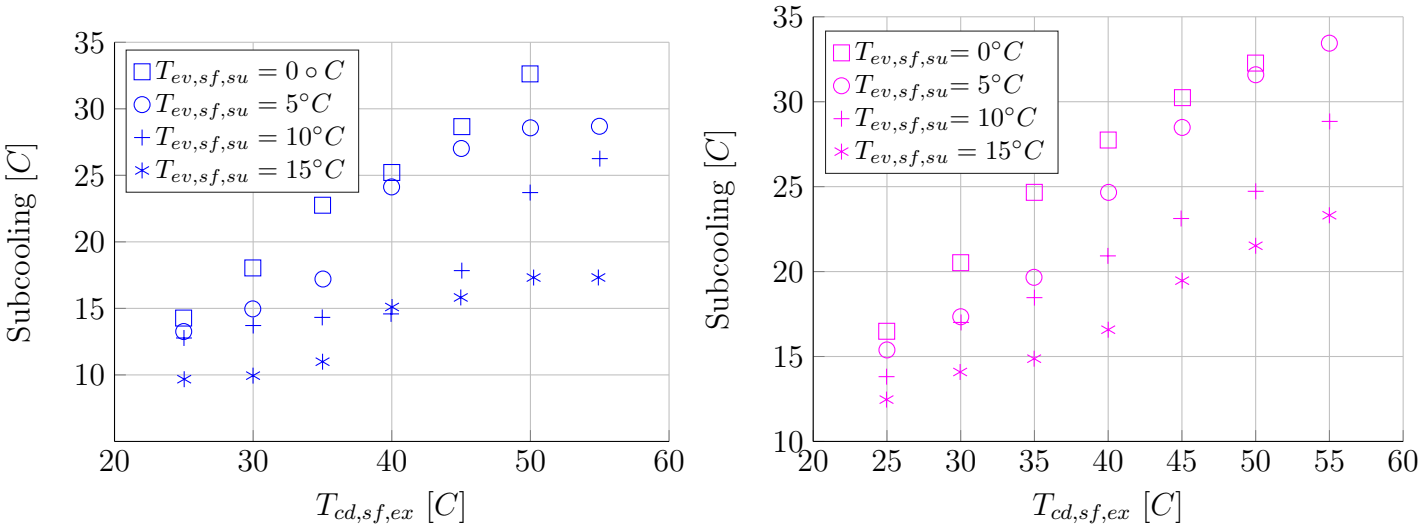

(a) (b)

Figure 3.14: Subcooling function of the secondary fluid temperatures when tap water enters the condenser at 40Hz (a), and 50Hz (b).

3.7 Cycle performance

The heat pump cycle performance is assessed in terms of coefficient of performance (COP). It should be noted that performances are only assessed in heating mode since no experimentation was held in cooling mode. The coefficient of performance of the heat pump defines the relationship between the heating or cooling power produced by the heat pump, and the electrical power consumed by the compressor. COP describes an energy efficiency: The higher the coefficient, the more efficient the heat pump.

The performance map of the heat pump, with a compressor frequency of 40Hz and in nominal condition (i.e. secondary fluid mass flow rate of $1.1kg/s$), is displayed in Figure 3.15. As expected, COP increases with increasing $T_{ev,sf,su}$ and decreasing $T_{cd,sf,ex}$. An increase of the outlet temperature of the generated warm water leads to a drop of the heat pump performances. The more the water is heated up, the less efficient the system is. This explains the choice of selling the product for floor heating. Moreover, the heat pump is a geothermal one. It allows taking advantage of a relatively consistent evaporator supply temperature and therefore allows avoiding a large COP fluctuation of air-source heat pump. As heating occurs most of the time when the outdoor temperature is low, the ground temperature is nearly always higher than the ambient temperature when the heat pump is turned on for floor heating. In Belgium, ground temperature is approximately $10°C$, which brings the COP for floor heating at $35°C$ to a value of 4.43. The heat pump design has been

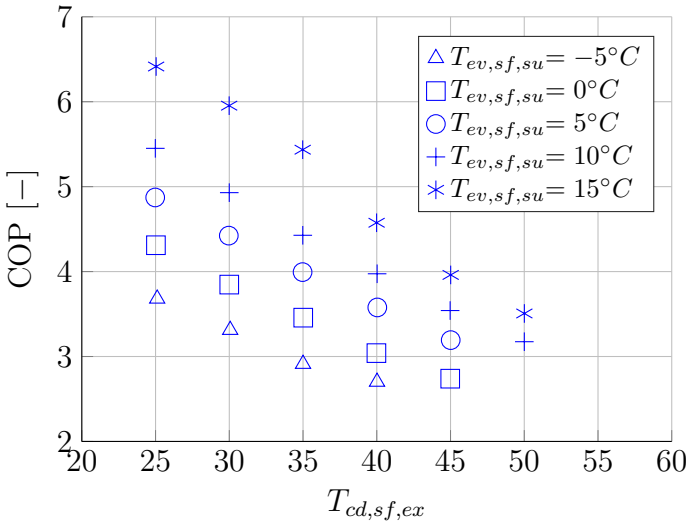

Figure 3.15: Heat pump COP at 40Hz, in nominal conditions.

made to reach a COP of 5 with geothermal heat at $12°C$ and a spline interpolation allows to approximate the real COP obtained in those conditions, which is 4.72. The actual COP is lower than the predicted one, even though the heat pump shows a very efficient behaviour: for 1kW of electricity, the system produces 4.72kW of heat.

It is worth noting that the performances of the R1234yf heat pump at 50Hz, in nominal conditions, could not be characterised even though it was planned. This is due to the fact that one of the two Grundfoss circulators got broken and could not be replaced on time to continue testing with preheated tap water in the condenser.

3.8 Compressor performances

The compressor performances are studied through the isentropic and volumetric efficiencies, defined by Equations 3.2 and 3.3 respectively.

Isentropic efficiency, with a mean value of 0.60, varies between 0.50 and 0.71. The maximum values are reached for compression ratio around 3 and for compressor frequency of $40Hz$, as it can be seen in Figure 3.16a. Figure 3.16b shows that the scroll compressor has low efficiency at low mass flow rate. Large deviations of the efficiency at constant compression ratio or constant mass flow rate are observed.

A continuity between some points can be observed in both Figures 3.16a and 3.16b, therefore it is studied in details to observe the impact of conditions variations. The compressor efficiency depends directly on the condensing and evaporating pressures, which are related to the secondary fluids properties. As the experimental campaign was conducted by varying the secondary fluids temperatures, the isentropic efficiency

is studied through $T_{ev,sf,su}$ and $T_{cd,sf,ex}$. The effects of the supply pressure is assessed by the heat pump model in Chapter 4. The model has shown that the isentropic efficiency increases with increasing supply compressor pressure. One can see in Figure 3.17 that the source temperature is highly impacting the scroll efficiency: the higher $T_{ev,sf,su}$, the higher the isentropic efficiency. It can also be noted that ϵ_{is} increases with $T_{cd,sf,ex}$ before reaching at maximum. At design conditions (i.e. $T_{cd,sf,ex}$=35°C and $T_{ev,sf,su}$=12°C), the isentropic efficiency value is approximately 0.67 and hence closed to the maximal value. The compressor is therefore working in optimum conditions and well-chosen.

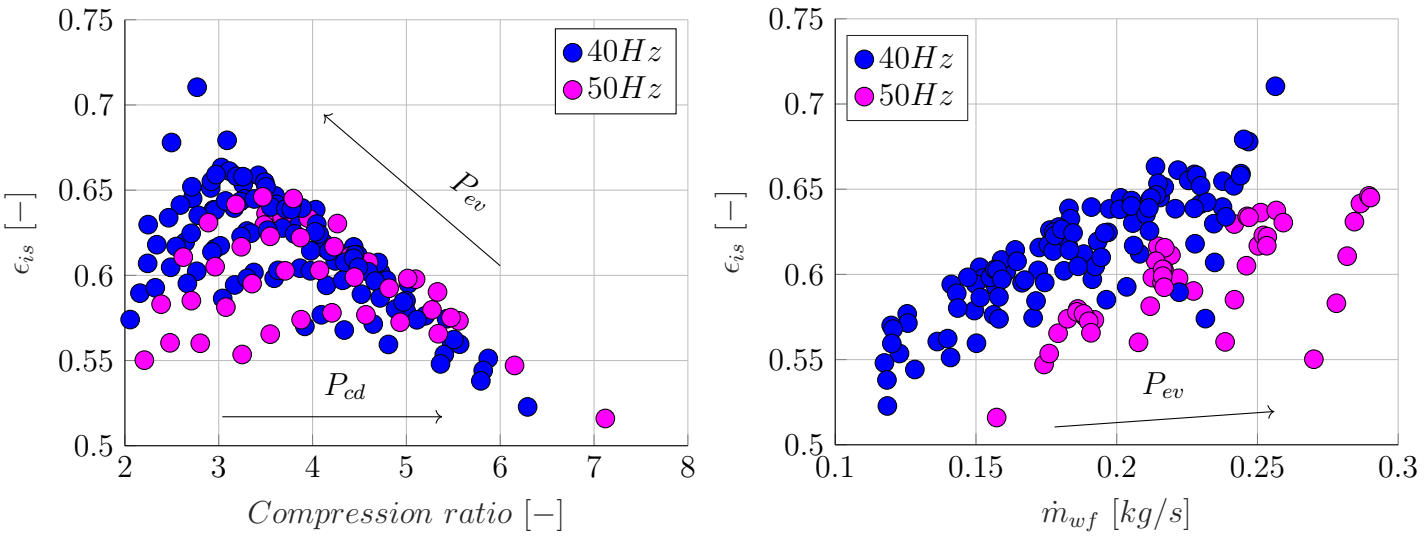

Figure 3.16: Evolution of the isentropic efficiency with the pressure ratio (a), and with the refrigerant mass flow rate (b).

The volumetric efficiency decreases with increasing compression ratio and decreasing compressor frequency, as shown in Figure 3.18a. At high compression ratio, the leakage flow between the outlet and inlet is high as the refrigerant is subjected to a high pressure difference through a leakage area. Gazes undergo re-compression and volumetric efficiency decreases. ϵ_{vol} is higher at a compressor frequency of 50Hz than 40Hz. Mass flow rate is higher at high rotational speed and, as shown in Figure 3.18b, volumetric efficiency increases with $\dot{m}_{wf}$.

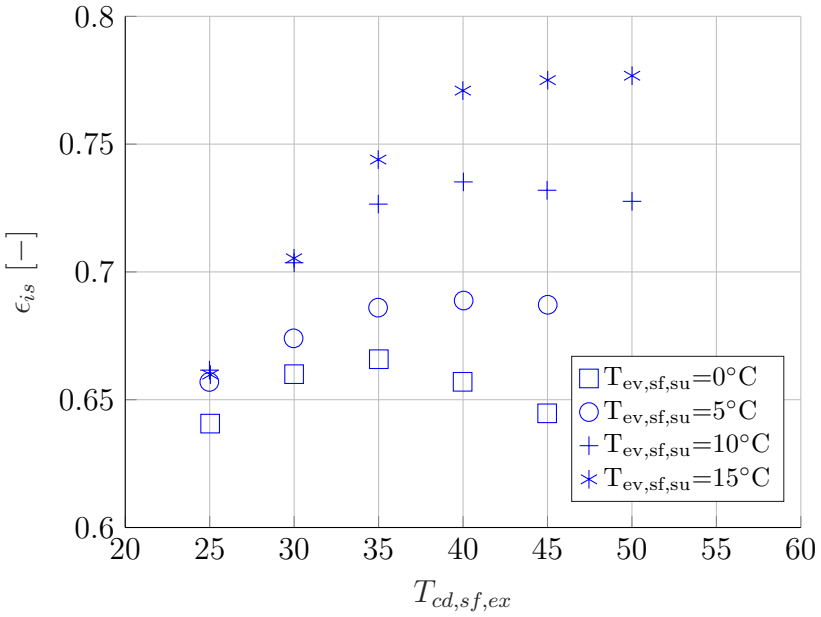

Figure 3.17: Evolution of the isentropic efficiency with $T_{cd,sf,ex}$ and $T_{ev,sf,su}$ at 40Hz and in nominal conditions.

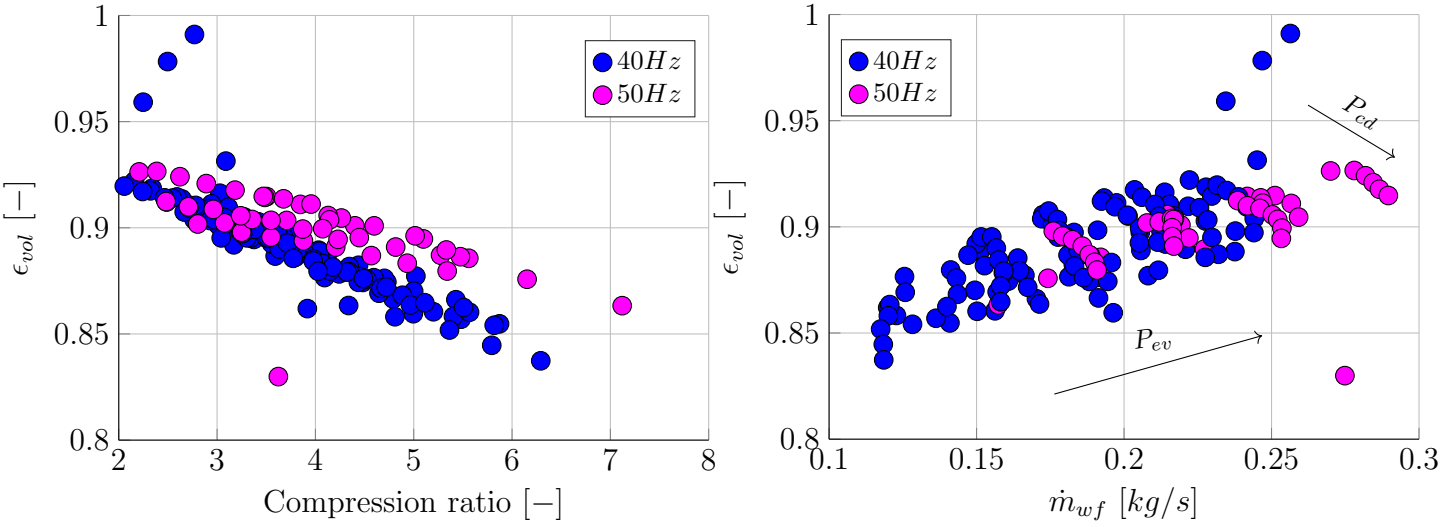

(a) (b)

Figure 3.18: Evolution of the volumetric efficiency with the pressure ratio (a), and with the working fluid flow rate (b).

3.9 Heat exchangers performances

Heat transfer in the two heat exchangers is linearly correlated with the refrigerant mass flow rate, as shown in Figures 3.19a and 3.19b. The thermal capacity is more important when the compressor frequency is high. Indeed, $\dot{m}_{wf}$ influences the heat transfer and is directly proportional to the rotational speed, as N is the compressor

rotational speed and ρ_{su} the supply density:

$$\dot{m}_{wf} = \frac{N}{60} \cdot V_s \cdot \rho_{su}, \tag{3.13}$$

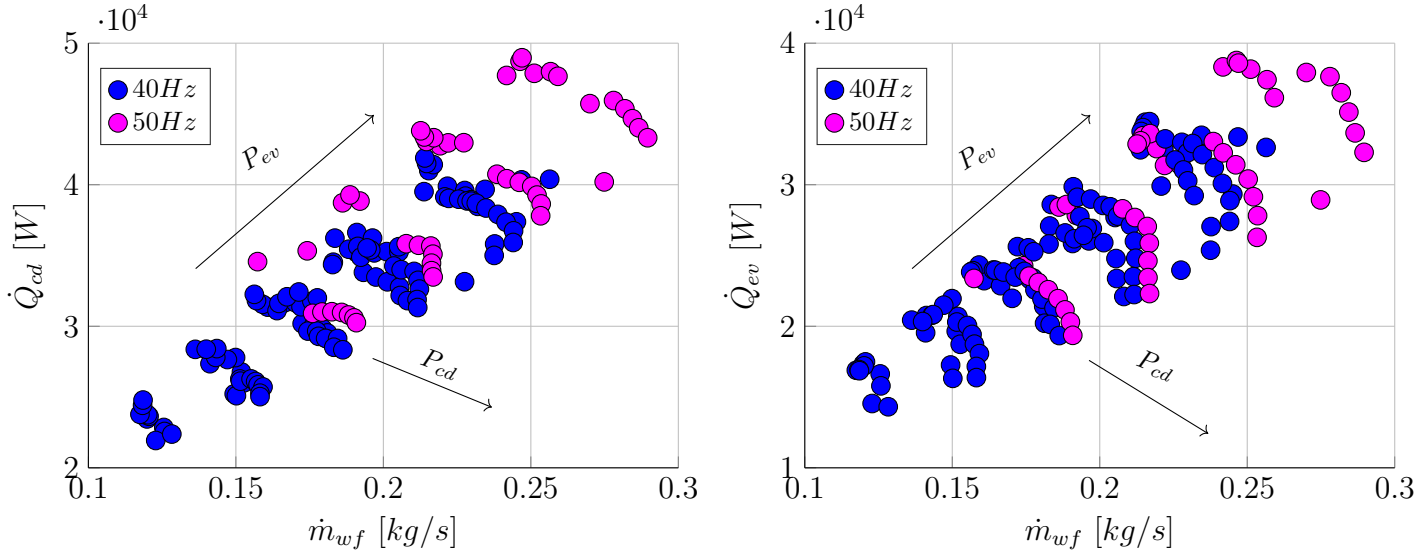

Figure 3.19: Evolution of the condenser heat load (a), and of the evaporator heat load (b) with the refrigerant mass flow rate .

The heat exchanger pinch points are an indication of its effectiveness. One can see in Figure 3.20 that the evaporator pinch point varies between almost 0 and 7°C at 50Hz, while it is almost constant and close to 3°C at 40Hz. The maximum efficiency of the heat exchanger is reached at the lowest evaporating temperature.

The thermal heat transfer in the condenser occurs at maximal efficiency when the system is overcharged, as shown in Figure 3.21a. The condenser pinch point is only dependent on the condensing temperature when a liquid receiver is used at the condenser outlet. In Figure 3.21b, it is seen that the condenser pinch increases with $T_{ev,sat}$. Figures 3.22a and 3.22b show the condenser pinch point as a function of $\dot{m}_{wf}$ and $\dot{m}_{sf,cd}$. One could see that the pinch increases with both mass flow rates in the condenser. Noteworthy, the water flow rate is approximately constant in a well-charged system with a $10K$ condenser water temperature lift, $\dot{m}_{cd}$ is therefore not influencing the HEX pinch. To conclude, the optimum heat transfer rates are obtained in overcharged heat pump, or at low flow rate and evaporating temperature.

Subcooling at the condenser outlet is not impacted by the temperature conditions in heat pumps including a liquid receiver, as indicated in Figures 3.23a and 3.23b. In a well charged system at constant water flow rate (i.e. $1.1kg/s$), subcooling slightly

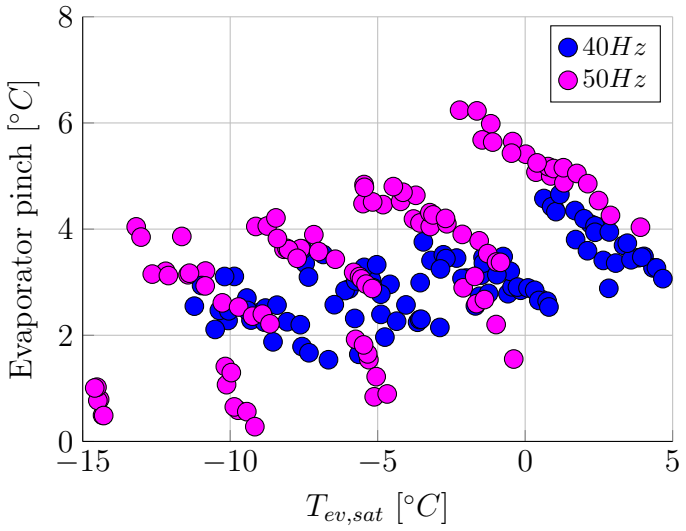

Figure 3.20: Evolution of the pinch point with $T_{ev,sat}$.

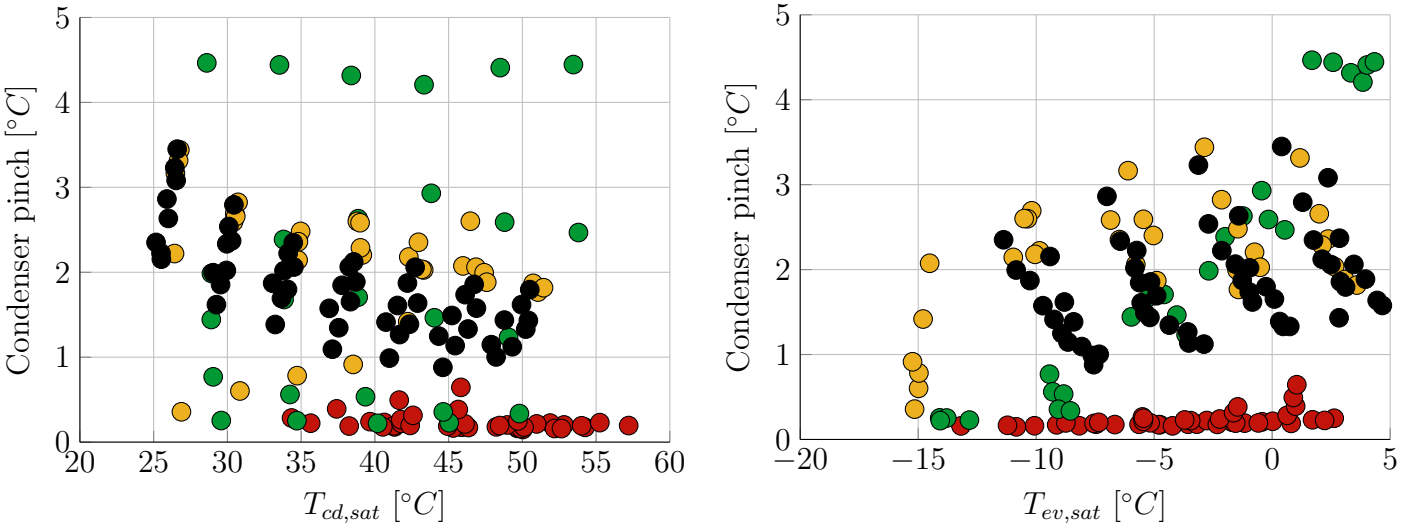

(a) (b)

Figure 3.21: Evolution of the condenser pinch point with the condensing temperature (a), and with the evaporating temperature (b) (red: overcharged system; green: well charged system with 1.1kg/s condenser water flow rate; orange: well charged system with small condenser water flow rate; black: liquid receiver added in the system with small condenser water flow rate).

decreases with increasing $T_{ev,sat}$ but is not fluctuating with $T_{cd,sat}$. In an overcharged system or at low condenser secondary fluid flow rate, subcooling increases with decreasing $T_{ev,sat}$ and increasing $T_{cd,sat}$

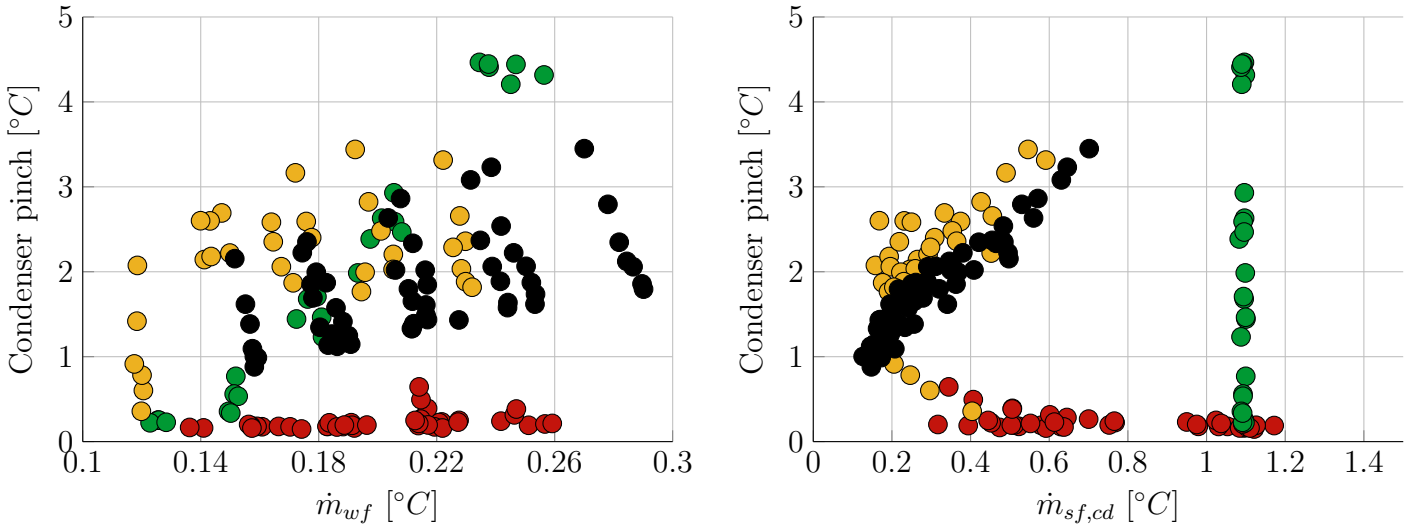

(a) (b)

Figure 3.22: Evolution of the condenser pinch point with the working fluid mass flow rate (a), and with the secondary fluid mass flow rate (b) (red: overcharged system; green: well charged system with $1.1kg/s$ condenser water flow rate; orange: well charged system with small condenser water flow rate; black: liquid receiver added in the system with small condenser water flow rate).

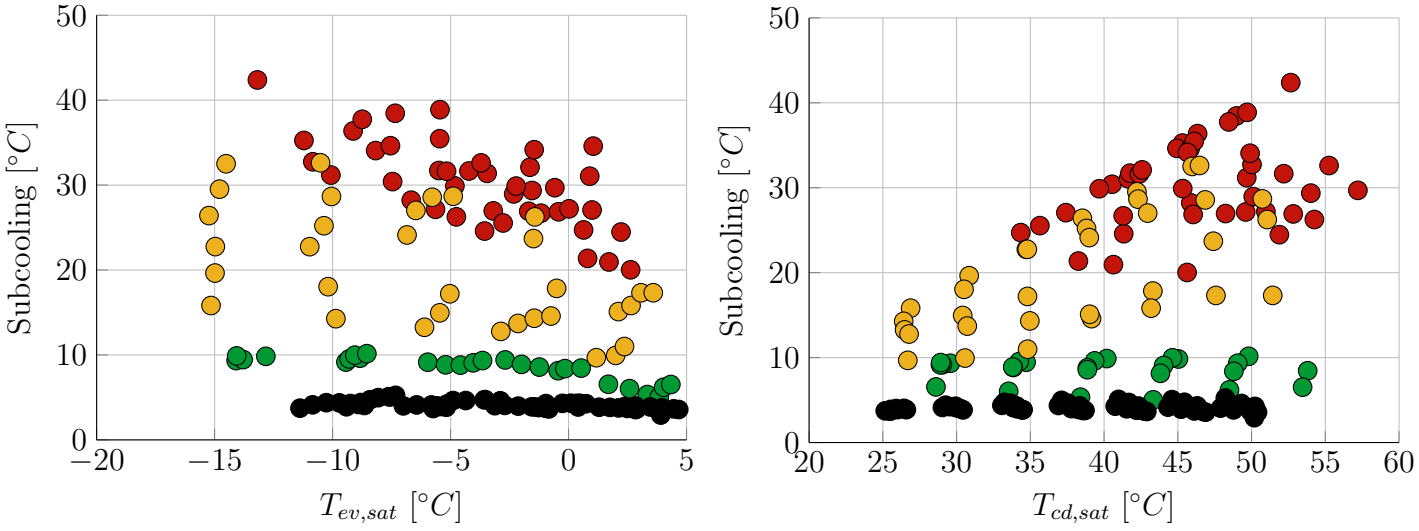

(a) (b)

Figure 3.23: Evolution of the subcooling with the evaporating temperature (a), and with the condensing temperature (b) (red: overcharged system; green: well charged system with $1.1kg/s$ condenser water flow rate; orange: well charged system with small condenser water flow rate; black: liquid receiver added in the system with small condenser water flow rate).

3.10 Effect of high water temperature lift

As previously introduced, a high water temperature lift is reached at small water flow rate. This allows, at a constant water outlet temperature, to decrease the inlet water temperature. In this test bench, it is done by supplying the condenser directly with tap water, without preheating (i.e. without recirculation of the exit water). The supplied water temperature varies between 8.5 and 12.5°C and has a mean value of 10.3°C. The water flow rate is therefore adjusted to reach the desired outlet secondary fluid temperature. The comparison between a 10K lift (i.e. nominal case) and high water temperature lift is made through TS diagrams, shown in Figures 3.24a and 3.24b. Few observations can be made: the condenser and evaporator heat loads increase with lift, while the condensing pressure decreases. Those observations are detailed below.

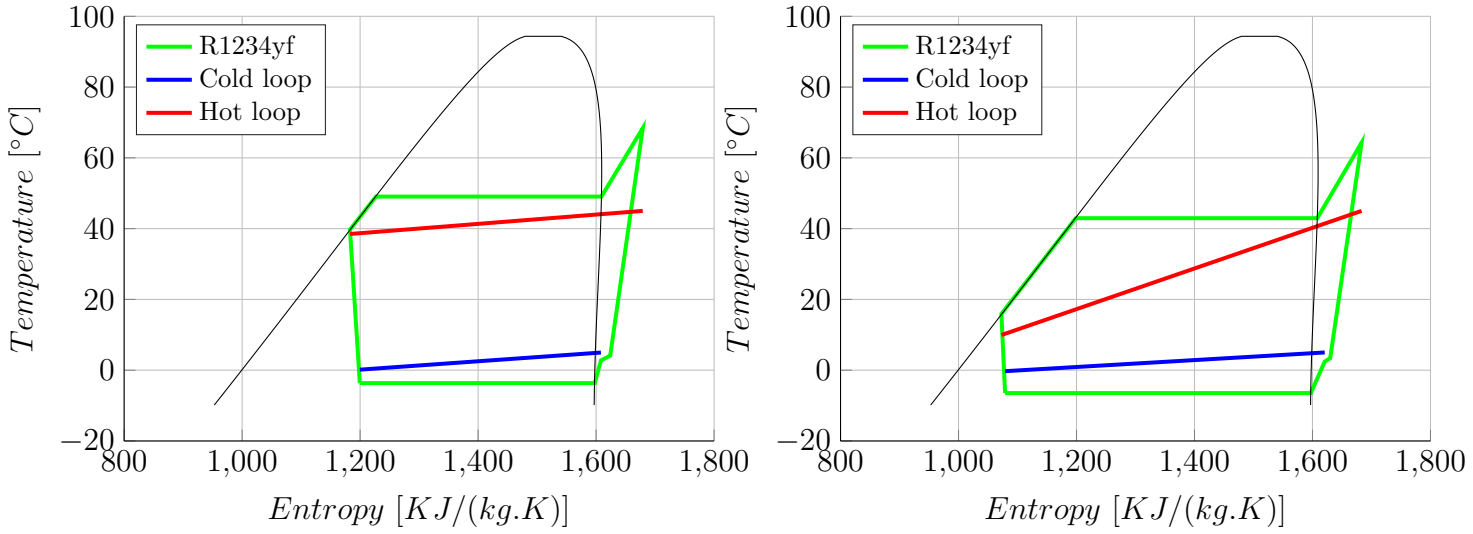

(a) (b)

Figure 3.24: TS diagram in nominal conditions (i.e. preheated tap water entering the condenser) (a), and TS diagram with tap water entering the condenser without being preheated (b).

As previously seen on the TS diagram, $\dot{Q}_{cd}$ is higher at small water flow rates, except for some testing points at $T_{ev,sf,su}$=15°C. The heat pump is therefore providing more thermal heat at small $\dot{m}_{sf,cd}$. One can remark, in Figure 3.25a, that the condenser heat load is not influenced by the water flow rate when the temperature water lift is high. The heat transfer between the cold and hot fluid in the evaporator also increases with decreasing water lift, as shown in Figure 3.25b. The increases in $\dot{Q}_{cd}$ and $\dot{Q}_{ev}$ benefits the heat pump performances if the needed compressor power does not increase.

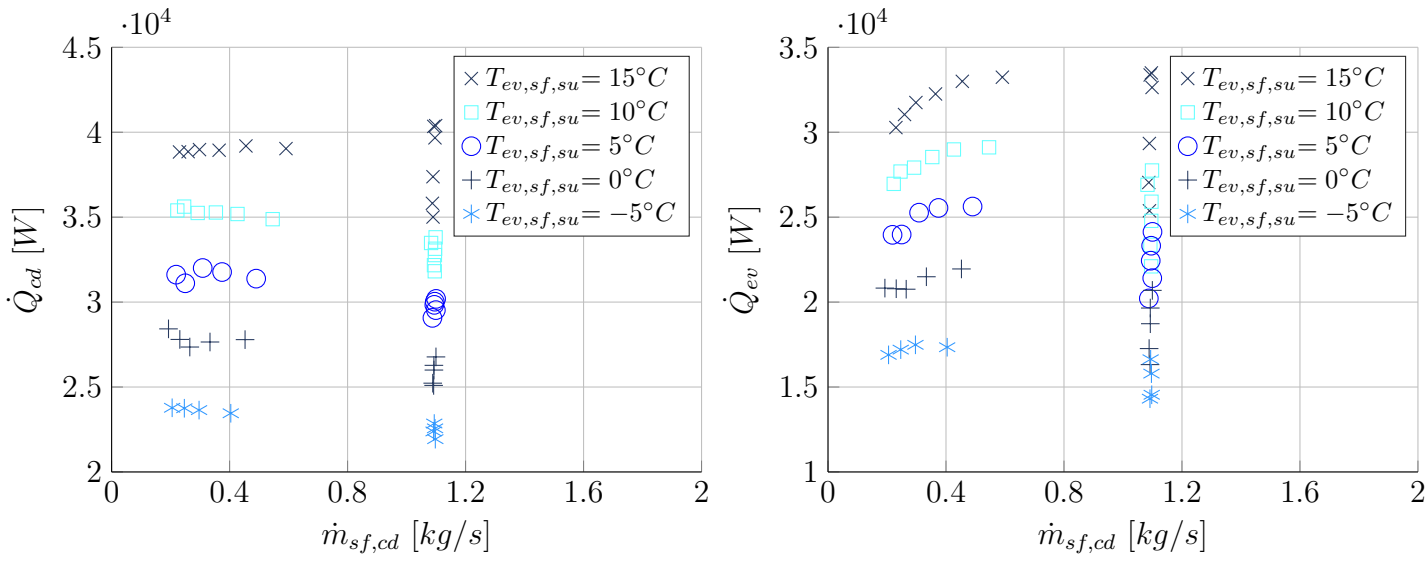

(a) (b)

Figure 3.25: Evolution of the condenser heat load (a), and of the evaporator heat load (b) with the condenser water mass flow rate

Another important observation on the TS diagram was the decrease in the condensing saturation temperature. One can see in Figure 3.26a that this decrease is even more significant at high $T_{cd,sf,ex}$, it can reach up to a $5K$ difference. The condensing pressure, proportional to the condensing temperature, also decreases and the compression work supplied by the scroll compressor drops at high water temperature lift, as shown in Figure 3.26b.

The beneficial effects of a high water temperature lift on both the produced thermal power and consumed electrical power have a positive impact on the coefficient of performance. Figure 3.26c shows the COP as a function of $T_{cd,sf,ex}$ with different values of $T_{ev,sf,su}$. The COP for a heat pump supplied by a small $\dot{m}_{sf,cd}$ is always higher than the one supplied with a water flow rate equal to $1.1kg/s$. This difference is particularly striking at low $T_{ev,sf,su}$ and high $T_{cd,sf,ex}$. To conclude, the more extreme the conditions, the higher achieved benefits with a small condenser flow rate.

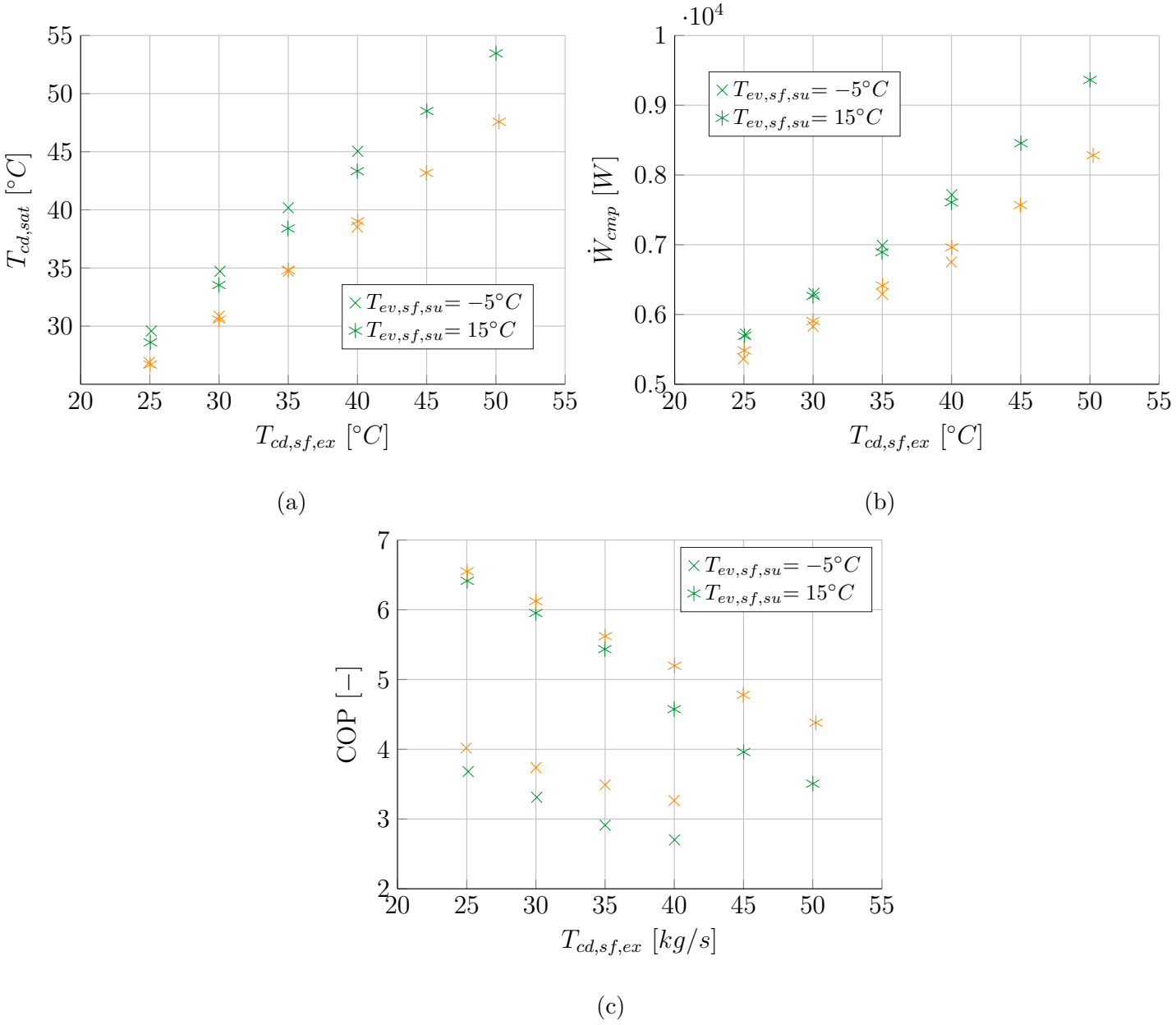

Figure 3.26: Evolution of the condensing temperature (a), of the compressor work (b), and of the COP with $T_{cd,sf,ex}$ (green: well charged system with $1.1kg/s$ condenser water flow rate; orange: well charged system with small condenser water flow rate).

3.11 Effect of superheat

During the experimental campaign, the controller of the electronic expansion valve is configured to reach a superheat of $5°C$. In order to confirm this choice, the effect of three values of superheat is studied in the following section, i.e. $5°C$, $15°C$ and $20°C$.

One can see in Figure 3.27a that high values of superheat tend to decrease the thermal power at the evaporator. At first sight, this statement is counter-intuitive as a

higher superheat should imply a higher heat load in vapour state, in addition to the one in two-phase state. As observed in Figures 3.27b and 3.27c, the evaporator exit temperature of the refrigerant is yet increasing with superheat, but the evaporating temperature is decreasing. As stated before, a lower $T_{ev,sat}$ is correlated with lower evaporator heat load.

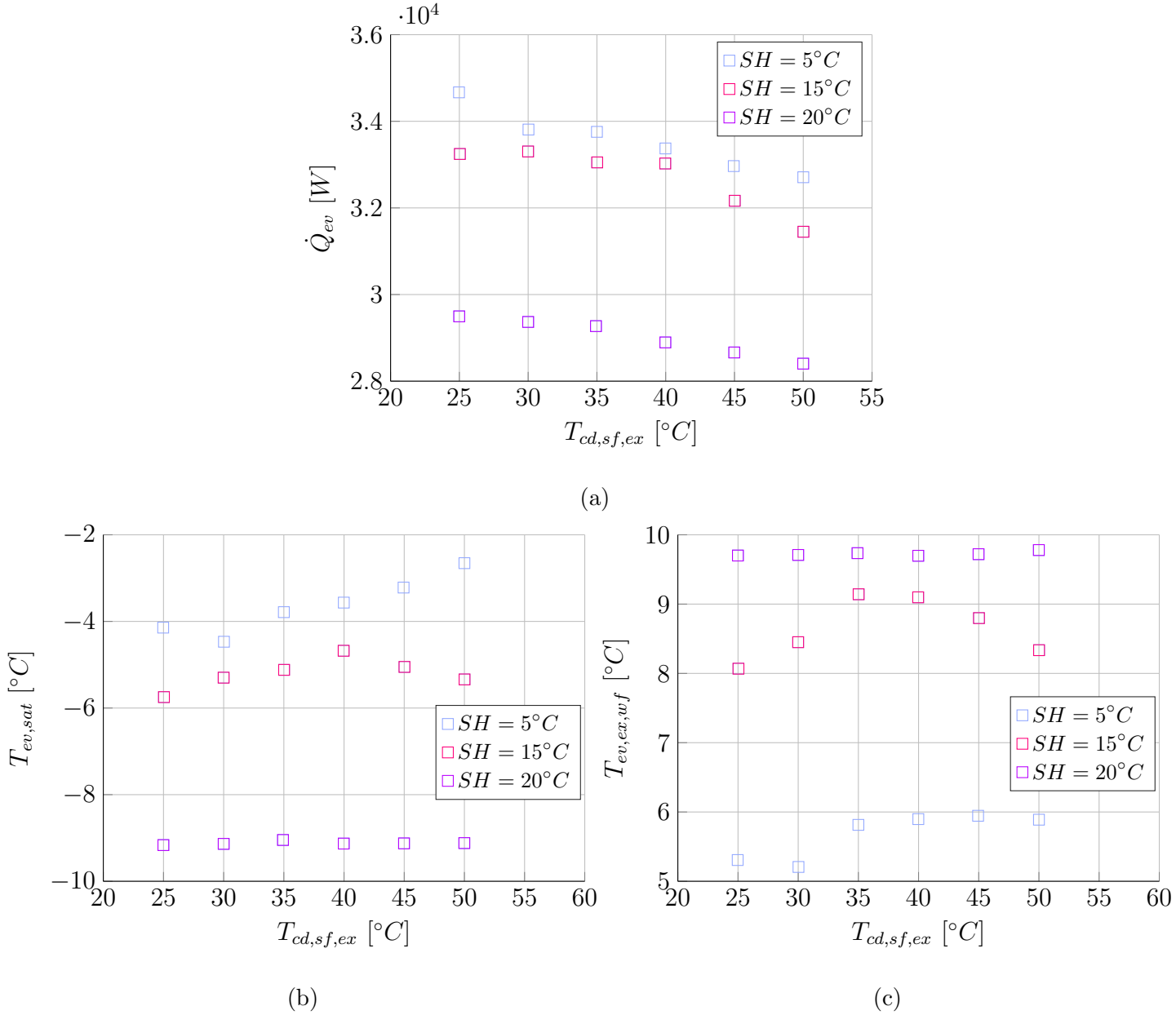

Figure 3.27: Variation of the evaporator heat load (a), of the evaporating temperature (b), and of the working fluid evaporator exhaust temperature (c) with different values of superheat.

As shown in Figure 3.28a, the compressor work is almost independent of the superheat value, even though the supply temperature of the compressor changes. As the

heat pump consumes the same amount of electrical power but extracts less heat at higher superheat, the produced thermal power at the condenser is lower. As a result, the coefficient of performance of the heat pump decreases with the superheat, as seen in Figure 3.28b. A five degrees superheat at the evaporator outlet is therefore an appropriate set point for the expansion valve controller. A lower value could damage the compressor as it could result in liquid refrigerant droplet at its inlet.

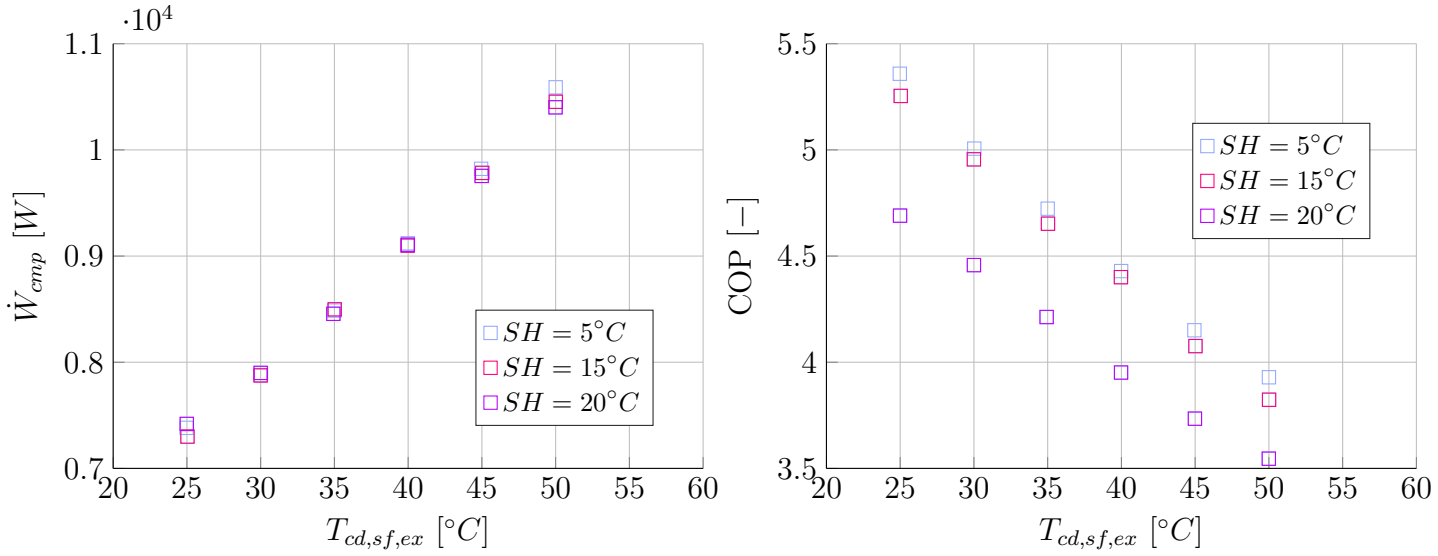

(a) (b)

Figure 3.28: Variation of the compressor work (a), and of the heat pump coefficient of performance (b) with different values of superheat.

Figure 3.29 describes the variation of the subcooling with different values of superheat , it shows that the subcooling at the condenser outlet increases with superheat. This can be explained by a higher area used by vapour in the evaporator, at the expense of the two-phase refrigerant. Less refrigerant is needed in the evaporator as working fluid in vapour phase has a lowest density than in two-phase. The excess of refrigerant therefore migrates to the condenser which increases the subcooling.
Due to the many pressure losses in the liquid line, this specific heat pump is highly sensitive to subcooling: it should, at anytime, be sufficient to ensure liquid is supplying the expansion valve. If vapour bubbles appear in the sight glass, a solution could be to increase the superheat setpoint of the controller, in cases where refrigerant can not be added to the system.

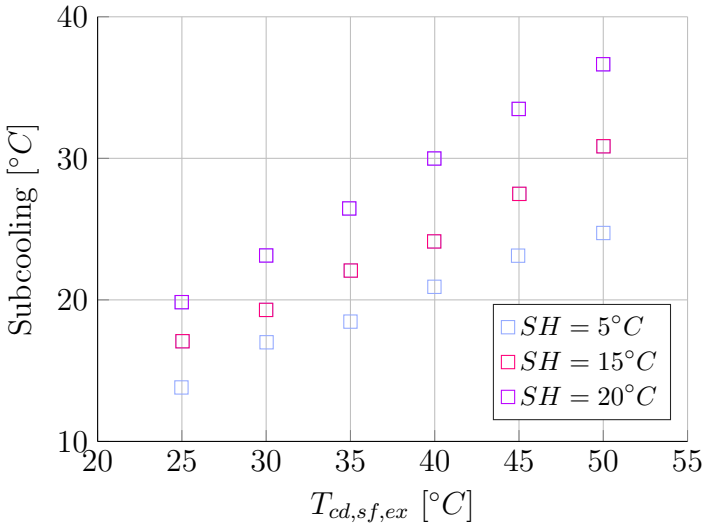

Figure 3.29: Variation of the subcooling with different values of superheat.

3.12 Impact of a liquid receiver

Analysing the impacts of a liquid receiver is of major importance to design a heat pump. Adding a liquid receiver has many advantages as it can meet fluctuations in the system by acting as a cushion. One can see in Figure 3.30 that $T_{cd,sf,ex}$ oscillates around the desired temperature (i.e. $50°C$) with a significant amplitude when the system does not include a liquid receiver. As shown in Figure 3.31, the heat pump is much more stable when a liquid receiver is added after the condenser, only some small oscillations are observed. Figure 3.32 shows the difference between the maximal and minimal temperature of $T_{cd,sf,ex}$ observed during each test. Without a buffer, this difference increases with $T_{cd,sf,ex}$ and reaches a maximum value of $7.17°C$. Those temperature variations are passed on pressure, mass flow and therefore compressor work. It might cause damage to the heat pump components. With a receiver, the temperature oscillation has a maximum amplitude of $2.4°C$, with a mean value of $1.2°C$.

The previous results have shown the importance of adding a liquid receiver to a heat pump. However, it also adds complexity to the system. The liquid receiver needs an extra amount of refrigerant (i.e. 3.87 kg) which adds up non-negligible extra cost. It is worth noting that the liquid receiver was oversized, less refrigerant should be added in a well-sized receiver. Besides, receiver leads to zero subcooling if it is partially filled [46] and, in many applications, a subcooler is required to ensure liquid fluid in the expansion valve. It was not possible to add one and the heat pump has been tested with a liquid receiver but without a subcooler. However, large fluctuations were observed, as it is detailed below. It has been decided to try to subcool the refrigerant inside the liquid receiver, by immersing it inside a bucket where freshwater was added.

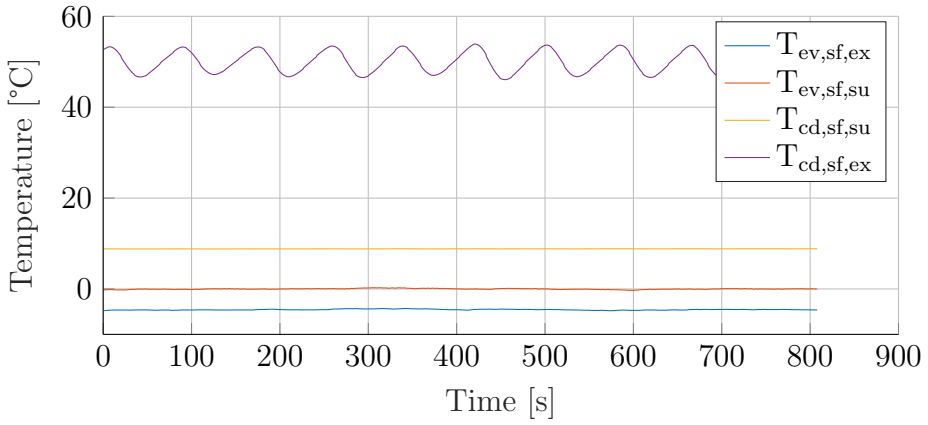

Figure 3.30: Temperatures evolution without liquid receiver.

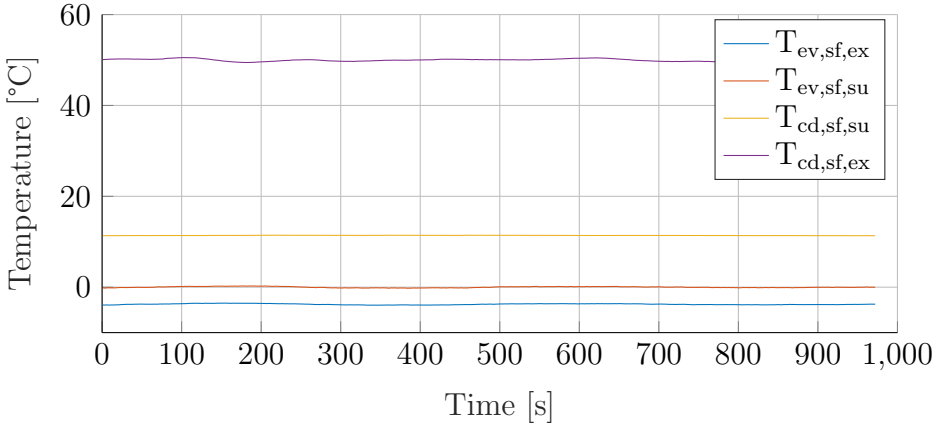

Figure 3.31: Temperatures evolution with liquid receiver.

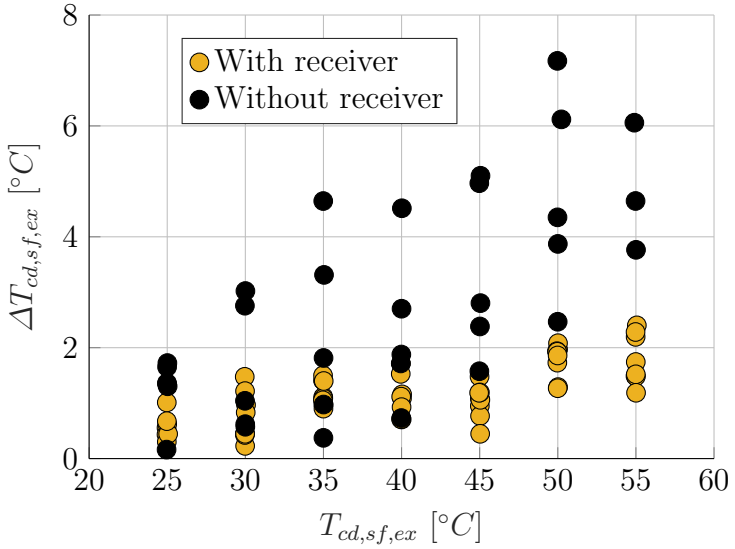

Figure 3.32: Variation of the difference between the maximal and minimal temperature $T_{cd,sf,ex}$.

The evolution of the subcooling at the condenser outlet and at the receiver outlet is displayed in Figure 3.33. Testing is performed from 0 to 500s without adding fresh water to the bucket, i.e. the liquid receiver is only surrounded by air. One can observe large fluctuations of the subcooling at the receiver outlet, with a value between 0.8 and 11.4°C. Refrigerant is always leaving the receiver in liquid saturated state but loses some subcooling in the liquid line due to pressure losses. The expansion valve is therefore periodically provided with a two phases fluid. As it can be seen in Figure 3.34, the EEV opening degree fluctuates between 40 and 100% when the receiver is not cooled down. After 500s, tap water is supplied to the bucket, around the liquid receiver. The system then reaches a stabilized state, as it can be observed in Figures 3.33 and 3.34. This heat pump can therefore not work properly with a liquid receiver if the refrigerant is not subcooled inside the receiver or with a subcooler. It should be noted that the liquid receiver has been oversized (i.e. 20l instead of 6-8l) due to high delays time for smaller receiver purchase order. The oversized receiver might be a reason for the loss of subcooling. Indeed, a receiver is filled with both vapour and liquid refrigerant. At the liquid-vapour interface, the refrigerant is saturated. Below this interface, the refrigerant is subcooled. The refrigerant leaves the receiver toward the bottom through an immersion tube and the working fluid can be subcooled at the outlet. As the receiver is oversized, vapour fluid is filling up most of the volume and the refrigerant looses almost all of its subcooling.

Figure 3.35 shows the variation of the coefficient of performance when a liquid receiver is added in the heat pump. The COP decreases with a receiver, especially at high values of $T_{cd,sf,ex}$ and low values of $T_{ev,sf,su}$. This can be explain by the loss of subcooling when a receiver is added, as it can be seen in Figure 3.36. As subcooling decreases, the condensing thermal power is reduced and, because the electrical consumption remains constant (i.e. constant condensing and evaporating pressures are shown on the graphs), the COP decreases. It is worth noting that heat losses occur in the receiver because of the freshwater added to the bucket to subcool the refrigerant. These losses are also responsible of the COP reduction.

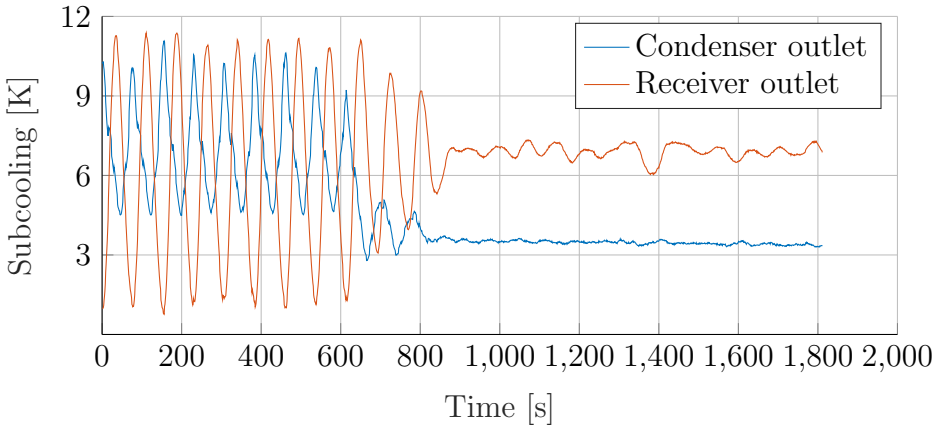

Figure 3.33: Evolution of the subcooling when the refrigerant is subcooled inside the liquid receiver.

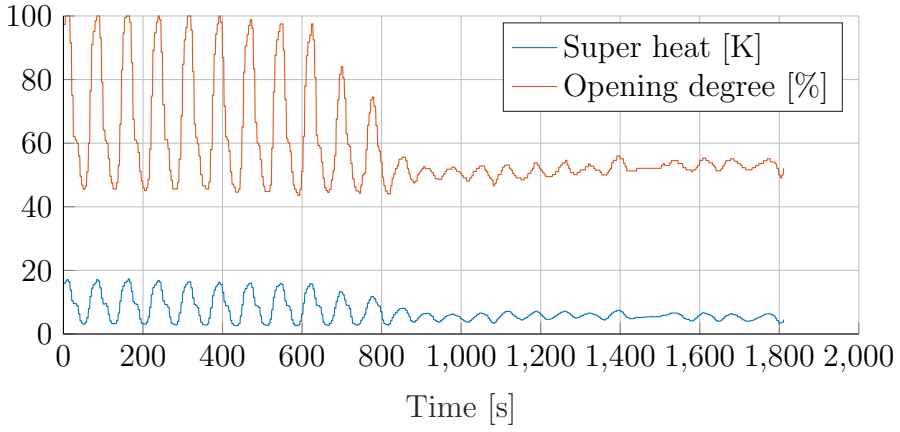

Figure 3.34: Evolution of the superheat and the opening degree of the EEV when the refrigerant is subcooled inside the liquid receiver.

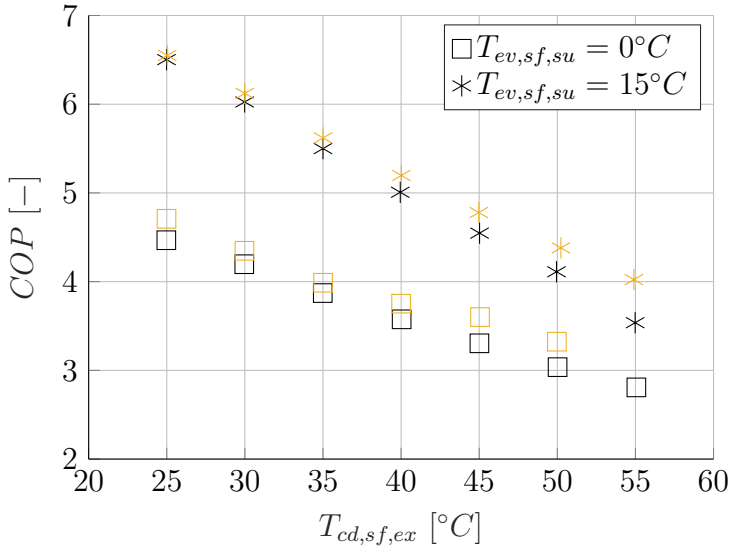

Figure 3.35: Variation of the coefficient of performance without a liquid receiver (orange) and with a liquid receiver (black).

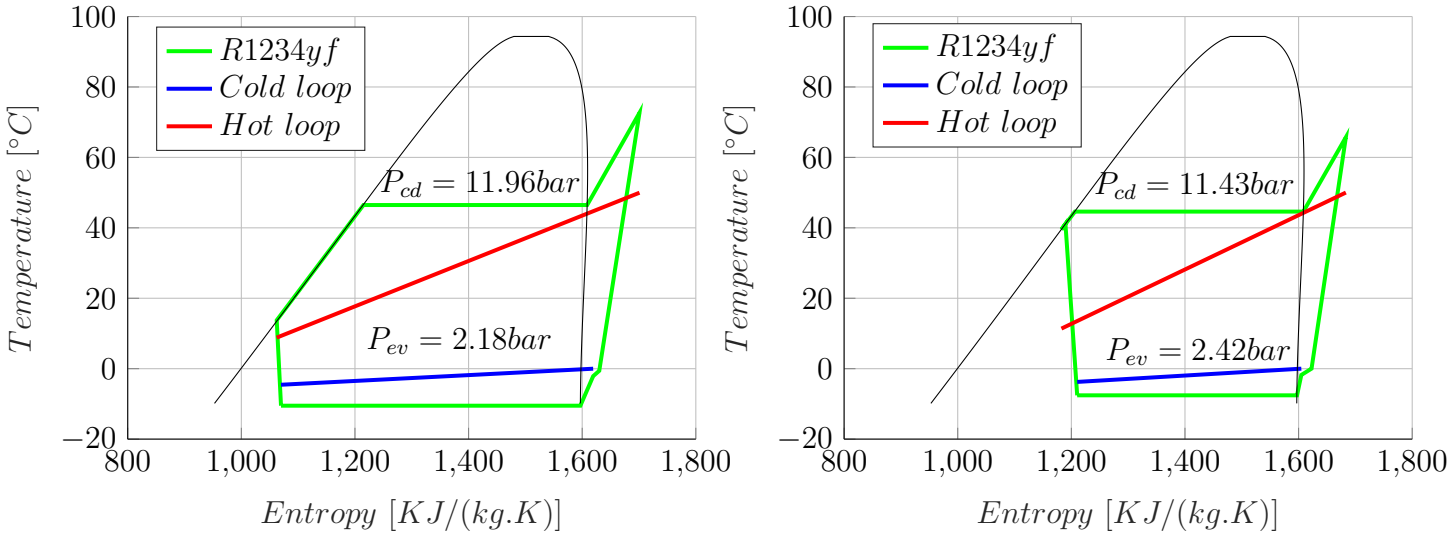

(a) (b)

Figure 3.36: TS diagram without a liquid receiver (a), and TS diagram with a liquid receiver (b).

Chapter 4

Semi empirical model of the heat pump

The performances of this $50kW_{th}$ heat pump are predicted with a semi-empirical model. The individual components are first modelled and then the complete model of the heat pump is detailed. A validation of the model followed by an analysis of the compressor through its model are presented.

4.1 Literature review

Heat pump models can be categorised into three mains groups: deterministic (white-box), semi-empirical (grey-box) and empirical (black-box) models.

Deterministic models allow predicting the performances of heat pumps by describing the physics of the processes within the vapour compression cycle. They provide high accuracy and have been widely used in the 1970s (Hiller and Glicksman in 1976 [47], Ellison et al. in 1976 [48]). However, the accuracy is obtained at the expense of complexity and computational time.

Empirical models are based on correlations derived, by curve fitting or regression analysis, from experimental data. The physical heat transfer and compression mechanisms are not considered. Black-box models are simplistic solutions that offer very fast calibration and execution speeds [49] [50]. However, the accuracy of the prediction drops in extrapolated conditions [51].

Semi-empirical models are a combination of empirical and deterministic models. The heat pump performances are predicted through physical equations and empirical parameters, only by describing the most impacting physical processes of the vapour compression cycle. It allows getting fast computational time while having good accuracy and extrapolation capabilities.

4.2 Components modelling

4.2.1 Compressor

The scroll compressor model is based on the ones developed by Winandy et al [52], Ransy et al [53] and Dickes et al [46] which describe the compression through thermodynamic transformations. The compression process is decomposed into six main stages, as shown in Figure 4.1:

1) Isobaric heating-up ($su \rightarrow su_1$),
2) Isobaric mixing between supply and leakage flows ($su_1 \rightarrow su_2$),
3) Isentropic compression ($su_2 \rightarrow ad$),
4) Isochoric compression ($ad \rightarrow ex_2$),
5) Isenthalpic pressure drop ($ex_2 \rightarrow ex_1$),
6) Isobaric cooling down ($ex_1 \rightarrow ex$)

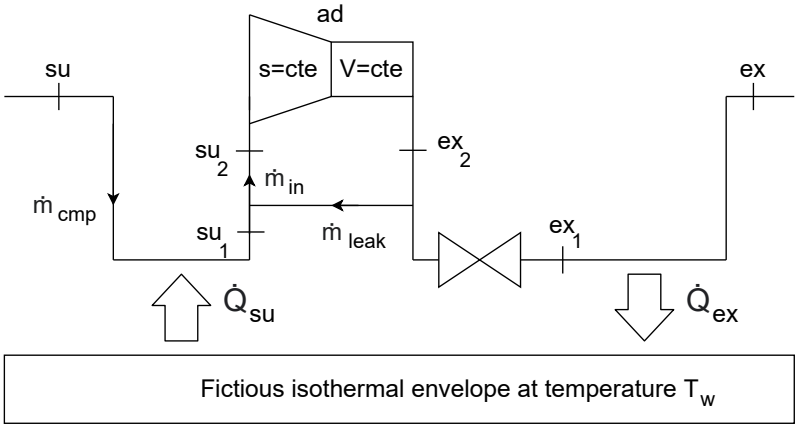

Figure 4.1: Conceptual schema of the compressor model.

- **Isobaric supply heat transfer**:
  The compressor is subjected to various heat transfer processes such as the ones between the refrigerant and the compressor shell, between the shell and the ambient air and the one provided by electromechanical losses. A fictitious isothermal envelope at temperature T_w is introduced to represent the compressor metal mass.

  The isobaric heat transfer undergone by the refrigerant at the entrance of the compressor is described by the $\epsilon - NTU$ method, with the following equations:

$$\dot{Q}_{su} = \dot{m}_{cmp} \left(h_{su1} - h_{su} \right) = \epsilon_{su} \dot{m}_{cmp} c_{p,su} \left(T_w - T_{su} \right), \tag{4.1}$$

$$\epsilon_{su} = \left(1 - e^{\left(\frac{-AU_{su}}{\dot{m}_{cmp} c_{p,su}}\right)}\right), \tag{4.2}$$

$$AU_{su} = AU_{su,n} \left(\frac{\dot{m}_{cmp}}{\dot{m}_{cmp,n}}\right)^{0.8}, \tag{4.3}$$

$$\dot{m}_{cmp,n} = V_s \cdot \rho_n(T_{ref}) \cdot \frac{N_{ref}}{60}. \tag{4.4}$$

Four parameters are introduced: the nominal supply heat transfer coefficient AU_{su}, the swept volume of the scroll compressor V_s and the nominal temperature (T_{ref}) and rotational speed (N_{ref}).

- **Isobaric mixing between supply and leakage flows:**
  Scroll compressors are subjected to two kinds of leakage flows: one through the axial clearance and one through the radial clearance [54]. The axial leakage occurs between the flanks of the fixed and orbiting scrolls while the radial leakage occurs between the plates and the scrolls, as shown in Figure 4.2. The two leakage flows are modelled as one fictitious leakage through a convergent nozzle of cross-sectional area A_{leak}, as shown in Figure 4.1.

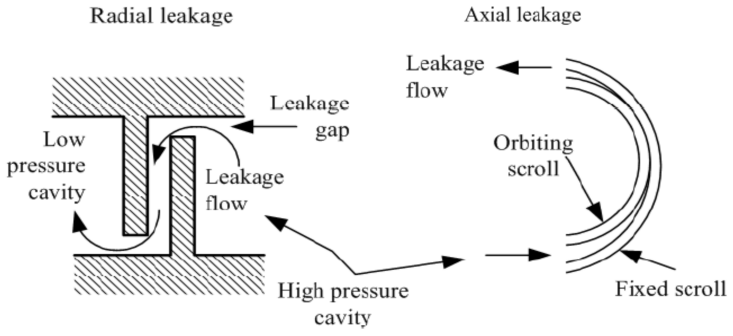

Figure 4.2: Axial and radial leakages [1].

The leakage flow is defined by combining the mass and energy conservation equations through the nozzle:

$$\dot{m}_{\text{leak}} = A_{\text{leak}}\, \rho\left(s_{\text{ex }2}, P_{thr}\right) \sqrt{2\left[h_{\text{ex }2} - h\left(s_{\text{ex }2}, P_{\text{thr,leak}}\right)\right]}, \tag{4.5}$$

where the throat pressure P_{thr}, defined by Eq. 4.6, corresponds to the maximum of the supply pressure P_{su1} and the critical pressure which is computed by considering the working fluid vapour as a perfect gas.

$$P_{thr,leak} = \max\left(P_{su1}, P_{crit}\right) = \max\left(P_{su1}, P_{ex2}\left(\frac{2}{\gamma_{ex2}+1}\right)^{\frac{\gamma_{ex2}}{\gamma_{ex2}-1}}\right) \tag{4.6}$$

The internal mass flow rate $\dot{m}_{in}$ is proportional to the density of R1234yf after the isobaric mixing ρ_{su2}, to the swept volume of the scroll compressor V_s and to the rotational speed of the compressor N, as shown in Eq. 4.7:

$$\dot{m}_{in} = \rho_{su2} V_s \frac{N}{60}. \tag{4.7}$$

The condition of the fluid before the isentropic compression can be obtained by considering an isobaric mixing between the supply and leakage flow, described with the two following equations:

$$\begin{aligned} \dot{m}_{in} &= \dot{m}_{cmp} + \dot{m}_{leak} \\ \dot{m}_{in} h_{su2} &= \dot{m}_{cmp} h_{su1} + \dot{m}_{leak} h_{ex2} \end{aligned} \tag{4.8}$$

One parameter is introduced and needs to be determined: A_{leak}.

- **Isentropic and isochoric compression:**
  The compression subjected to the refrigerant, inside a scroll compressor, is modelled first with an isentropic compression up to an adapted pressure P_{ad} and then with an isochoric compression.

  The adapted pressure is estimated via the adapted entropy ($s_{ad} = s_{su2}$) and the adapted specific volume υ_{ad}, defined by Equation 4.9.

$$\upsilon_{ad} = \frac{\upsilon_{su2}}{r_{v,in}}, \tag{4.9}$$

  where $r_{v,in}$ is the built-in volume ratio of the machine, a parameter which needs to be determined.

  If the adapted pressure P_{ad} is different than P_{ex2}, the compressor is not adapted to the given pressure ratio and the fluid is then compressed or expanded at constant volume to reach the appropriate exhaust pressure.

  The isochoric compression work undergone by the fluid is described by:

$$W_v = \upsilon_{ad} \cdot (P_{ex2} - P_{ad}) \tag{4.10}$$

  The total compression work $\dot{W}_{in}$ is the sum of the isentropic compression work $\dot{W}_s$ and the isochoric compression work $\dot{W}_v$.

- **Isenthalpic pressure drop:**
  The internal discharge pressure P_{ex2} introduced for the isentropic compression is determined by knowing the exhaust pressure P_{ex} and the isenthalpic pressure drop at the outlet of the compressor. The pressure drop is computed by considering an isentropic flow through a simply convergent nozzle, as done for the leakage flow. Then, we have:

$$\dot{m}_{cp} = A_{dis}\rho\left(s_{ex2}, P_{thr,dis}\right)\sqrt{2\left[h_{ex2} - h\left(s_{ex2}, P_{thr,dis}\right)\right]}, \tag{4.11}$$

$$P_{thr,dis} = \max\left(P_{ex}, P_{ex2}\left(\frac{2}{\gamma_{ex2}+1}\right)^{\frac{\gamma_{ex2}}{\gamma_{ex2}-1}}\right), \tag{4.12}$$

  where A_{dis}, the fictious discharge throat area, is a parameter to identify.

- **Isobaric exhaust heat transfer:**
  The fictious discharge heat transfer is modelled as the suction heat transfer. The same equations than for the supply heat transfer therefore apply:

$$\dot{Q}_{ex} = \varepsilon_{ex}\dot{m}_{cmp}c_{p,ex1}\left(T_w - T_{ex1}\right) \tag{4.13}$$

$$\varepsilon_{ex} = \left(1 - e^{\left(\frac{-AU_{ex}}{\dot{m}_{cmp}c_{p,ex1}}\right)}\right) \tag{4.14}$$

$$AU_{ex} = AU_{ex,n}\left(\frac{\dot{m}_{cmp}}{\dot{m}_{cmp,n}}\right)^{0.8} \tag{4.15}$$

- **Heat balance over the compressor**
  As steady-state conditions are assumed, a global energy balance can be stated:

$$\dot{W}_{loss} - \dot{Q}_{ex} - \dot{Q}_{su} - \dot{Q}_{amb} = 0, \tag{4.16}$$

  where $\dot{W}_{loss}$ and $\dot{Q}_{amb}$ are the mechanical losses and the ambiant losses respectively.

  Ambient losses are computed by Equation 4.17. A new parameter is introduced and needs to be identified: AU_{amb}, the global heat transfer coefficient between the compressor and the environment.

$$\dot{Q}_{amb} = AU_{amb}\cdot\left(T_w - T_{amb}\right), \tag{4.17}$$

Mechanical losses are modelled via two terms:

$$\dot{W}_{loss} = \dot{W}_{loss,0} \cdot \left(\frac{N}{N_{ref}}\right)^2 + \alpha \cdot \dot{W}_{in}. \tag{4.18}$$

The constant electro-mechanical loss term $\dot{W}_{loss,0}$ and the factor of proportionality α are positive parameters to be identified.

Eleven parameters have been introduced by the compressor model. One is given by the manufacturer (V_s=347.8cm^3), two are fixed arbitrarily (T_{ref}=5°C, N_{ref}=3000rpm) and the other parameters need to be determined from the experimental data. A multivariate optimization is performed with the *MATLAB* fmincon function so as to minimise a global error residual E:

$$E = \sqrt{\frac{1}{n} \cdot \sum_{i=1}^{n} \left(\left(\frac{\dot{W}_{pred,i} - \dot{W}_{meas,i}}{\dot{W}_{pred,i}}\right)^2 + \left(\frac{\dot{M}_{pred,i} - \dot{M}_{meas,i}}{\dot{M}_{pred,i}}\right)^2 + \left(\frac{h_{ex,pred,i} - h_{ex,meas,i}}{h_{\text{cex },pred,i}}\right)^2 \right)} \tag{4.19}$$

The values of the parameters obtained after calibration are given in Table 4.1.

Supply heat transfer coefficient	AU_{su}	$63.9W/K$
Leakage area	A_{leak}	$2.05mm^2$
Built-in volume ratio	$r_{v,in}$	3.12
Discharge area	A_{dis}	$404.63mm^2$
Exhaust heat transfer coefficient	AU_{ex}	$514W/K$
Heat transfer coefficient with the ambient	AU_{amb}	$7.51W/K$
Electro-mechanical loss term	$\dot{W}_{loss,0}$	1256 W
Loss factor of proportionality	α	0.22

Table 4.1: Identified parameters of the compressor model

4.2.2 Heat exchangers

The evaporator and condenser are both brazed plate heat exchangers, they are therefore modelled in the same way. The heat exchangers are considered counterflow and their geometric characteristics provided by SWEP are listed in Table 4.2. As it can be seen, the manufacturer only provides few information and assumptions are made. Table 4.3 shows the assumptions that have been made, according to the nomenclature represented in Figure 4.3. The assumptions are made by using the

		Condenser	Evaporator
Plate length	L_p	$0.470m$	$0.470m$
Plate width	L_w	$0.119m$	$0.119m$
Number of plates	N_p	66	84

Table 4.2: Geometric characteristics of the heat exchangers provided by the manufacturer SWEP.

Plate pitch	p	$0.00152m$
Chevron angle	β	$60°$
Enlargement factor	ϕ	1.22
Plate thickness	t	$0.4mm$

Table 4.3: Hypothetical geometric characteristics of brazed plate heat exchangers.

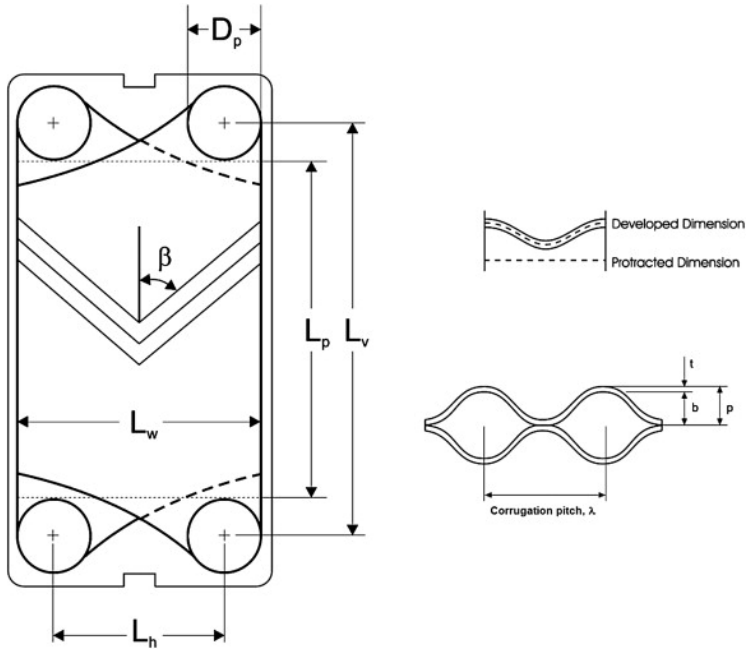

Figure 4.3: Nomenclature of the brazed plate heat exchangers [2]

characteristics of the brazed plate heat exchanger used by Ransy (2020) [53].

The heat exchanger is modelled by means of three zones, depending on the refrigerant state: vapour (v), two-phase (tp) and liquid (l). The total heat transfer in the heat exchanger is the sum of the thermal powers in each zone. The heat transfer rate in each zone are computed as:

$$\left.\begin{aligned} \dot{Q}_{hex,i} &= \dot{m}_{wf}\left(h_{wf,su,i} - h_{ws,cx,i}\right) \\ \dot{Q}_{hex,i} &= \dot{m}_{sf} cp_{sf}\left(T_{sf,ex,i} - T_{sf,su,i}\right) \\ \dot{Q}_{hex,i} &= A_i U_i \Delta T_{\log,i} \end{aligned}\right\} i = v, tp\, or\, l, \tag{4.20}$$

where ΔT_{log} is the logarithmic mean temperature difference between the secondary fluid and the working fluid. A_i and U_i are the heat transfer area and the overall heat transfer coefficient of each zone, respectively.

The overall heat transfer coefficient can be computed with Equation 4.21 by introducing the plate thickness t, the thermal conductive coefficient of the plates k_p and the convective heat transfer coefficient of the secondary fluid $h_{i,sf}$ and of the working fluid $h_{i,wf}$. The conductive heat transfer coefficients are computed with the correlation proposed by Martin [55] for the secondary fluid and in the liquid and vapour zone for the refrigerant, while the correlations proposed by Longo [56] and [57] are used for the refrigerant condensation and evaporation respectively.

$$\left.\begin{aligned} U_i = \frac{1}{\frac{1}{h_{i,sf}} + d\frac{t}{k_p} + \frac{1}{h_{i,wf}}} \end{aligned}\right\} i = v, tp\,or\,l, \tag{4.21}$$

To close the system of equations, the sum of the heat transfer areas of each zone is equal to the total heat transfer area of the condenser or evaporator, computed with the geometric characteristics of the heat exchanger:

$$A_l + A_{tp} + A_v = (N_p - 2) \cdot L_p \cdot L_w \tag{4.22}$$

4.2.3 Heat pump modelling

The compressor and heat exchangers models are interconnected to build the heat pump model. It is important to note that the expansion in the electronic expansion valve is assumed isenthalpic (i.e. $h_{ex,cd}$=$h_{su,ev}$) and that the four-way valve is considered ideal (i.e. without heat transfer, pressure losses neither leakage flows). Pressure drops and ambient heat losses in the pipings are neglected as well. The heat pump model iterates on the evaporating pressure P_{lp} and the condensing pressure P_{hp} in order to minimize the following residuals :

$$Res_1 = 1 - \frac{P_{ev}}{P_{su,cmp}}, \tag{4.23}$$

$$Res_2 = 1 - \frac{P_{ex,cmp}}{P_{cd}}. \tag{4.24}$$

The architecture of the heat pump model is shown in Figure 4.4

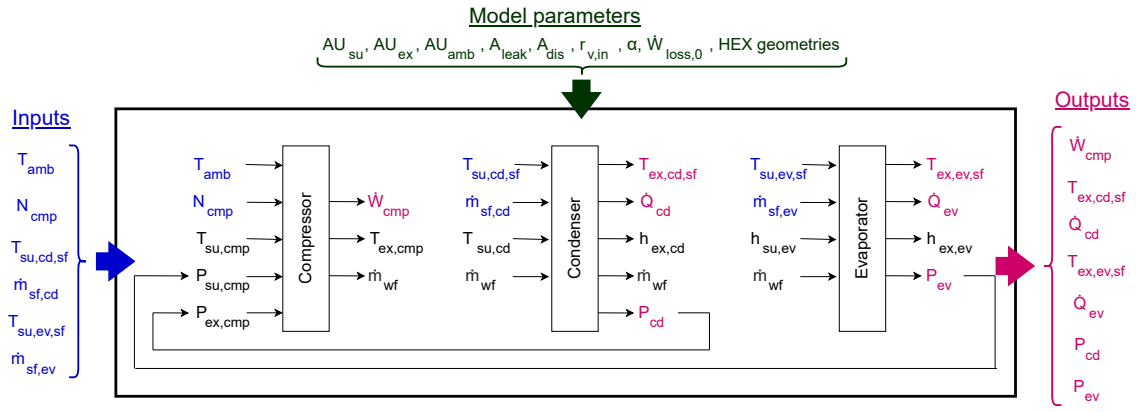

Figure 4.4: Architecture of the heat pump model.

4.3 Model validation

The heat pump model is validated by comparing the predicted values with the measured ones. For this purpose, the sub-models of the condenser, evaporator and compressor are run by providing the testing values as inputs. The achieved results of the sub-models are then compared with the experimental results that were measured during testing.

4.3.1 Condenser sub-model

The condenser receives as inputs the secondary fluid supply temperature and mass flow rate and the working fluid supply temperature and mass flow rate. Figures 4.5a and 4.5b show the comparison between the predicted and measured heat transfer and condensing pressure respectively, when the measured subcooling value is given to the subcooling parameter. The heat transfer rate in the condenser is determined with an accuracy of 2.6% and the condensing pressure with an accuracy of 7.6%. The model is therefore correctly predicting the condenser behaviour.

However, using the measured subcooling value is too much of a hypothesis. The subcooling at the outlet of the condenser is therefore imposed at one fixed value, depending on the working conditions of the heat pump. As discussed in Section 3.9, subcooling remains constant at approximately $5K$ when a liquid tank is used, while it is steady around $10K$ when the system is supplied with a $1.1l/s$ condenser water flow rate. When this mass flow rate is smaller than $1.1l/s$, subcooling varies between 10 and $35K$. Finally, ΔT_{sc} oscillates between 20 and $45K$ when the heat pump is overcharged. The values of the subcooling for the condenser model are functions of those four situations, as shown in Table 4.4.

One can see in Table 4.4, in Figure 4.6a and in Figure 4.6b that the heat rate in

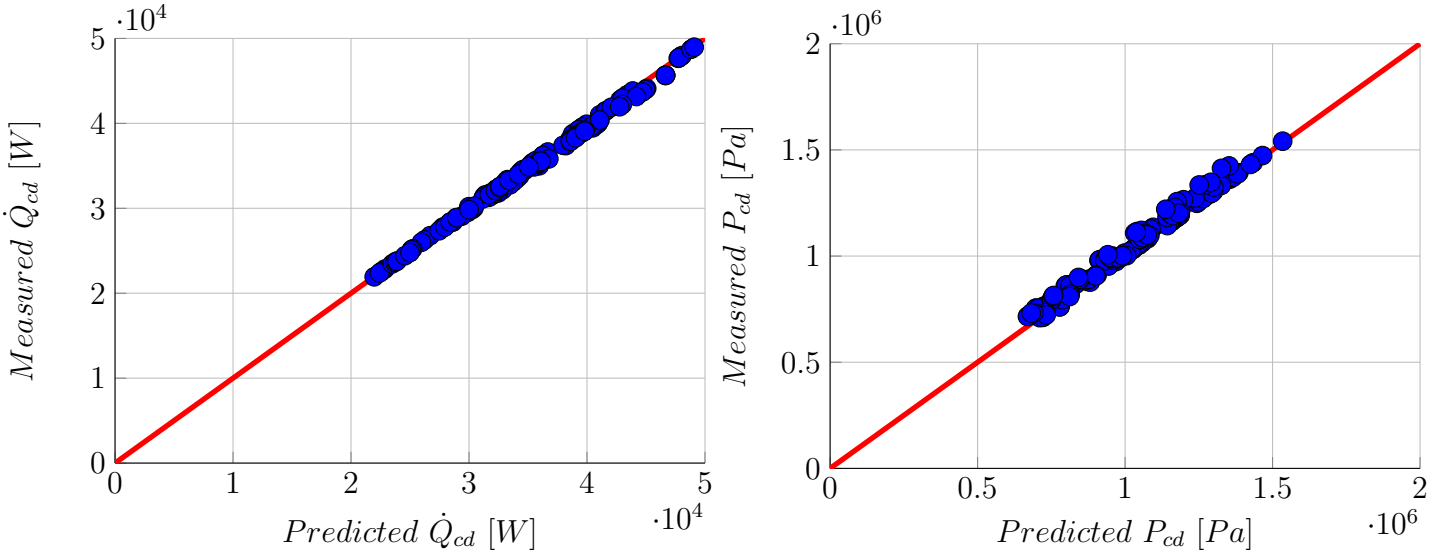

(a) (b)

Figure 4.5: Comparison between predicted and measured heat transfer in the condenser (a), and between predicted and measured condensing pressure (b) when subcooling is assumed well known.

Situation	Subcooling	error($\dot{Q}_{cd}$)	error(P_{cd})
HP with liquid tank	$6K$	12.4%	21.9%
Well charged HP, $\dot{m}_{cd}$=1.1kg/s	$9K$	5%	8.3%
Well charged HP, small $\dot{m}_{cd}$	$15K$	11.9%	19%
Overcharged HP	$30K$	17.1%	26.4 %

Table 4.4: Subcooling and error of $\dot{Q}_{cd}$ and P_{cd} for the condenser sub-model.

the condenser is well estimated. The condensing pressure has higher absolute error (i.e. up to 26.4%), especially when the system is overcharged or provided with a liquid tank. The predictions of the model are highly accurate when the system is well charged and with a 10°C water glide (i.e. in green).

4.3.2 Evaporator sub-model

The evaporator sub-model is predicting the evaporator heat transfer rate with extreme precision, as shown in Figure 4.7a. Indeed, the maximal error on $\dot{Q}_{ev}$ is only 1.8% when the superheat is imposed equal to 5°C. The evaporating pressure is showing less accuracy as it is predicted with a 16% error. Figure 4.7b reveals that P_{ev} is overpredicted in most cases.

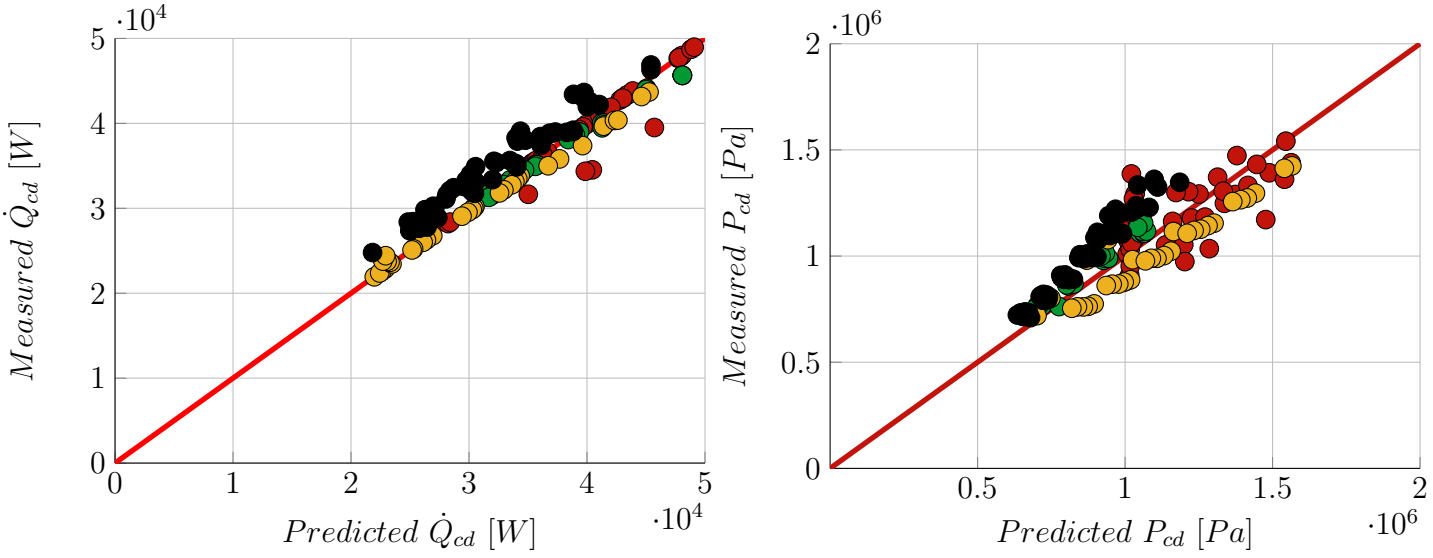

(a) (b)

Figure 4.6: Comparison between predicted and measured heat transfer in the condenser (a), and between predicted and measured condensing pressure (b) (red: overcharged system; green: well charged system with $1.1kg/s$ condenser water flow rate; orange: well charged system with small condenser water flow rate; black: liquid receiver added in the system with small condenser water flow rate).

4.3.3 Compressor sub-model

Figure 4.9a shows the prediction of refrigerant mass flow rate by the compressor sub-model. The working fluid mass flow rate is very well predicted (i.e. with a 6.3% error). The compressor work, shown in Figure 4.8, is even better predicted: the results are accurate within ±5.2 percentage points. It can be seen in Figure 4.9b that the prediction of the compressor exhaust temperature is less accurate, it tends to be slightly underestimated, which means that, for those points, the compressor efficiency is overestimated. $T_{ex,cmp}$ is predicted within an error of $\pm$ 16.7°C. The compressor efficiencies are well predicted, as shown in Figures 4.10a and 4.10b: the maximum errors on isentropic and volumetric efficiencies are 8.5% and 6.3% respectively.

4.3.4 Heat pump model

The heat pump model developed on *MATLAB* allows predicting the performance of the R1234yf heat pump, eventhough the predicted values are subjected to propagation of errors. However, as shown in Table 4.5 and in the following figures,

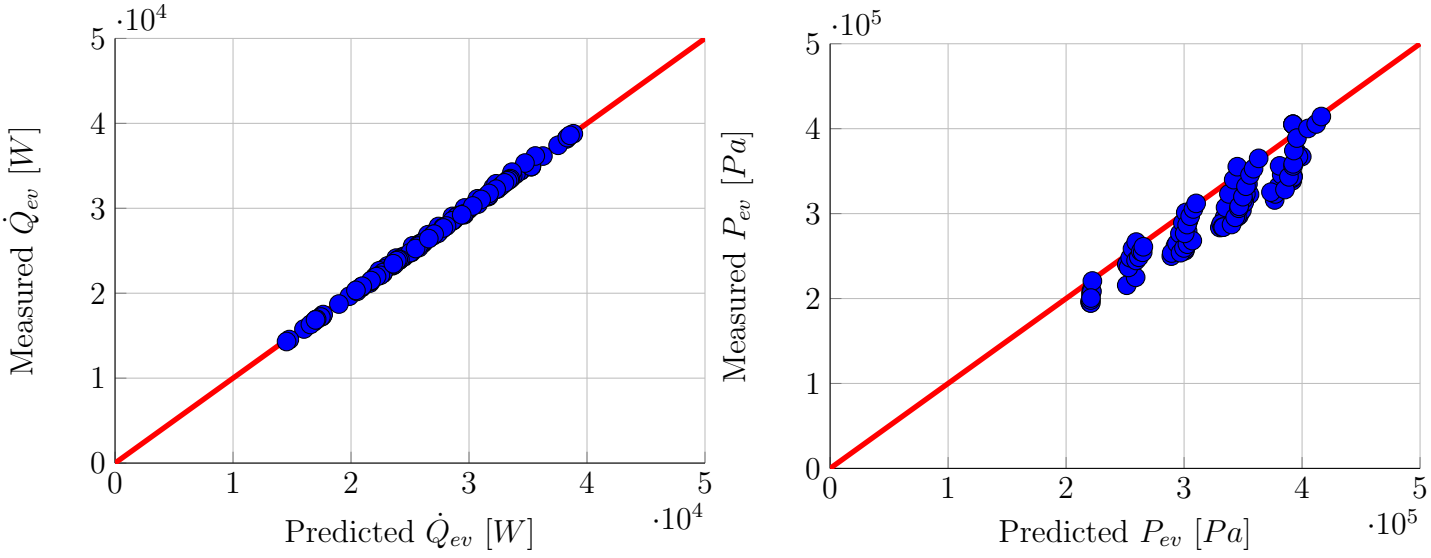

(a) (b)

Figure 4.7: Comparison between predicted and measured heat transfer in the evaporator (a), and between predicted and measured evaporating pressure (b).

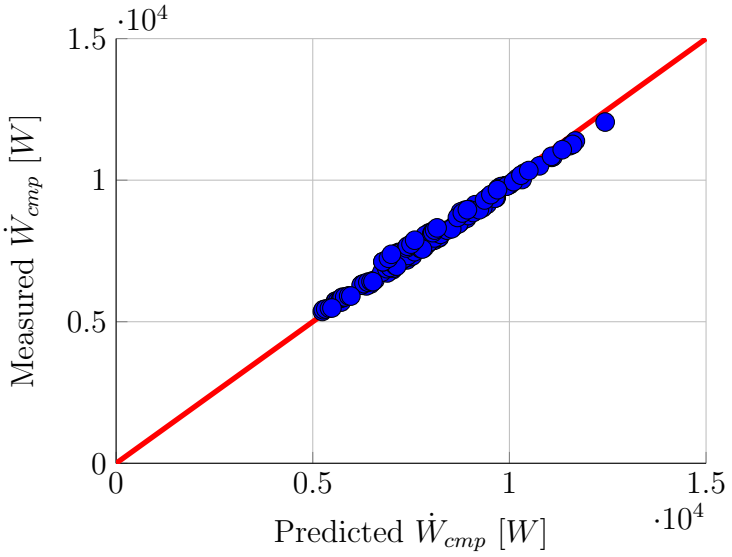

Figure 4.8: Comparison between predicted and measured compressor work.

the accuracy of the predictions is highly dependent on the testing conditions. The model gives the least desirable results when the system is overcharged while the predicted performances show high accuracy when a liquid tank is added to the heat

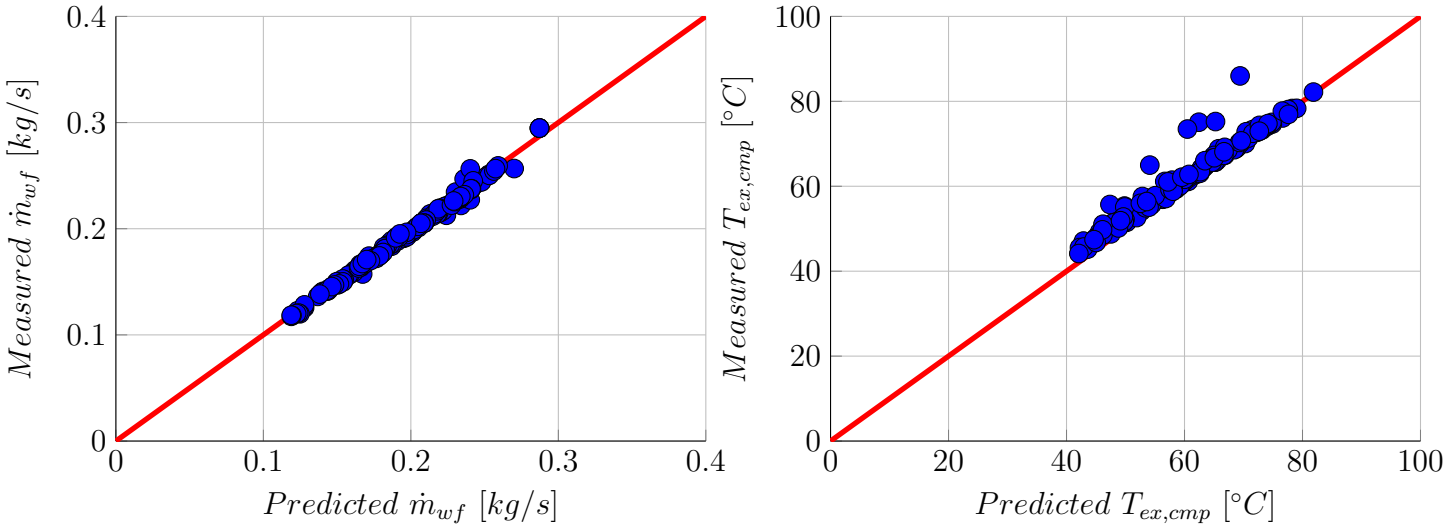

(a) (b)

Figure 4.9: Comparison between predicted and measured refrigerant mass flow rate in the compressor (a), and between predicted and measured compressor exhaust temperature (b).

pump. As shown in Figures 4.11, evaporation and condensation pressure are well predicted, except P_{cd} which shows large scattering predictions when the heat pump is overcharged. According to Figures 4.12, the thermal power in the evaporator and condenser are both predicted with large deviations at high power, the thermal loads being over-predicted. The predictions of the compressor work are highly accurate when the heat pump works in nominal conditions (i.e. well charged HP and condenser mass flow rate of $1.1kg/s$) and when a liquid tank is used, the maximal error being 3.5% and 5.9%, respectively. However, the prediction of $\dot{W}_{cmp}$ are weak for an overcharged system, as depicted in Figure 4.13a. Finally, the predicted coefficients of performances show large deviations to the measured ones, with maximum error of 31%. COP is overestimated, as shown in Figure 4.13b. The results are still considered satisfactory with regard to the various tested conditions.

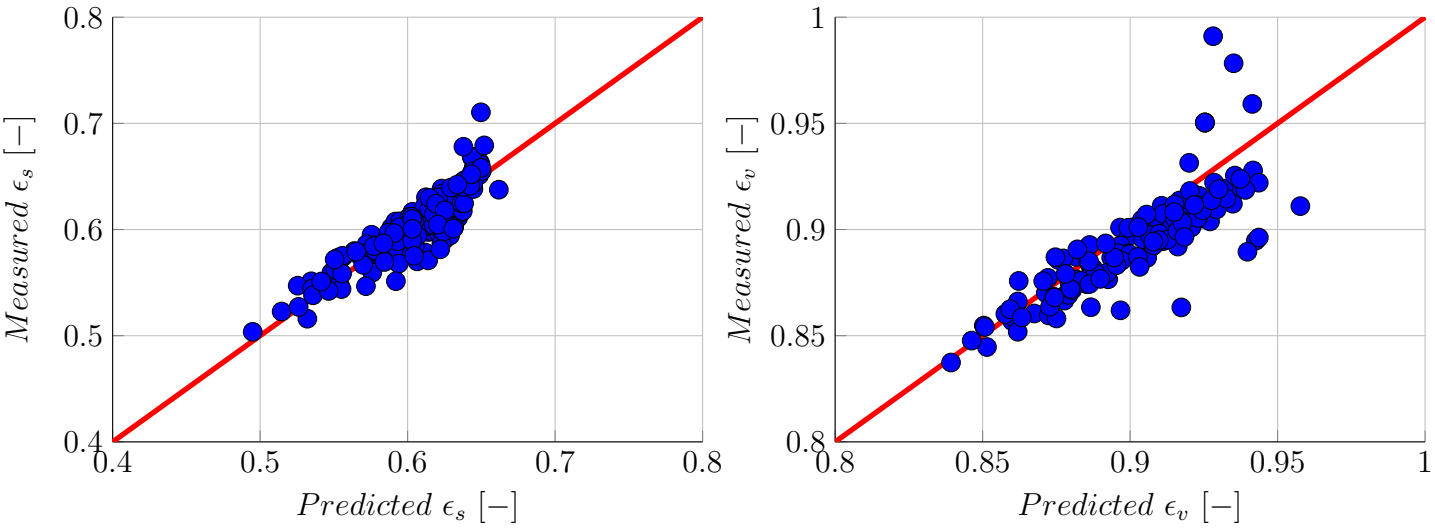

(a) (b)

Figure 4.10: Comparison between predicted and measured compression isentropic efficiency (a), and between predicted and measured compression volumetric efficiency (b).

	Overcharged HP	Well charged HP, $\dot{m}_{cd}$=1.1kg/s	Well charged HP, small $\dot{m}_{cd}$	HP with liquid tank
E(P_{ev}) [%]	15.6	9.5	4.9	10.1
E(P_{cd}) [%]	26.6	3.6	12.4	7.8
E($\dot{Q}_{ev}$) [%]	21.2	25.6	21.9	11.9
E($\dot{Q}_{cd}$) [%]	15.1	15.8	15.7	9.7
E($\dot{W}_{cmp}$) [%]	20.7	3.4	11	5.9
E(COP) [%]	31	22	14.8	17.2

Table 4.5: Maximal errors of the heat pump model.

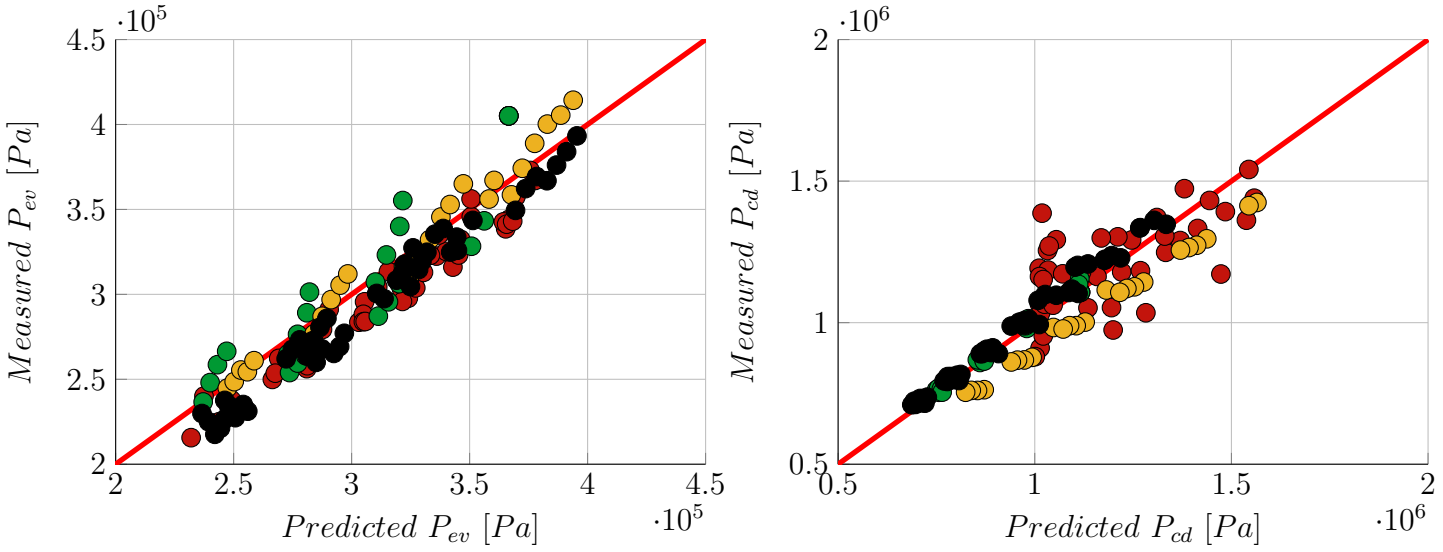

(a) (b)

Figure 4.11: Comparison between predicted evaporating pressure (a), and condensing pressure (b) by the heat pump model (red: overcharged system; green: well charged system with $1.1kg/s$ condenser water flow rate; orange: well charged system with small condenser water flow rate; black: liquid receiver added in the system with small condenser water flow rate).

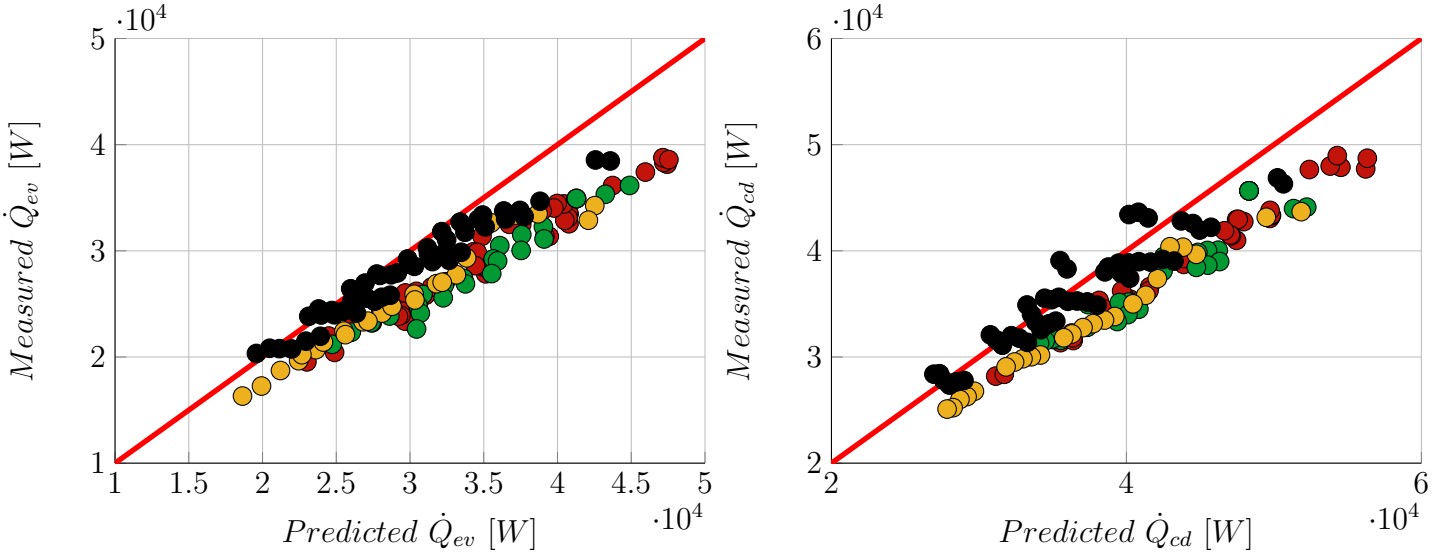

(a) (b)

Figure 4.12: Comparison between predicted evaporating thermal power (a), and condensing thermal power (b) by the heat pump model (red: overcharged system; green: well charged system with $1.1kg/s$ condenser water flow rate; orange: well charged system with small condenser water flow rate; black: liquid receiver added in the system with small condenser water flow rate).

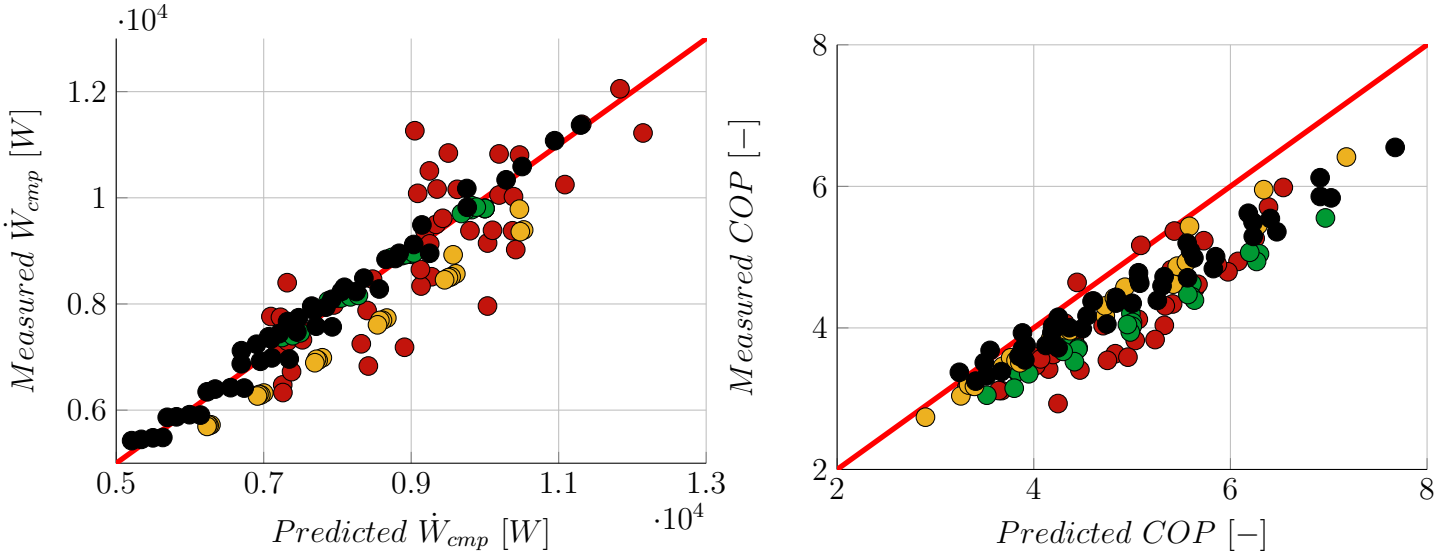

(a) (b)

Figure 4.13: Comparison between predicted compressor work (a), and heat pump COP (b) by the heat pump model (red: overcharged system; green: well charged system with $1.1 kg/s$ condenser water flow rate; orange: well charged system with small condenser water flow rate; black: liquid receiver added in the system with small condenser water flow rate).

4.4 Compressor analysis

4.4.1 Effect of the compressor losses on the isentropic efficiency

Considering the high efficiencies accuracy of the compressor sub-model (i.e. maximum error of 8.5% and 6.3% for the isentropic and volumetric efficiencies, respectively), this sub-model is used to illustrate the losses of the Danfoss SY240 scroll compressor.

Figure 4.14a shows the evolution of the isentropic compressor efficiency with the compression ratio (i.e. at fixed inlet pressure with varying outlet pressure) and the different losses. A scroll compressor is characterised by a fixed internal volume ratio $r_{v,in}$ which is responsible for the loss in isentropic efficiency at low and high compression ratio. In fact, the isentropic compression is followed by an expansion or a second compression, at constant volume and not a constant efficiency, up to the needed pressure. The more the fluid is compressed outside of the design conditions, the less efficient the compression process. The electromechanical losses are responsible for a significant drop in isentropic efficiency. The impact of those losses is higher at high rotational compressor speed. It can also be seen that the leakage flows have higher effects at high compression ratio, eventhough their impacts on the isentropic efficiency is low. The impact of the pressure drop at the compressor exhaust is negligible and is therefore not shown on the graph.

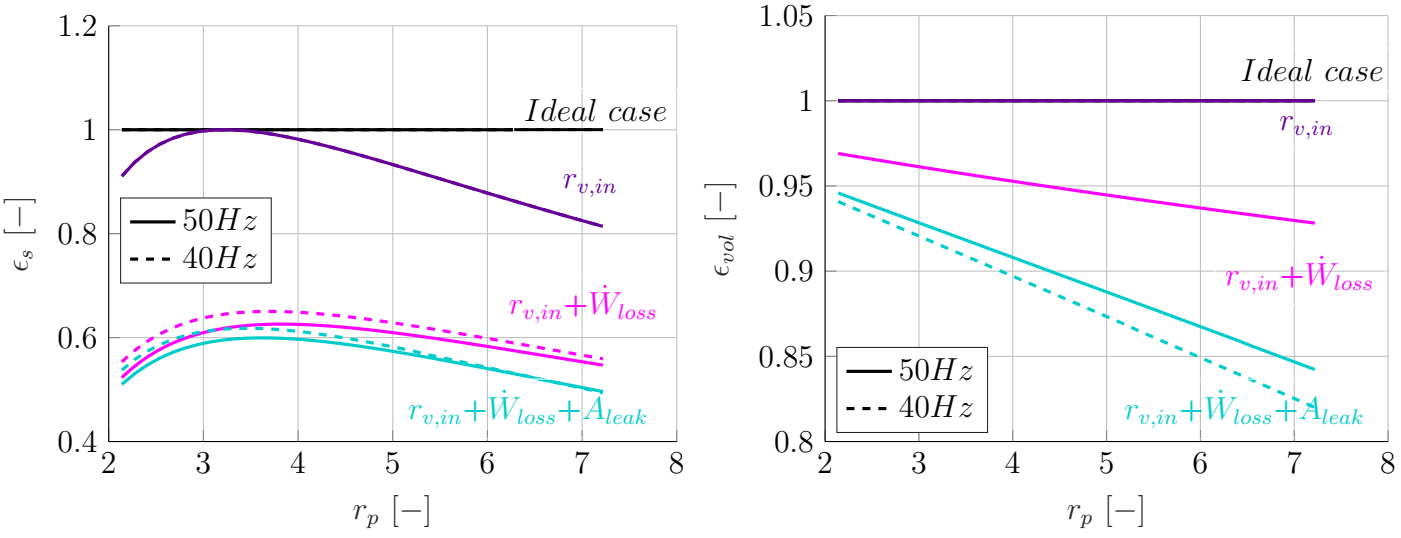

(a) (b)

Figure 4.14: Effect of the compressor losses on the isentropic efficiency (a) and volumetric efficiency (b).

Figure 4.14b illustrates the effect of the compressor losses on the volumetric efficiency. One can see that the fixed internal volume ratio does not impact ϵ_{vol}. The electromechanical losses and the leakage flow are highly impacting the volumetric efficiency, especially at high compression ratio. Figure 4.14b also shows volumetric inefficiencies at a rotational speed of $40Hz$.

4.4.2 Effect of the pressure ratio on the isentropic efficiency

The compressor sub-model is used to characterise the impact of the supply compressor pressure on the isentropic efficiency, as the experimental campaign aimed to keep $T_{ev,sf,su}$ constant rather than P_{su}. Figure 4.15 shows that the isentropic efficiency increases with increasing supply compressor pressure and reaches a maximum at intermediate compression ratio.

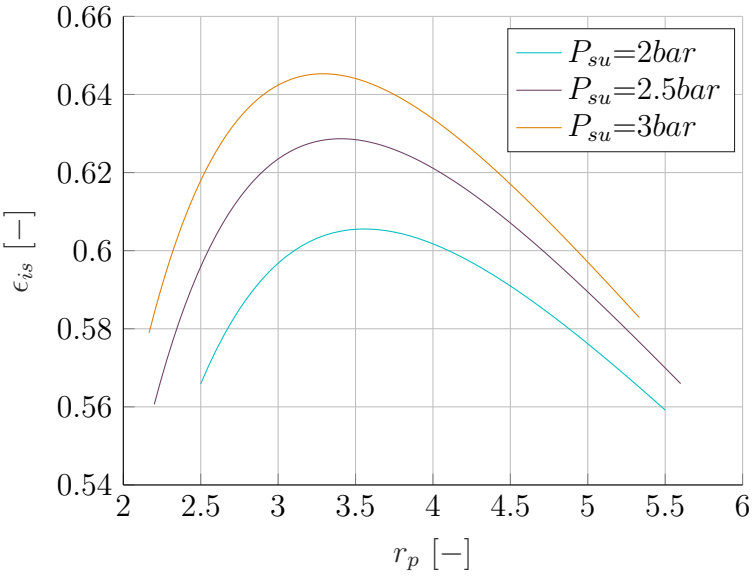

Figure 4.15: Variation of the isentropic efficiency with the compressor pressure ratio, for three value of supply pressure.

4.4.3 Comparison with Danfoss predictions

The experimental results can not be directly compared to the predicted results from the compressor manufacturer as data are provided for R134a and not for currently used R1234yf. Using the compressor sub-model, it is however possible to compare the predicted electrical work and refrigerant mass flow rate with the Danfoss data. The results obtained with the same operating conditions (i.e. R134a refrigerant, superheat of 8K and subcooling of 2K) are shown in Figures 4.16a and 4.16b. One can see that Danfoss has overpredicted the electrical consumption while the mass

flow rate is well predicted, except at high condensing temperature.

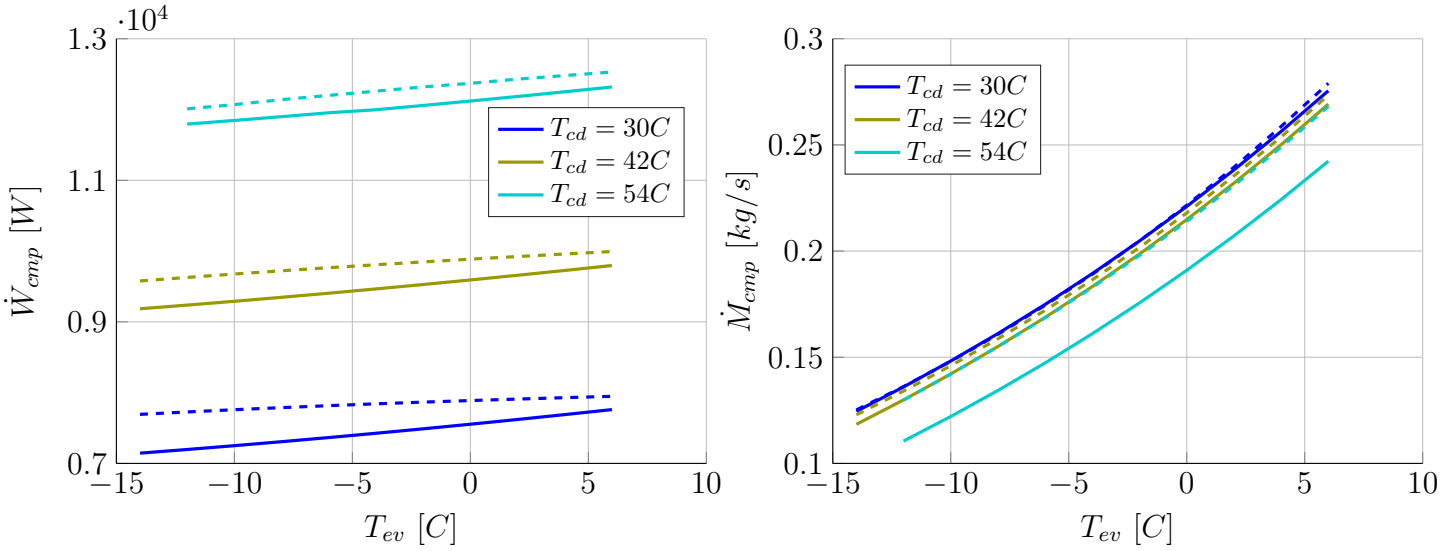

(a) (b)

Figure 4.16: Comparison between the manufacturer predictions (dashed lines) and the compressor sub-model (plain lines) for the compressor work (a), and the refrigerant mass flow rate (b).

Chapter 5

Perspectives

Uncertainties and inaccuracies have been identified concerning the experimental campaign and the heat pump modelling. The perspectives and improvements of this work are various:

- The first analysis of the experimental campaign has shown uncertainties in some temperature measurements. In fact, an analysis of the temperatures at the evaporator inlet and compressor exhaust has demonstrated that those measurements were aberrant and were therefore neglected. A set of new sensors should be installed on the heat pump unit to validate this assumption and to exactly know the state of the fluid at the compressor exhaust (i.e before the four-way valve).

- A total of 6 pressure sensors are installed on the test bench, as shown in Figure 2.1, to precisely characterise the states undergone by the working fluid. However, the accuracy level of the sensors is too low to quantify the pressure drops of the system. In fact, the measurements indicate a mean pressure rise of $6000Pa$ in the condenser which is physically impossible. Differential pressure transmitters could be installed around the four-way valve and the heat exchangers. Those elements should then be modelled to reach higher accuracy in the predicted values. The system has also shown refrigerant bubbles at the entrance of the electronic expansion valve even with subcooling around $5K$ at the condenser outlet. Adding a differential pressure transmitter in the liquid line would give information on the pressure losses undergone by the refrigerant and the prediction of the subcooling loss would therefore be possible.

- The experimental campaign has shown that the subcooling has a high impact on the heat pump performance. However, the subcooling could not be directly influenced. Adding a subcooler in the heat pump would allow to characterise its impact on the COP and evaluate the optimal subcooling.

- The optimal mass of refrigerant has been chosen by minimizing it while keeping enough subcooling to ensure saturated liquid at the inlet of the electronic

expansion valve. It would be of interest to investigate the heat pump performances under various refrigerant charges.

- The heat pump has been manufactured to work both on heating and cooling mode. However, the system needs improvements to be completely reversible. In fact, the liquid receiver and the electronic expansion valve locations are not suitable for the cooling mode. The liquid line should be completely re-designed.

- Fluctuations of the thermodynamic quantities have been measured during the test campaign, even with a liquid receiver in the system. It has been noticed that the temperature at the evaporator outlet, measured by the sensor of the EEV controller, was oscillating while the thermocouple measurement was steady at the same location. These temperature oscillations have led to fluctuations in the EEV opening degree and therefore in the whole system. The sensor has been changed once without significant improvements, further investigation is therefore required.

- Liquids receiver are sized on the basis of the total refrigerant load and selected with an internal volume 20% bigger. Considering a refrigerant charge of $5.25kg$ and the R1234yf density (i.e. $1.1\ g/cm^3$), a liquid receiver of 6 to 8 litres should have been added in the system. However, due to high delays time associated to the appropriate sized one, a liquid receiver of $20l$ was mounted on the heat pump. Tests with a well-sized receiver should be performed.

- The test bench has been equipped with various and expensive sensors. In a commercial heat pump, the final cost is a critical issue. A study should be performed to assess the essential sensors for the good functioning of the system. A stand-alone control of the heat pump should also be implemented.

- The compressor rotational speed can vary between 2400 and $3600rpm$ but tests have only been performed at 2400 and $3000rpm$. The electrical installation should be reviewed to allow higher current to test the system at higher rotational speeds.

- The heat pump has shown to be highly charge-sensitive. The refrigerant charge effect should be deeply studied to allow good modelling of the system.

- The heat pump model imposes the value of the subcooling and overheating. A fixed overheating has shown good results as the controller of the expansion valve keeps the overheating value constant. However, the subcooling is highly dependent on the testing conditions and imposing its value has shown inaccuracy in the performance predictions. Studies should be performed to correctly predict the subcooling value, or the model should be adjusted.

Chapter 6

Conclusion

The heat pump industry is constantly renewing itself, in a ceaseless research of environmentally friendly refrigerant. HFO-1234yf is a hydrofluoro-olefin refrigerant and a successor of high-GWP refrigerants. R1234yf is already used as a drop-in replacement of R134a in automotive applications, but researches are still conducted to assess its performances in heating and cooling applications. This study aimed to characterise and predict the performances of a water-to-water R1234yf heat pump. A performance map was determined in nominal conditions. The behaviour of the system was then studied under changing temperatures and compressor rotational speeds. The impact of the refrigerant charge, the subcooling, the overheating and a liquid receiver was also assessed. Finally, a semi-empirical model was developed to predict the heat pump performances.

A test bench was built and fully equipped with sensors. The components mounted on the test-rig allowed the variation of five independent variables: the condenser water outlet temperature, the evaporator Ethylene Glycol inlet temperature, the two secondary fluids mass flow rates (i.e. of the condenser and evaporator loops), and the compressor rotational speed. The heat pump was designed to produce heat at $35°C$ (for floor heating) by taking advantage of a geothermal source at $12°C$. In those conditions, the coefficient of performances reached the value of 4.72, with a compressor speed of $2400rpm$ and secondary fluid mass flow rates of $1.1kg/s$. Due to technical issues, the performances could not be evaluated at higher compressor rotational speed in the same conditions. However, the experimental campaign allowed testing in various conditions. The COP of the heat pump increased with a smaller condenser mass flow rate, as it increased the water temperature lift, the subcooling and therefore the condensing heat load without modifying the electrical consumption. It was demonstrated that increasing the superheat value decreases the coefficient of performance. The superheat should be kept to its lowest value while ensuring saturated vapour at the compressor inlet. The experimental campaign showed that the compressor isentropic efficiency is maximal at a compressor ratio of

± 3.5, increases with increasing refrigerant mass flow rate and decreasing compressor rotational speed. The scroll compressor reaches high isentropic efficiency at high evaporating temperature and intermediate condensing temperature. The volumetric efficiency increases with increasing rotational speed, increasing refrigerant mass flow rate and decreasing compression ratio. Adding a liquid receiver allows stabilising the system, its effect is significant at high condensing temperature. However, the subcooling is almost entirely lost in the liquid receiver, causing the refrigerant to enter the expansion valve in a two-phase state and causing large variations of the EEV opening degree. It is mandatory to subcool the working fluid after the liquid receiver to achieve a stable system.

The experimental results were used to calibrate the heat pump semi-empirical model. Each sub-model (i.e of the compressor, the condenser and the evaporator) were predicting, without many errors, the performances of the components. The heat pump model is subjected to the propagation of errors and shows losses of accuracy.

To conclude this work, possibilities of improvements and perspectives are provided in the last chapter.

Bibliography

[1] Fabio Pantano and Roberto Capata. Expander selection for an on board orc energy recovery system. *Energy*, 141, 09 2017.

[2] S. Liu S. Kakac. Heat exchangers selection, rating, and thermal design. *CRC*, 2002.

[3] European Commission. Mapping and analyses of the current and future (2020 - 2030) heating/cooling fuel deployment (fossil/renewables). 2016.

[4] European Commission. Communication from the commission to the european parliament, the council, the european economic and social committee and the committee of the regions: An eu strategy on heating and cooling. 2016.

[5] European Commission. Mapping and analyses of the current and future (2020 - 2030) heating/cooling fuel deployment (fossil/renewables). March 2016.

[6] Harish Satyavada and Simone Baldi. Monitoring energy efficiency of condensing boilers via hybrid first-principle modelling and estimation. *Energy*, 142:121–129, 2018.

[7] Zivic Marija, Antun Galovic, Jurij Avsec, and Antun Barac. Application of gas condensing boilers in domestic heating. *Tehnicki Vjesnik*, 26:681–685, 01 2019.

[8] Hisham Khatib. *Energy Efficiency and Electrical Power Generation*. 03 2012.

[9] R. Mikalsen. 6 - internal combustion and reciprocating engine systems for small and micro combined heat and power (chp) applications. In Robert Beith, editor, *Small and Micro Combined Heat and Power (CHP) Systems*, Woodhead Publishing Series in Energy, pages 125–146. Woodhead Publishing, 2011.

[10] R. Napoli, M. Gandiglio, A. Lanzini, and M. Santarelli. Techno-economic analysis of pemfc and sofc micro-chp fuel cell systems for the residential sector. *Energy and Buildings*, 103:131–146, 2015.

[11] I. Staffell, R. Green, and K. Kendall. Cost targets for domestic fuel cell chp. *Journal of Power Sources*, 181(2):339–349, 2008.

[12] Salvador Acha, Niccolo Le Brun, Maria Damaskou, Tekena Craig Fubara, Vinay Mulgundmath, Christos N. Markides, and Nilay Shah. Fuel cells as combined heat and power systems in commercial buildings: A case study in the food-retail sector. *Energy*, 206:118046, 2020.

[13] Julian Packer. Commercialisation of fuel cells for combined heat and power (chp) application. *Journal of Power Sources*, 37(1):101–109, 1992.

[14] H. Krause A. Herrmann, J. Schumann. Cost-efficiency of a chp hydrogen fuel cell. *3rd International Hybrid Power Systems Workshop*, 2018.

[15] S.O Andersen and J.M Lupinacci. Implication of cfcs on environmental quality and opportunities for engineering solutions. *International Journal of Refrigeration*, 11(4):253–256, 1988.

[16] Mikael Eriksson and Oskar Graffman. Modelling and simulation of heat pump systems for hybrid and electrical vehicles. 2018.

[17] Changru Yang, Sangwon Seo, Nobuo Takata, Kyaw Thu, and Takahiko Miyazaki. The life cycle climate performance evaluation of low-gwp refrigerants for domestic heat pumps. *International Journal of Refrigeration*, 121:33–42, 2021.

[18] Benjamin K. Sovacool, Steve Griffiths, Jinsoo Kim, and Morgan Bazilian. Climate change and industrial f-gases: A critical and systematic review of developments, sociotechnical systems and policy options for reducing synthetic greenhouse gas emissions. *Renewable and Sustainable Energy Reviews*, 141:110759, 2021.

[19] Adrián Mota-Babiloni, Joaquín Navarro-Esbrí, Ángel Barragán-Cervera, Francisco Molés, and Bernardo Peris. Analysis based on eu regulation no 517/2014 of new hfc/hfo mixtures as alternatives of high gwp refrigerants in refrigeration and hvac systems. *International Journal of Refrigeration*, 52:21–31, 2015.

[20] Di Wu, Bin Hu, and R.Z. Wang. Vapor compression heat pumps with pure low-gwp refrigerants. *Renewable and Sustainable Energy Reviews*, 138:110571, 2021.

[21] Andy Pearson. Refrigeration with ammonia. *International Journal of Refrigeration*, 31(4):545–551, 2008.

[22] Ioan Sarbu and Calin Sebarchievici. Chapter 3 - substitution strategy of non-ecological refrigerants. In Ioan Sarbu and Calin Sebarchievici, editors, *Ground-Source Heat Pumps*, pages 27–45. Academic Press, 2016.

[23] Alison Subiantoro and Kim Tiow Ooi. Chapter 10 - dynamic characteristics of rolling piston machines. In Ibrahim A. Sultan and Truong H. Phung, editors, *Positive Displacement Machines*, pages 263–289. Academic Press, 2019.

[24] Ioan Sarbu and Calin Sebarchievici. *Substitution Strategy of Non-Ecological Refrigerants*, pages 27–45. 12 2016.

[25] Milan N. Šarevski and Vasko N. Šarevski. Characteristics of r718 refrigeration/heat pump systems with two-phase ejectors. *International Journal of Refrigeration*, 70:13–32, 2016.

[26] Di Wu, Bin Hu, R.Z. Wang, Haibin Fan, and Rujin Wang. The performance comparison of high temperature heat pump among R718 and other refrigerants. *Renewable Energy*, 154(C):715–722, 2020.

[27] Y.S Chang, M.S Kim, and S.T Ro. Performance and heat transfer characteristics of hydrocarbon refrigerants in a heat pump system. *International Journal of Refrigeration*, 23(3):232–242, 2000.

[28] Björn Palm. Hydrocarbons as refrigerants in small heat pump and refrigeration systems – a review. *International Journal of Refrigeration*, 31(4):552–563, 2008.

[29] Y.S Chang, M.S Kim, and S.T Ro. Performance and heat transfer characteristics of hydrocarbon refrigerants in a heat pump system. *International Journal of Refrigeration*, 23(3):232–242, 2000.

[30] Eric Granryd. Hydrocarbons as refrigerants — an overview. *International Journal of Refrigeration*, 24(1):15–24, 2001.

[31] Björn Palm. Hydrocarbons as refrigerants in small heat pump and refrigeration systems – a review. *International Journal of Refrigeration*, 31(4):552–563, 2008. Refrigeration with Ammonia and Hydrocarbons.

[32] R. Cabello, D. Sánchez, R. Llopis, I. Arauzo, and E. Torrella. Experimental comparison between r152a and r134a working in a refrigeration facility equipped with a hermetic compressor. *International Journal of Refrigeration*, 60:92–105, 2015.

[33] Kasni Sumeru, Cecep Sunardi, Azhar abdul aziz, Henry Nasution, Adekunle Abioye, and Mohd Farid Muhamad Said. Comparative performance between r134a and r152a in an air conditioning system of a passenger car. *Jurnal Teknologi*, 78, 10 2016.

[34] M. Bryson, C. Dixon, and S. StHill. Testing of hfo-1234yf and r152a as mobile air conditioning refrigerant replacements. 2011.

[35] Kundlik V. Mali Kalpesh N. Kothale and S. D. Nimbalkar. Study of r-161 refrigerant as an alternate refrigerant to various other refrigerants. *International Journal of Current Engineering and Technology*, 2016.

[36] Rishiraj Ladkat Pankaj Bhojane Rohit Ahire Ashish Utage Rushikesh Jog, Kundlik V. Mali. Hfc-161 as an alternative to hcfc-22 in air conditioner. *International Journal for Research in Engineering Application Management*, 2018.

[37] D. N. Hatkar Subodh Deshpande. Study of performance of binary mixture of r134a and r161 as a substitution of r134a in a domestic refrigerator. *International Journal of Engineering Research Technology*, 4, 2015.

[38] Carlos Mateu-Royo, Joaquín Navarro-Esbrí, Adrián Mota-Babiloni, Marta Amat-Albuixech, and Francisco Molés. Thermodynamic analysis of low gwp alternatives to hfc-245fa in high-temperature heat pumps: Hcfo-1224yd(z), hcfo-1233zd(e) and hfo-1336mzz(z). *Applied Thermal Engineering*, 152:762–777, 2019.

[39] Cordin Arpagaus, Ralph Kuster, Manuel Prinzing, Michael Uhlmann, Elias Büchel, Stefan Frei, Jürg Schiffmann, and Stefan Bertsch. High temperature heat pump using hfo and hcfo refrigerants - system design and experimental results. 08 2019.

[40] Vipin Nair. Hfo refrigerants: A review of present status and future prospects. *International Journal of Refrigeration*, 122:156–170, 2021.

[41] Sergio Bobbo, Giovanni Di Nicola, Claudio Zilio, J. Steven Brown, and Laura Fedele. Low gwp halocarbon refrigerants: A review of thermophysical properties. *International Journal of Refrigeration*, 90:181–201, 2018.

[42] Juan J.G. Pabon, Ali Khosravi, J.M. Belman-Flores, Luiz Machado, and Remi Revellin. Applications of refrigerant r1234yf in heating, air conditioning and refrigeration systems: A decade of researches. *International Journal of Refrigeration*, 118:104–113, 2020.

[43] Adrián Mota-Babiloni, Pavel Makhnatch, and Rahmatollah Khodabandeh. Recent investigations in hfcs substitution with lower gwp synthetic alternatives: Focus on energetic performance and environmental impact. *International Journal of Refrigeration*, 82:288–301, 2017.

[44] Giulia Righetti, Claudio Zilio, and Giovanni A. Longo. Comparative performance analysis of the low gwp refrigerants hfo1234yf, hfo1234ze(e) and hc600a inside a roll-bond evaporator. *International Journal of Refrigeration*, 54:1–9, 2015.

[45] Atilla Gencer Devecioğlu and Vedat Oruç. Characteristics of some new generation refrigerants with low gwp. *Energy Procedia*, 75:1452–1457, 2015.

[46] R. Dickes. Charge-sensitive methods for the off-design performance characterization of organic rankine cycle (orc) power systems. 2019.

[47] Carl Hiller and Leon Glicksman. Improving heat pump performance via compressor capacity control - analysis and test, volume 1. 01 1976.

[48] R. Ellison, F. Creswick, C Keith Rice, W. Jackson, and S. Fischer. Heat pump modeling: A progress report. 03 1979.

[49] Hui Jin and J Spitler. Parameter estimation based model of water-to-water heat pumps with scroll compressors and water/glycol solutions. *Building Services Engineering Research and Technology*, 24(3):203–219, 2003.

[50] Daniel Carbonell, Jordi Cadafalch, Peter Pärisch, and Ricard Consul. Numerical analysis of heat pump models. comparative study between equation-fit and refrigerant cycle based models. 2012.

[51] Validation of a numerical model aimed at the estimation of performance of vapor compression based heat pumps. *Energy and Buildings*, 47:411–420, 2012.

[52] Eric Winandy, Claudio Saavedra O, and Jean Lebrun. Experimental analysis and simplified modelling of a hermetic scroll refrigeration compressor. *Applied Thermal Engineering*, 22(2):107–120, 2002.

[53] Frédéric Ransy, S. Gendebien, and V. Lemort. Modelling of an exhaust air heat pump used for heating and domestic hot water production. 2020.

[54] Sano K. Oono M. Iwamura S. Ishii N., Bird K. and T. Otokura. Refrigerant leakage flow evaluation for scroll compressors. *International Compressor Engineering Conference*, 1996.

[55] Martin H. A theoretical approach to predict the performance of chevron-type plate heat exchangers. *Chemical Engineering and Processing*, 35:301–310, 1996.

[56] Zilio C. Longo G., Righetti G. A new computational procedure for refrigerant condensation inside herringbone-type brazed plate heat exchangerss. *International Journal of Heat and Mass Transfer*, 82:530–536, 2015.

[57] Giovanni A. Longo, Simone Mancin, Giulia Righetti, and Claudio Zilio. A new model for refrigerant boiling inside brazed plate heat exchangers (bphes). *International Journal of Heat and Mass Transfer*, 91:144–149, 2015.

1